



UPPSALA
UNIVERSITET

*Digital Comprehensive Summaries of Uppsala Dissertations
from the Faculty of Science and Technology 1761*

Computational Studies of 2D Materials

*Application to Energy Storage and Electron
Transport in Nanoscale Devices*

VIVEKANAND SHUKLA



ACTA
UNIVERSITATIS
UPSALIENSIS
UPPSALA
2019

ISSN 1651-6214
ISBN 978-91-513-0547-9
urn:nbn:se:uu:diva-369471

Dissertation presented at Uppsala University to be publicly examined in 80101, Ångströmlaboratoriet, Lägerhyddsvägen 1, Uppsala, Friday, 1 March 2019 at 13:00 for the degree of Doctor of Philosophy. The examination will be conducted in English. Faculty examiner: Prof. Dr. Kristian Sommer Thygesen (Denmark Technical University, Denmark).

Abstract

Shukla, V. 2019. Computational Studies of 2D Materials. Application to Energy Storage and Electron Transport in Nanoscale Devices. *Digital Comprehensive Summaries of Uppsala Dissertations from the Faculty of Science and Technology* 1761. 101 pp. Uppsala: Acta Universitatis Upsaliensis. ISBN 978-91-513-0547-9.

The field of two-dimensional (2D) layered materials provides a new platform for studying diverse physical phenomena that are scientifically interesting and relevant for technological applications. Novel applications in electronics and energy storage harness the unique electronic, optical, and mechanical properties of 2D materials for design of crucial components. Atomically thin, with large surface to volume ratio, these materials are attractive for broad applications for hydrogen storage, sensing, batteries and photo-catalysis. Theoretical predictions from atomically resolved computational simulations of 2D materials play a pivotal role in designing and advancing these developments.

The central topic of this thesis is 2D materials studied using density functional theory and non-equilibrium Green's function. The electronic structure and transport properties are discussed for several synthesized and predicted 2D materials, with diverse potential applications in nanoscale electronic devices, gas sensing, and electrodes for rechargeable batteries. Lateral and vertical heterostructures have been studied for applications in nanoscale devices such as graphene/hBN heterostructure nanogap for a potential DNA sequencing device, while in case of twisted bilayer black phosphorus nanojunction, where electronic and transport properties have been explored for diode-like characteristics device. We also have addressed the structural, electronic and transport properties of the recently synthesized polymorphs of 2D borons known as borophenes. We have explored the conventional methods of tuning the material's properties such as strain in borophene and substitutional doping in black phosphorus with the further investigation of their gas sensing application.

A significant portion of this thesis is also dedicated to the energy storage applications of different 2D materials. Energy storage technologies arise with vital importance in providing effective ways to transport and commercialize the produced energy, aiming at rechargeable batteries with high energy and power density. In this context, first-principles simulations have been applied together with other theoretical tools to evaluate structural properties, ion intercalation kinetics, specific capacity and open circuit voltage of selected 2D materials at the atomic level. The simulation study supports the understanding while improving the properties of the materials to increase their efficiency in battery operation.

Keywords: Density functional theory, Non-equilibrium Green's function, 2D materials, Energy storage, Electron transport

Vivekanand Shukla, Department of Physics and Astronomy, Materials Theory, Box 516, Uppsala University, SE-751 20 Uppsala, Sweden.

© Vivekanand Shukla 2019

ISSN 1651-6214

ISBN 978-91-513-0547-9

urn:nbn:se:uu:diva-369471 (<http://urn.kb.se/resolve?urn=urn:nbn:se:uu:diva-369471>)

Dedicated to the reader

List of papers

This thesis is based on the following papers, which are referred to in the text by their Roman numerals.

- I **Prospects of Graphene-hBN Heterostructure Nanogap for DNA Sequencing**
Vivekanand Shukla, Naresh K. Jena, Anton Grigoriev, and Rajeev Ahuja
ACS Appl. Mater. Interfaces **9**(46), 39945-39952 (2017)
- II **Rectifying properties in 90° rotated bilayer black phosphorus nanojunction: A first principle study**
Vivekanand Shukla, Anton Grigoriev, and Rajeev Ahuja
Submitted
- III **Strain controlled electronic and transport anisotropies in two-dimensional borophene sheets**
Vivekanand Shukla, Naresh K. Jena, Anton Grigoriev, and Rajeev Ahuja
Phys. Chem. Chem. Phys. **20**, 22952-22960 (2018)
- IV **Toward the Realization of 2D Borophene Based Gas Sensor**
Vivekanand Shukla, John Wörnå, Naresh K. Jena, Anton Grigoriev, and Rajeev Ahuja
J. Phys. Chem. C **121**(48), 26869-26876 (2017)
- V **Ultrahigh-sensitive gas sensors based on doped phosphorene: A First-principles investigation**
Jariyane Prasongkit, Vivekanand Shukla, Anton Grigoriev, Rajeev Ahuja, and Vittaya Amornkitbamrung
Manuscript
- VI **The curious case of two dimensional Si₂BN: A high-capacity battery anode material**
Vivekanand Shukla, Rafael B.Araujo, Naresh K. Jena, and Rajeev Ahuja
Nano Energy **41**, 251-260 (2017)

VII Borophane as a Benchmark of Graphene: A Potential 2D Material for Anode of Li and Na-Ion Batteries

Naresh K. Jena, Rafael B.Araujo, Vivekanand Shukla, and Rajeev Ahuja
ACS Appl. Mater. Interfaces **9**(19), 16148-16158 (2017)

VIII Borophene's tryst with stability: exploring 2D hydrogen boride as an electrode for rechargeable batteries

Vivekanand Shukla, Rafael B.Araujo, Naresh K. Jena, and Rajeev Ahuja
Phys. Chem. Chem. Phys. **20**, 22008-22016 (2018)

IX Modeling High-performing Batteries with Mxenes: The case of S-functionalized two-dimensional Nitride Mxene Electrode

Vivekanand Shukla, Naresh K. Jena, and Rajeev Ahuja
Submitted

Reprints were made with permission from the publishers.

Comments on my own contribution

All the works presented in the Papers I to IX have been performed in the close collaboration with the co-authors. A brief description of my contribution to the works is summarized as follows. All the articles where I am the first author, I took the central responsibility for designing the project, performing theoretical calculations, interpreting data, preparing figures and writing manuscript. In paper V, I participated in designing the research and performed part of the calculations, analyzed data and wrote the manuscript. In Paper VII, I was associated with designing the project and helped in analyzing data.

List of papers not included in the thesis

During the time frame of this thesis, the following works have been made, but, these are not included in the thesis.

♠ **Stability of $\text{Ar}(\text{H}_2)_2$ to 358 GPa**

Cheng Ji, Alexander F Goncharov, Vivekanand Shukla, Naresh K Jena, Dmitry Popov, Bing Li, Junyue Wang, Yue Meng, Vitali B Prakapenka, Jesse S Smith, Rajeev Ahuja, Wenge Yang, Ho-kwang Mao
PNAS **114** (14) 3596-3600 (2017)

♠ **Enabling the Electrochemical Activity in Sodium Iron Metaphosphate $[\text{NaFe}(\text{PO}_3)_3]$ Sodium Battery Insertion Material: Structural and Electrochemical Insights**

Ritambhara Gond, Sher Singh Meena, SM Yusuf, Vivekanand Shukla, Naresh K Jena, Rajeev Ahuja, Shigeto Okada, Prabeer Barpanda
Inorganic chemistry **56** (10), 2017

♠ **Sub 20 nm metal-conjugated molecule junctions acting as a nitrogen dioxide sensor**

Ishtiaq Hassan Wani, Syed Hassan Mujtaba Jafri, John Wörnå, Aqib Hayat, Hu Li, Vivekanand Shukla, Andreas Orthaber, Anton Grigoriev, Rajeev Ahuja, Klaus Leifer
Submitted

♠ **Anti-carcinogenic Activity of Blue Fluorescent h-BN Quantum Dots: As an Effective Enhancer for DNA Cleavage Activity of Anti-cancer Drug Doxorubicin**

Sima Umrao, Akhilendra K. Maurya, Vivekanand Shukla, Anton Grigoriev, rajeev Ahuja, Manjula Vinayak, Rohit R. Srivastava, Preeti S Saxena, Ilkwon Oh, Anchal Srivastava
submitted

♠ **Electronic transport properties in bilayer phosphorene and substitution effect in bilayer nano junction: A first principles investigation**

Vivekanand Shukla, Naresh K. Jena, Anton Grigoriev and Rajeev Ahuja
Manuscript

Contents

Part I: Introduction & Theoretical background	11
1 Introduction	13
1.1 Thesis Outline	17
2 Theoretical background	18
2.1 The many-body problem	18
2.2 Density functional theory	20
2.2.1 Hohenberg-Kohn theorem	20
2.2.2 Kohn-Sham Formalism	22
2.3 Exchange-correlation functionals	23
2.3.1 Local density approximations	23
2.3.2 Generalized gradient approximations (GGA)	24
2.4 Electronic structure of periodic solids	25
2.5 Pseudopotentials	25
2.6 Basis sets	27
2.6.1 Plane waves	27
2.6.2 Projector augmented wave	28
2.6.3 LCAO basis set	30
2.7 Force theorem and geometry optimization	32
2.8 Quantum transport theory	33
2.8.1 The Landauer formula	33
2.9 Non-equilibrium Green's function	36
2.9.1 The Schrödinger equation	38
2.9.2 Transport problem and charge density	39
2.9.3 Calculation of current	41
Part II: Summary of the Results	43
3 Nanoscale device applications of 2D materials	45
3.1 DNA sequencing in Graphene/h-BN nanogap	45
3.2 Twisted bilayer black phosphorus nanojunction	49
4 Electronic and transport properties of 2D materials	54
4.1 β_{12} and χ -borophene	55
4.1.1 Electron transport properties	56
4.2 Corrugated borophene	58

4.3	S/Si substituted black phosphorus	62
5	2D materials for anode application in rechargeable batteries	68
5.1	Intercalation profile	68
5.2	Basin-hopping	70
5.3	Nudged elastic band method	71
5.4	2D Si ₂ BN anode for rechargeable battery	72
5.5	Hydrogenated 2D boron anode for rechargeable battery	74
5.5.1	2D B ₂ H ₂ case	75
5.5.2	2D BH case	77
5.6	S-Mxene and application in battery anode	79
	Part III: Final Remarks	83
6	Summary and Outlook	85
6.1	Future prospects	87
7	Svensk sammanfattning	89
8	Acknowledgments	92
	References	94

Part I:
Introduction & Theoretical background

1. Introduction

For a long time, it was believed in the scientific community that two dimensional (2D) materials might not, strictly speaking, exist [1, 2]. During the first half of the last century, theoreticians predicted that the low dimensional crystal would most likely disintegrate at finite temperature because of the large displacement of lattice atoms resulting from diverse sources of thermal fluctuations [2–4]. Typically, the amplitude of this displacement was suggested to be in the same order of the interatomic distances in the material. Further, Mermin extended this theory in his publication, which was strongly supported by experimental observations, presenting that the melting point of the thin films material rapidly reducing with decreasing its thickness [5–7]. This proved to give a solid understanding of the supported thin films and yielded the long-standing belief that these materials can only be grown on the solid substrate with a negligible lattice mismatch, but they cannot be stable in freestanding (isolated) form. The common understanding largely prevailed until the impossible goal was achieved in the form of isolation of graphene sheet in 2004 by Novoselov *et al.* [8]. Although, it will not be justified to ignore the previous efforts on the isolation of monolayer materials as some of them even dated long before 2004 [9–12], it was only the work from Novoselov and co-workers, which successfully reported the exfoliation of few layers of graphene and presented its physical properties [8]. The discovery proved to be a turning point of significant research covering material science, physics, chemistry and driving the exploration of novel 2D materials associated with vivid range of applications.

Why these 2D materials are interesting? In general, the word "2D materials" is quite obscure as there is a broad collection of materials that come into this class with a wide range of characteristics. 2D materials are generally defined as crystalline materials consisting of substances with a thickness of few nanometers or less. There are layered metals, semi-metals, insulators, small and moderate bandgap semiconductors in this class such as transition metal dichalcogenides (TMDCs), hexagonal boron nitride (hBN), Mxenes and so on. There also exist layered materials such as black phosphorus (BP) and ReS_2 , which possesses in-plane electrical and optical anisotropy [13, 14]. The only common string among all these materials is the strong *intra*-layer bonding along with the weak *inter*-layer van der Waals (vdW) interaction. This implies that they can be mechanically exfoliated in the form of mono or few-layer on a substrate. 2D materials, such as molybdenum disulfide (MoS_2) and other members of TMDC family, Mxenes, BP, hBN represent the ultimate

scaling of the materials dimension in the vertical direction [15–21]. However, there is also a class of materials, which can be synthesized from precursors in a bottom-up approach and we call them here synthetic 2D materials such as silicene, germanene, tellurene, several polymorph of borophene and so on [22–28]. In addition to these materials, there are several other theoretically predicted layered materials have been found, which are needed to be experimentally synthesized [29, 30]. Some remarkable properties of the 2D materials are superior elastic properties, meaning strength, stiffness and flexibility; ability to interact with light, create heterostructures, trap free surfaces and abundant active sites; high in-plane conductivity. The reasonable flexibility in 2D materials certainly allows the tailoring of their electronic properties [31, 32]. The mechanical properties enable them for flexible and stretchable electronic applications [33]. Beside these characteristics, they can be electrically biased and operated at low bias voltages. It is also very promising that so far isolated 2D materials can embrace the entire range of the electromagnetic spectrum [34, 35].

The importance of 2D materials has been increased because of the problems in the miniaturization of modern electronic devices. At present, we have entered the era, where the modern laptops and smart-phones are made with more than a billion transistors ¹, but the conventional methods of further miniaturization of electronic devices for increased productivity are facing challenges [36, 37]. The search for novel devices and materials becomes the forefront of technological research while sustaining with famous Moore’s law [38]. The key requirement in present time is to look beyond the silicon-based CMOS (Complementary Metal Oxide Semiconductor) technology and search for different alternatives, in which 2D crystals provide very interesting form-factors with respect to traditional 3D crystals. Although, devices made from 2D materials are still in the laboratory scale but they have not failed to present strong promise for future [39, 40]. The high-mobility in these materials offers an alternative in the expanding field of low cost and large area electronics, which is currently dominated by low-mobility organic semiconductors and amorphous silicon [41].

For example, Meric *et al.* [42] reported one of the first demonstrations of graphene-based device as top-gated graphene field effect transistor (GFET), which was based on a high- k gate dielectric without any bandgap engineering. Although $I_{\text{on}}/I_{\text{off}}$ ratio was poor, but high transconductance and current saturation were achieved. Further experiments observed an extremely high charge carrier mobility, which was remained high even after electron and hole doping and this enables high current through the device [43–46]. However, absence of band gap in graphene limits the associated applications in electronic devices

¹The very first Central Processing Unit (CPU) on single chip (Intel 4004) had 2300 transistors. Whereas modern standard core i7 quad-CPU has 731,000,000 transistors. This is still a low number compared to the high-end 8-Core Xeon Nehalem-EX with 2,300,000,000 transistors.

[44, 45]. As the solution for the lack of bandgap in graphene, 2D semiconductor materials such as TMDCs have been emerged as the possible alternatives [47, 48]. Recently, many essential electronic components have been manifested based on mono or few-layers of different TMDC materials, e.g., field-effect transistors (FETs), sensors and photo-transistors [49–54]. However, regardless of much encouraging theoretical foresight, the observed mobility of TMDC based devices is still moderate due to the scattering mechanisms and heavy effective mass of charge carriers [47, 50]. In 2014, Li *et al.* conducted a study, where they showed that the high mobility ($1000 \text{ cm}^2\text{V}^{-1}\text{s}^{-1}$) in BP was superior to that of commercial silicon-based devices and the drain current modulation at room temperature was larger than that in graphene by four orders [55].

Apart from the electronic application as a transistor material, graphene has also proved to be the robust electrode for a molecular electronic device such as single molecular rectifier, switches and negative differential resistance (NDR) devices in several experimental and theoretical works [56–58]. The nonopore and nanogaps in 2D materials have been well explored for the salt water filtering and ambitious DNA sequencing due to atom layer thinness [59–68]. In the recent trend, vertical heterostructure based on 2D vdW materials are being synthesized [69–71]. This integrates their isolated properties and opens a new possibility of utilizing 2D materials in nanoscale device applications such as gate free rectifier, and transistor [72–77]. The lateral heterostructures are also reported for tuning the electronic and structural properties of 2D materials and their further applications [78]. In addition to the current controlling devices, 2D materials have been reported for the identification and quantification of toxic gases and organic vapors. They have shown potential promise in the form of chemiresistors, FET transistors sensors, conductometric sensors and impedance sensors to detect the various types of gas [79].

Along with the miniaturization of electronic devices, it is also important to have perfect power sources for those devices. IBM Linux watch 1.0, released in 2000, showed many advances in mobile computing. Since then a rapid growth has been recorded in the smart devices, which run not only algorithm but also connected with the Internet [80–82]. These smart devices offer plenty of applications while following strict size constraints, which also possess a great challenge for the power supply. The developments of Li-ion battery technology offer great possibilities. On the other hand, heavy electronics and power grids also need large grid-based energy storage devices [83, 84]. In heavy electronics, Na-ion batteries can be an alternative of Li-ion because of the abundance of Na in the nature [85]. The demands for high energy density, with relatively low-cost energy storage devices are proliferating and current commercial batteries will not be able to fulfill the requirement. The first successful incorporation of graphite in commercial Li-ion battery was introduced by Sony Corporation in 1991 [86]. Graphite has been the dominant anode materials in Li-ion battery industry since then due to its relatively low lithium

intercalation voltage. However, only a single lithium can be intercalated in a six-carbon ring, which results in theoretical capacity of 371 mAh/g and further limits the energy density. Secondly, graphite works well for Li-ion battery but in the case of Na-ion, it shows much less specific capacity due to the bigger size of Na, which creates more specific requirements for electrode materials than those of Li-ion batteries [87]. In order to extend the effective use of energy storage devices from portable devices to large-scale energy storage, solar cells and electric vehicles, further breakthrough in Li or Na-ion battery are imperative [87].

The main challenge is to develop the profound understanding of electrolytes and electrode materials that will allow us to identify the alternative energy storage strategies. In this regard, ultrathin 2D materials have shown numerous advantages for electrochemical energy storage because of the highly accessible surface area, tunable electronic properties and fast charge transfer kinetics [88]. The volume changes get relaxed during the insertion and de-insertion process of Li/Na atoms in 2D electrode materials due to the vdW stacked formations. Additionally, the large surface area apparently provides a higher theoretical capacity compared to that of bulk form [89, 90]. For example, graphene nanoflake produced via liquid phase exfoliation manifests higher Li intake as LiC_2 than the graphite and yields specific capacity up to 1500 mAh/g [32]. Furthermore, reduced graphene oxide (rGO) shows the specific capacity of 1000 mAh/g, although it results poor reversibility in comparison to graphene nanoflake [91]. Beyond graphene, BP exhibits exceptionally high specific capacity as 2596 mAh/g, but suffers from poor cycling stability due to the large intake of Li from P to Li_3P [92]. Sun *et al.* readdressed this issue in BP, and with ball milling approach they synthesized BP flake with graphene flake. Further, this showed exceptionally high specific capacity as 2786 mAh/g and improved capacity retains 80% after 100 cycles [93]. TMDCs have also shown quite high specific capacity both in theory and experiment with good cycling capacities [94]. In the series, recently synthesized Mxenes have shown potential for Li and Na ion battery both in experiments and theory [18, 95–97]. Recent applications of 2D materials in rechargeable batteries has delivered the significant promise, including enhancements in capacity retention, rate capability, and specific capacities.

However, the key issue here is the stability of these materials, which are often doubted from practical perspective (ambient gas/2D surface interaction). It is reasonable due to the high surface to volume ratio, that nearly 100% of forming atoms in the crystal lattice are directly exposed to ambient environment. Therefore, it is crucial to think how 2D materials perform when surface molecular interactions take place. However, the stability of 2D layers can be improved through the surface functionalization, molecular decoration and tectonics. This can further change the properties of the 2D materials in ways that can offer various options for a broad range of applications.

1.1 Thesis Outline

In this thesis, mainly density functional theory (DFT) and non-equilibrium Green's function (NEGF) based methods have been used to investigate the structural, electronic and transport properties of 2D materials and their applications in nanoscale devices, gas sensing and rechargeable battery electrode. The thesis is arranged in three main parts. Part I includes the introduction in Chapter 1, and a brief description of the DFT, NEGF formalisms, and computational methods are given in Chapter 2. The part II of this thesis is dedicated to the summary of the results produced during the doctoral work. This part contains three chapters: Chapter 3, 4, and 5. Chapter 3 mainly discusses the nanoscale device application of the 2D materials, where lateral and vertical heterostructures have been explored. We have specifically evaluated graphene-hBN lateral heterostructure nanogap for DNA sequencing application. Secondly, the symmetrically stacked and twisted bilayer BP is discussed. Its application in nanojunction form for rectifying diode application has been explored. In Chapter 4, mainly the 2D materials beyond the graphene are discussed for structural, electronic, and transport properties. We have investigated the newly synthesized various polymorph of 2D boron and further one of them has been used to check the suitability in gas sensing application. In the end, the effect of substitutional doping in structural, electronic and transport in BP has been studied. Furthermore, its behavior with different gas molecule adsorptions has been discussed. Chapter 5 is dedicated to energy storage application of 2D materials, where we have investigated the different 2D materials for rechargeable battery anode. At first, brief description of modeling methodologies is given, after that different cases such as Si_2BN , B_2H_2 , BH, two different form of sulfur functionalized Mxene (Ti_2NS_2 , V_2NS_2) have been discussed for Li and Na-ion insertion potential, diffusion barrier and stability. Final remarks on the thesis are arranged in part III. The conclusion and outlook has been shown in Chapter 6 and the summary of this thesis in Swedish is given in Chapter 7. For details of the methods and discussion of results, the readers are encouraged to read the original paper and manuscripts attached at the end of the thesis.

2. Theoretical background

Density functional theory (DFT) has made its way to the central stage in quantum chemistry and condensed matter physics. The main reason behind this is the accuracy and computational economy of the calculations, which make the choice of DFT natural and practical. In this chapter, we elucidate the theoretical background of the DFT and the computational method, which has been employed during the electronic structure and transport calculations in the thesis. In the first part of this chapter, an overview of the main theorems behind the DFT is presented. Further, a brief description of the application of the DFT for atomic scale calculations is given, as employed for the electronic structure calculations in this thesis. The chapter ends with a glimpse of theory, describing electron transport with quantum transport theory based on non-equilibrium Green's function (NEGF).

2.1 The many-body problem

Materials consist of electrons and nuclei, hence the fundamental basis for understanding materials and their properties ultimately depends upon understanding the electronic structure. To describe the electronic structure, one needs to understand the underlying quantum mechanics: how a large number of electrons interacts with each other and atomic nuclei? their properties can be obtained by solving a many-body equation, described as Schrödinger equation:

$$\hat{H}\Psi(\mathbf{r}_1, \mathbf{r}_2, \dots, \mathbf{R}_1, \mathbf{R}_2, \dots) = E\Psi(\mathbf{r}_1, \mathbf{r}_2, \dots, \mathbf{R}_1, \mathbf{R}_2, \dots), \quad (2.1)$$

where $\Psi(\mathbf{r}_1, \mathbf{r}_2, \dots, \mathbf{R}_1, \mathbf{R}_2, \dots)$ is a wavefunction, which corresponds to the positions of electrons, \mathbf{r}_i , and the nuclei \mathbf{R}_I . In other words, Ψ contains all the information that can be possibly known about a system under consideration. Further, E is the energy of the system described by Ψ and \hat{H} represents the Hamiltonian of the interacting system, which can be explicated as:

$$\hat{H} = \underbrace{-\frac{\hbar^2}{2m_e} \sum_i \nabla_i^2}_{\hat{T}_e} - \underbrace{\frac{\hbar^2}{2} \sum_I \frac{\nabla_I^2}{M_I}}_{\hat{T}_n} + \underbrace{\frac{1}{2} \sum_{i \neq j} \frac{e^2}{4\pi\epsilon_0 \mathbf{r}_{ij}}}_{\hat{V}_{ee}} - \underbrace{\sum_{i,I} \frac{e^2 Z_I}{4\pi\epsilon_0 \mathbf{R}_{iI}}}_{\hat{V}_{en}} + \underbrace{\frac{1}{2} \sum_{I \neq J} \frac{e^2 Z_I Z_J}{4\pi\epsilon_0 \mathbf{R}_{IJ}}}_{\hat{V}_{nn}}. \quad (2.2)$$

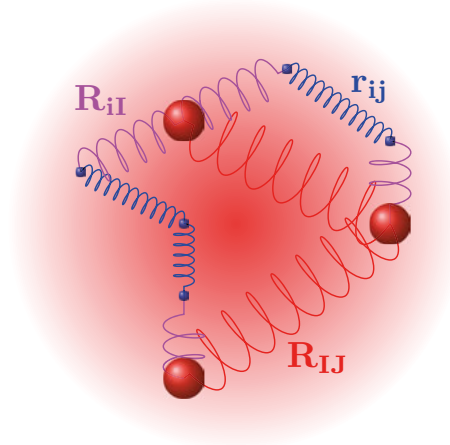


Figure 2.1. Schematic representation of randomly positioned atoms and electrons in a many body system. Big (red) and small (blue) balls describe atoms and electrons, respectively. The springs red, blue and magenta show the interaction between nuclei-nuclei, electron-electron and electron-nuclei respectively, (sizes are in imaginary scale).

Here m_e and M_I are the mass of the i^{th} electron and I^{th} nucleus, respectively. Z_I is the atomic number of the I^{th} atom. The first two terms in the equation are the kinetic energy of the electron and nuclei. Later three terms describe the potential energy from the Coulomb interaction between electron-electron, electron-nucleus, and nucleus-nucleus, respectively. The analytical solution for the equation mentioned above is limited to the simple systems, for example, hydrogen atom and molecule. To broaden its applicability in practically interesting systems like solids where a large number of particles need to be considered, approximations have to be made. The first approximation utilizes the large mass differences between the nuclei and the electrons (proton-to-electron mass ratio is slightly more than 1836). This makes the nuclei static relative to motion of electrons, hence the dynamics of nuclei could be neglected by considering them frozen (or very slow) related to electrons. This is the basis of Born-Oppenheimer approximation (BOA) [98], which allows us to separate the electronic and ionic degrees of freedom. The total wavefunction in Eq. (2.1) can thus be rewritten as a product of wave functions for electrons and ions as

$$\Psi(\mathbf{r}_1, \mathbf{r}_2, \dots, \mathbf{R}_1, \mathbf{R}_2, \dots) = \psi(\mathbf{r}_1, \mathbf{r}_2, \dots) \psi(\mathbf{R}_1, \mathbf{R}_2, \dots). \quad (2.3)$$

The above simplification reduces the initial problem to a purely electronic problem, where the nuclei coordinates enter only as parameters. Considering the nuclei as static, the last term of Eq. (2.2) can be treated as a constant-valued term and the kinetic energy of the nuclei, i.e., the second term of Eq.

(2.2) vanishes. Therefore, the many body Hamiltonian can be recast as

$$\hat{H} = \underbrace{-\frac{\hbar^2}{2m_e} \sum_i \nabla_i^2}_{\hat{T}_e} + \underbrace{\frac{1}{2} \sum_{i \neq j} \frac{e^2}{4\pi\epsilon_0 r_{ij}}}_{\hat{V}_{ee}} - \underbrace{\sum_{i,I} \frac{e^2 Z_I}{4\pi\epsilon_0 R_{iI}}}_{\hat{V}_{en}}. \quad (2.4)$$

Here the kinetic energy of nuclei is neglected and nuclear repulsion contributes as a constant to the total energy. Although use of this approximation does not help us to get simplified solution of the many body Schrödinger equation. The problem of solving this equation of interacting N electron system still persists.

The use of BOA simplifies the many body Hamiltonian involving ions and electrons to a many body Hamiltonian involving electrons only. However, the solution of the electronic Hamiltonian in Eq. (2.4) is still cumbersome because one has to solve the second-order differential equations for N electrons. The latter task is theoretically possible only for systems where the number of electrons is small, e.g., hydrogen atom. Once the number of electrons gets higher, the solution of the Hamiltonian is practically impossible. Therefore, one must look for another way to solve the many body problem by restricting the number of degrees of freedom. To this end, one way is to consider the density of electrons instead of positions. In the next section, we discuss the density functional theory that involves the many body Hamiltonian (energy) as a function of density.

2.2 Density functional theory

The foundation of density functional theory (DFT) is based on the fact that the property of interacting electron systems can be described via functional of its ground state density instead of the many body wave functions. Thomas and Fermi proposed the very first illustration of DFT for quantum system based on the non-interacting homogeneous electron density [99, 100]. However, their consideration of simple approximation lacked with the accurate description of electrons in the many body system, which resulted in its failure. Thereafter, density functional formalism as we know today was born with the landmark paper of Hohenberg and Kohn [101], which introduced an exact theory of interacting many body systems. The theorems proven in this report represent the major theoretical pillars on which all modern day density functional theories are erected.

2.2.1 Hohenberg-Kohn theorem

Hohengberg and Kohn established a solid foundation to DFT through their theorems, shown that the properties of interacting system can be calculated by

using the ground state density. These theorems are the core concept of DFT which are described below.¹

Theorem I

For any system of interacting particles in an external potential $V_{\text{ext}}(\mathbf{r})$, the potential $V_{\text{ext}}(\mathbf{r})$ is determined uniquely, up to a constant, by ground state density, $n_0(\mathbf{r})$.

The first theorem only furnishes the existence of a functional of electron density as basic variable but the true form of this function is not exactly known. The second theorem defines the property of the functional.

Theorem II

Universal functional for the energy $E[n]$ in terms of density $n(\mathbf{r})$ can be defined for any external potential V_{ext} . For any particular V_{ext} , the ground state energy of the system is the global minimum of the energy functional, and the density $n(\mathbf{r})$ which minimizes the functional is the exact ground state density $n_0(\mathbf{r})$.

We do not intend to provide a heuristic proof of these theorems as it can be found in textbooks on DFT [102–104]. Combining these two theorems, the energy functional can be written as

$$E_{HK}[n] = F_{HK}[n] + \int d^3r V_{\text{ext}}(\mathbf{r})n(\mathbf{r}). \quad (2.5)$$

Here F_{HK} defines all the internal energies including kinetic and potential energies. The total internal energy functional is expressed as

$$F_{HK}[n] = T[n] + E_{\text{int}}[n]. \quad (2.6)$$

The above equation does not depend on the external potential and only depends upon the density. Hence this functional must be universal by its construction. But in the theorem there are no any means to determine the exact form of the functional and hence it has to be approximated in order to apply in practical systems (Calculations). The global minimum of the functional in (2.6) is the exact ground state total energy of the system E_0 and particle density which minimizes this functional would be the exact ground state density $n_0(\mathbf{r})$. Using the variational principle, one can determine the ground state density as

$$\left. \frac{\delta}{\delta n} E_{HK}[n(\mathbf{r})] \right|_{n=n_0} = 0. \quad (2.7)$$

The HK theorems proved to be the bedrock of the modern DFT. These theorems describe the unique mapping between ground state density and ground

¹These theorems are directly taken from ref. [102]

state energy. However, they do not present any recommendation on how the functional (which delivers the ground state energy) can be formulated. Further, Kohn-Sham in their formalism established the concept of a non-interacting reference system built from a set of orbitals such that the major part of the kinetic energy can be computed to good accuracy.

2.2.2 Kohn-Sham Formalism

The two HK theorems were capable of solving the many body problem using the particle density function and variation principle. However, for practical applications, the realization of DFT was first proposed by Kohn and Sham (KS) [105]. The essential modification proposed in HK theorem is the replacement of interacting electron system with an auxiliary system of non interacting particles having the same density. Thus, the total energy functional can be written as

$$E_{KS}[n] = T_s[n] + \int d^3r V_{ext}(\mathbf{r})n(\mathbf{r}) + \frac{1}{2} \int d^3r d^3r' \frac{n(\mathbf{r})n(\mathbf{r}')}{|\mathbf{r} - \mathbf{r}'|} + E_{xc}[n]. \quad (2.8)$$

The first three terms represent the functional for the kinetic energy of a non-interacting electron gas, the external potential contribution due to nuclei and other external potential and the classical Coulomb contribution (Hartree term) for the electron-electron interaction, respectively. The last term, $E_{xc}[n]$, contributes towards all the many body effects of exchange interactions and correlations, also known as exchange and correlation functional. The analytical expression of the functional, $E_{xc}[n]$ is still unknown and the implementation of the KS formalism counts on the ability to find a good approximation for it. Here the Coulomb repulsion in between the nuclei is directly added as a constant term in the Eq. (2.8)

According to the second HK theorem, the solution of the KS auxiliary system can be done as the minimization of the KS energy functional with respect to the density $n(\mathbf{r})$. The minimization of energy results in a Schrödinger-like equation

$$\hat{H}_{KS}\psi_i(\mathbf{r}) = \left[-\frac{\hbar^2}{2m_e}\nabla^2 + V_{KS}(\mathbf{r}) \right] \psi_i(\mathbf{r}) = \varepsilon_i \psi_i(\mathbf{r}), \quad (2.9)$$

where $\psi_i(\mathbf{r})$ are the KS orbital, ε_i are the eigenvalues. V_{KS} is the effective potential that can be defined as

$$V_{KS}(\mathbf{r}) = V_{ext} + \int d^3r' \frac{n(\mathbf{r}')}{|\mathbf{r} - \mathbf{r}'|} + V_{xc}. \quad (2.10)$$

Moreover, the exchange correlation potential can be defined by

$$V_{xc} = \frac{\delta E_{xc}[n]}{\delta n(\mathbf{r})}. \quad (2.11)$$

It must be noted that the KS orbitals, $\psi_i(\mathbf{r})$, are not the wave functions of electrons, in fact they do not have any direct physical interpretation. They are the auxiliary functions for calculating electron density, which is described as follows

$$n(\mathbf{r}) = \sum_i |\psi_i(\mathbf{r})|^2. \quad (2.12)$$

The KS formalism is exact and would lead to the exact ground state of an interacting many body system, provided that the true form of E_{xc} is known. Note that the effective potential in Eq. (2.10) depends on the electron density. The latter, in turn, depends on the KS orbitals which are being searched within KS formalism. Therefore, the KS equations has to be solved self-consistently following an iterative method. At the end, the self-consistent solution ensures that the true ground state density has been achieved.

2.3 Exchange-correlation functionals

As previously discussed, Kohn-Sham formalism replaces the real system with an auxiliary non-interacting system and accommodates unknowns in the exchange and correlation functional. Therefore, the KS formalism is exact, only when the form of E_{xc} is exactly known. The accuracy of DFT calculations exclusively relies on the accuracy of the chosen form of E_{xc} . However, the question of finding the best approximation for exchange and correlation potential is itself a research problem that is still unsolved. The approximations of this functional need to be made with respect to the energy of exact ground state. In the following section, we describe the most commonly used approximation for the exchange-correlation functional.

2.3.1 Local density approximations

Local density approximations (LDA) was the first approximation proposed by Kohn and Sham, when they introduced their formalism [105]. In this approximation, the exchange-correlation energy density has been treated locally as a homogeneous electron gas. The reason for considering the homogeneous electron gas is that it has the simplest form of exchange-correlation functional, which works quite well for many systems and it is described as

$$E_{xc}^{LDA} = \int n(\mathbf{r}) \epsilon_{xc}^{hom}[n(\mathbf{r})] d\mathbf{r}, \quad (2.13)$$

where ϵ_{xc}^{hom} defines the exchange correlation energy density of a homogeneous electron gas with the density $n(\mathbf{r})$ calculated locally at a point \mathbf{r} . The ϵ_{xc}^{hom} can further be divided into two parts of exchange ϵ_x and correlation ϵ_c terms. The exchange part can be computed simply from analytical approach but correlation part is again not known. Thus, the numerical form of ϵ_c is used, which

comes from whole range of Monte-Carlo calculations combined with different interpolation schemes [106]. Despite of simplicity, LDA works very well in many systems. LDA was expected to work for the systems with slowly varying density, for instance, the free electrons in metallic systems [107]. However, the recent investigations have also shown that LDA also works very well for several other systems, e.g., semiconductors and insulators and explains majority of their properties [108, 109]. A list of drawbacks of LDA follows: the LDA tends to overbind that means the computed cohesive energies are large. There is lack of enough localization of electrons in the space, which is appropriate for s and p electrons, but not good for d and f electrons. The long-range effects like van der Waals bonds are lacking, owing to the overly local nature of the LDA. At last, the potential felt by an electron while approaching an atom/surface is shoddily stipulated by the LDA. The hydrogen bond, is also poorly reckoned for.

2.3.2 Generalized gradient approximations (GGA)

The improvement in LDA was proposed by Hohenberg and Kohn [101], where they proposed to include the gradient of the local density in the expression for the exchange and correlation. The latter provided the cornerstone of the GGA [110, 111], where the exchange-correlation density not only depends on the electronic density $n(\mathbf{r})$, but also on the gradient of the electronic density $\nabla n(\mathbf{r})$. Mainly, the exchange-correlation energy in GGA is obtained by modifying the LDA energy density and can be written as

$$\begin{aligned} E_{xc}^{GGA} &= \int n(\mathbf{r}) \epsilon_{xc}^{GGA}[n(\mathbf{r}), \nabla n(\mathbf{r})] d\mathbf{r} \\ &= \int \epsilon_x^{hom} n(\mathbf{r}) F_{xc}[n(\mathbf{r}), \nabla n(\mathbf{r})] n(\mathbf{r}) d\mathbf{r}, \end{aligned} \quad (2.14)$$

where ϵ_x^{hom} is the exchange energy density of a uniform electron gas of density equal to $n(\mathbf{r})$. F_{xc} is a dimensionless quantity that is a function of density and its gradient. F_{xc} can further separated in the two parts as exchange and correlations. The exchange part has been proposed to have several forms such as Perdew, Burke and Ernzerhof (PBE) [112] and Becke (B88) [113]. Let us make a small comparison between LDA and GGA schemes. Even though LDA describes the physical properties for a wide range of systems, it fails to describe the chemical properties, e.g., binding energies in particular [114]. The consideration of GGA has overcome such failures of LDA. GGA provides a more realistic description for the chemical energy barrier in metallic and semi-conducting surfaces [115, 116]. Apart from this, GGA also faces problems in describing long-range effects, such as Van der Waals. However, hydrogen bonds are generally well justified.

2.4 Electronic structure of periodic solids

So far, we have discussed the method, which is applicable for the system with finite number of electrons, like atoms and molecules. However, there are infinite number of electrons in a periodic model of a crystal. The above mentioned DFT approximations cannot directly be used in such crystals, hence, further developments are requisite. One of the development is to use periodic boundary conditions. The periodicity in a crystal makes its potential also periodic in nature, hence, the effective potential in the KS equation will follow the crystal periodicity as

$$V_{eff}(\mathbf{r} + \mathbf{R}) = V_{eff}(\mathbf{r}), \quad (2.15)$$

with \mathbf{R} as a translation vector. Using the Bloch theorem [117, 118], we can write the single particle wavefunction

$$\psi_{\mathbf{k}}(\mathbf{r}) = e^{i\mathbf{k}\mathbf{r}} u_{i\mathbf{k}}(\mathbf{r}), \quad (2.16)$$

where $u_{i\mathbf{k}}(\mathbf{r})$ is periodic function in the lattice, which means $u_{i\mathbf{k}}(\mathbf{r}) = u_{i\mathbf{k}}(\mathbf{r} + \mathbf{R})$. \mathbf{k} stands for the wave vector. One can express the periodic function $u_{i\mathbf{k}}(\mathbf{r})$ in Fourier series, using the reciprocal lattice vector \mathbf{G} and plane wave expansion coefficient $c_{i\mathbf{G}}$ as

$$u_{i\mathbf{k}}(\mathbf{r}) = \sum_{\mathbf{G}} c_{i\mathbf{G}} e^{i\mathbf{G}\cdot\mathbf{r}}. \quad (2.17)$$

Note that due to the periodicity, the following condition has to be obeyed: $\mathbf{G} \cdot \mathbf{R} = 2\pi m$, with m being an integer that defines the periodicity of the system. Further, the single particle wave function can be written as a linear combination of plane waves

$$\psi_{i\mathbf{k}}(\mathbf{r}) = \sum_{\mathbf{G}} c_{i\mathbf{k}+\mathbf{G}} e^{i(\mathbf{k}+\mathbf{G})\cdot\mathbf{r}} \quad (2.18)$$

This reduces the infinite solid problem (infinite number of electrons) to infinite number of k -points, which might seem somewhat contradicting. Nevertheless, it allows the great simplification because $\psi_{i\mathbf{k}}(\mathbf{r})$ changes smoothly along the close k -points hence by considering only one k -point, the small region can be sampled. This implies that considering the discrete k -point grid in order to calculate the electronic structure of solid is sufficient.

2.5 Pseudopotentials

Along with the proper treatment of exchange-correlation functional, the solution of the Kohn-sham equation is feasible for the electronic systems. Further, for bigger systems having a higher number of electrons, it becomes computationally expensive. One solution could be use to decrease the number of effective electrons in the system. The reduction of electrons effectively introduces the concept of pseudopotential. The basic idea of the pseudopotential

is to replace the existing problem with another problem. It deals with the valence electrons of the system and replaces the strong Coulomb potential of the nucleus and effect of tightly bound core electron to an effective ionic potential acting on the valence electron. The wave function of the core atom does not change significantly with the environment of the parent atom. These core electrons and nucleus are also associated with rapidly varying wave function with many nodes. Therefore, the large number of basis functions are required to describe them. Accordingly, it is useful to combine these two (nucleus and core electrons), and only deal with the valence electrons. The core electrons screen the external potential and provide a softer potential to the valence electrons. To understand the construction of the pseudopotential, let us first consider the

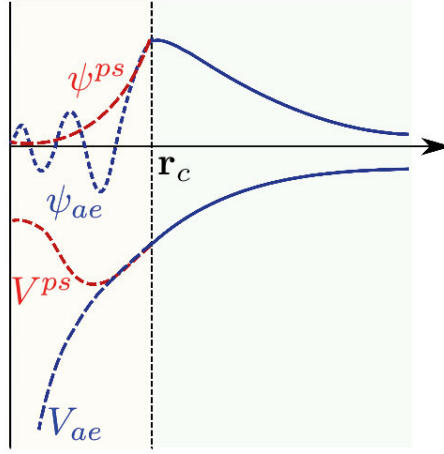


Figure 2.2. Schematic of a pseudopotential V^{ps} and respective wave function ψ^{ps} , where pseudo wave function is node less and matches well with all-electron wave function ψ^{ae} over the cut off radius r_c . This induces the much softer potential (pseudo) than the all-electron potential $V^{ae} = -\frac{Z}{r}$.

exact core and valence states, as $|\psi_c\rangle$ and $|\psi_v\rangle$ and Schrödinger equation can be written as

$$\hat{H}|\psi_i\rangle = E_i|\psi_i\rangle, \quad (2.19)$$

where i defines both the valence and core states. We are interested to get smoother valence states in the core region. Defining a smooth pseudo-state $|\psi^{ps}\rangle$, we can write

$$|\psi_v\rangle = |\psi^{ps}\rangle + \sum_c |\psi_c\rangle \alpha_{cv}, \quad (2.20)$$

where $\alpha_{cv} = -\langle\psi_c|\psi^{ps}\rangle$ defines that valence band has to be orthogonal to all of the core states. Further, using Eqs. (2.19) and (2.20) one can get,

$$\hat{H}|\psi^{ps}\rangle + \sum_c (E_v - E_c) |\psi_c\rangle \langle\psi_c|\psi^{ps}\rangle = E_v |\psi^{ps}\rangle \quad (2.21)$$

$$\implies \hat{H}^{ps} |\psi^{ps}\rangle = E_v |\psi^{ps}\rangle. \quad (2.22)$$

The last Eq. is analogous to the Schrödinger equation with a pseudo Hamiltonian and pseudopotential

$$\hat{H}^{ps} = \hat{H} + \sum_c (E_v - E_c) |\psi_c\rangle \langle \psi_c| \quad (2.23)$$

$$\hat{V}^{ps} = \hat{V}_{eff} + \sum_c (E_v - E_c) |\psi_c\rangle \langle \psi_c| = \hat{V}_{eff} + \hat{V}_{nl}. \quad (2.24)$$

The first term in Eq. (2.24) describes the true potential. The second term stands for repulsive potential localized to the core region. Therefore, it cancels the strong attractive nuclear Coulomb potential and softens the core potential. It results in a weaker pseudopotential and nodeless pseudo wavefunction.

2.6 Basis sets

Undoubtedly, an excellent and relatively cheaper alternative to wave function methods is KS-DFT. As described earlier, this scheme replaces the calculation of true wave function ψ by that of a single Slater determinant that represents a non-interacting model system, resulting the same ground state energy as of ψ . But, the implementation of the KS-DFT method still faces several numerical difficulties as the behavior of the wave function is not same everywhere. In fact it is seen in Fig. 2.2 that the wave function has different shapes in different regions of space, i.e., the core and valence regions. Henceforth, choosing the appropriate basis set, which can describe the wave function in all the regions of space, is the key requirement to obtain the accuracy in the results. There are number of choices for the basis sets depending upon the system under investigation and required accuracy. Some examples of these basis sets are: plane waves (PW), linearized augmented plane waves (LAPW), linear muffin tin orbital waves (LMTO), linear combination of atomic orbitals (LCAO) etc. [102–104]. However, there are several other basis sets proposed and used in the literature mostly in quantum chemistry [119]. Below, we discuss briefly about the PW and LCAO as the results presented in the thesis are mostly produced by using these two basis sets.

2.6.1 Plane waves

Plane wave (PW) basis set is a natural choice to solve the KS equations for the periodic system, such as bulk solids [120, 121]. PW method has been widely used and optimized and also implemented for *ab initio* calculation for periodic solid [122]. In KS-DFT the electrons moving in an effective potential of a periodic lattice can be described by the Eqs. (2.9) and (2.10). Hence, the KS orbitals ψ can be written as a product of the function $u_{\mathbf{k}}(\mathbf{r})$ such that the periodicity is followed according to Eqs. (2.16) and (2.17).

If the PW basis set is used, the periodic function $u_{i\mathbf{k}}(\mathbf{r})$ can be expressed as sum over the plane waves, which would have same periodicity as it. Such plane waves are those ones corresponding to the reciprocal lattice vectors. Hence, the KS orbitals can be written in a linear combination of the plane waves as

$$\psi_{i\mathbf{k}}(\mathbf{r}) = \sum_{\mathbf{G}} c_{i\mathbf{k}}(\mathbf{G}) \times \frac{1}{\sqrt{\Omega}} e^{i(\mathbf{k}+\mathbf{G})\cdot\mathbf{r}}, \quad (2.25)$$

where $c_{i\mathbf{k}}$ is the expansion coefficient of the wave function in the plane wave basis set $e^{i(\mathbf{k}+\mathbf{G})\cdot\mathbf{r}}$ and \mathbf{G} are the reciprocal lattice vector. Here, the states are normalized and follow the periodic boundary condition in a large volume Ω , which is allowed to reach up to infinity. Thus, $\frac{1}{\sqrt{\Omega}}$ serves as a normalization factor. \mathbf{k} stands for Bloch wave vector. Further, the KS equation can be written as

$$\hat{H}_{KS}\psi_i(\mathbf{r}) = \left[-\frac{\hbar^2}{2m_e}\nabla^2 + V_{KS}(\mathbf{r}) \right] \psi_i(\mathbf{r}) = \varepsilon_i \psi_i(\mathbf{r}). \quad (2.26)$$

Using Eq. (2.25) into (2.26) and left multiplication with $e^{-i(\mathbf{k}+\mathbf{G}')\cdot\mathbf{r}}$, further, integration over \mathbf{r} would give the matrix eigenvalue equation as:

$$\sum_{\mathbf{G}'} \left(\frac{\hbar^2}{2m_e} |\mathbf{k} + \mathbf{G}'|^2 \delta_{\mathbf{G}',\mathbf{G}} + V_{KS}(\mathbf{G} - \mathbf{G}') \right) c_{i\mathbf{k}}(\mathbf{G}') = \varepsilon_{i\mathbf{k}} c_{i\mathbf{k}}(\mathbf{G}). \quad (2.27)$$

Note that the kinetic energy, i.e., the first term is diagonal and the potential energy V_{KS} is defined in terms of its Fourier transform. The solution is obtained by diagonalization of a Hamiltonian matrix and the size of the matrix is determined by choice of the cut off energy, $E_{cut} = \frac{\hbar^2}{2m_e} |\mathbf{k} + \mathbf{G}|^2$. The size of the matrix becomes intractably large for systems that contain both the valence and core electrons. This makes the calculation computationally expensive and the problem can be solved by using the pseudopotential approximations. There are several advantages of PW basis sets like, it does not depend on the system as a result it is easy to compute and compare the properties. PW has good control referring to accuracy and convergence, since it is easy to increase the number of plane waves in the calculation. The Schrödinger equation can be solved efficiently because the fast Fourier transform algorithm can adequately compute the expansion co-efficients.

2.6.2 Projector augmented wave

A significant part of the results presented in this treatise, the electronic structure calculations and geometry relaxations have been performed using the projector augmented wave (PAW) method, implemented in VASP [123]. It is predominantly an all-electron frozen core method, which consists the simpler energy and potential independent basis but retains the flexibility of augmented

wave method [124]. The behavior of the wave function differs with the distance from the nucleus (core and valence region) as can be seen in Fig. 2.2. Since the full wave function vary rapidly near the nucleus and remains uniform outside of the centered sphere, all the integrals are evaluated as a combinations of integrals of smooth functions extending throughout the space plus localized contributions described by radial integrals over the muffin tin sphere. Essentially, the method is based on the linear transformation \mathfrak{S} , which describes the relation between all-electron single particle KS wave function ψ_n and computationally convenient smooth wave function $\tilde{\psi}_n$ as

$$|\psi_n\rangle = \mathfrak{S} |\tilde{\psi}_n\rangle . \quad (2.28)$$

The index n stands for the bands, \mathbf{k} -points and spins. We can use the variational principle with respect to auxiliary wave function and write the transformed KS equation as follows,

$$\mathfrak{S}^\dagger H \mathfrak{S} |\tilde{\psi}_n\rangle = \mathfrak{S}^\dagger \mathfrak{S} |\tilde{\psi}_n\rangle \varepsilon_n , \quad (2.29)$$

where $\mathfrak{S}^\dagger H \mathfrak{S}$ stands for pseudo Hamiltonian \tilde{H} and $\mathfrak{S}^\dagger \mathfrak{S} = \tilde{O}$ is the overlap operator. The objective of this transformation is to avoid the nodal structure of true wave function in the core region having radius r_c . Therefore, the modification of the wave function in the core region would be governed by

$$\mathfrak{S} = 1 + \sum_R S_R , \quad (2.30)$$

with S_R as deduction between the auxiliary wave function from all-electron wave function and R is the atom site index. The S_R acts within the augmented region, which is basically the core radius as $r_c \in R$. The core wave function is then limited to augmented region and it is treated separately using frozen core approximation. Hence, the \mathfrak{S} operates on valence wave function, which can be written within the augmented space as

$$\psi(\mathbf{r}) = \sum_{i \in R} \phi_i(\mathbf{r}) c_i , \quad (2.31)$$

where $\phi_i(\mathbf{r})$ is the all-electron partial wave solution of the radial Schrödinger equation for the isolated atom and c_i are the expansion coefficients. These partial wave $\phi_i(\mathbf{r})$ are locally mapped to corresponding auxiliary partial wave function $\tilde{\phi}_i(\mathbf{r})$ by the transformation \mathfrak{S} ,

$$\begin{aligned} |\phi_i\rangle &= (1 + S_R) |\tilde{\phi}_i\rangle \\ \implies S_R |\tilde{\phi}_i\rangle &= |\phi_i\rangle - |\tilde{\phi}_i\rangle \quad \forall i \in R. \end{aligned} \quad (2.32)$$

It is worth reminding that due to the local transformation, these $\tilde{\phi}_i$ and ϕ_i are identical outside the augmented region. Once we have the realistic all-electron

wave function and smooth wave function, they can further be expanded into the all-electron partial and pseudo partial wave function ($\phi_i = \tilde{\phi}_i \ \forall i \in R$). Hence, any auxiliary wave function can be formed with an auxiliary partial wave basis within the augmented region as

$$\tilde{\psi}(\mathbf{r}) = \sum_{i \in R} \tilde{\phi}_i(\mathbf{r}) c_i = \sum_{i \in R} \tilde{\phi}_i(\mathbf{r}) \langle \tilde{p}_i | \tilde{\psi} \rangle, \quad (2.33)$$

where $\langle p_i |$ is the projector operator and satisfies the conditions for completeness and orthogonality

$$\sum_{i \in R} |\tilde{\phi}_i\rangle \langle \tilde{p}_i| = 1 \quad (2.34)$$

$$\langle \tilde{\phi}_i | \tilde{p}_j \rangle = \delta_{ij} \quad \forall i, j \in R. \quad (2.35)$$

Thus, using Eqs. (2.30) and (2.32), the transformation operator can finally be expressed in terms of auxiliary and the true partial waves as

$$\begin{aligned} \mathfrak{S} &= 1 + S_R \sum_i |\tilde{\phi}_i\rangle \langle \tilde{p}_i| \\ &= \left(1 + \sum_i (|\phi_i\rangle - |\tilde{\phi}_i\rangle) \langle \tilde{p}_i| \right). \end{aligned} \quad (2.36)$$

Note that the involved sum runs over all the partial waves corresponding to all the atoms. Further, following the Eq. (2.28), the true wave function can be obtained as

$$\begin{aligned} |\psi\rangle &= |\tilde{\psi}\rangle + \sum_i (|\phi_i\rangle - |\tilde{\phi}_i\rangle) \langle \tilde{p}_i | \tilde{\psi} \rangle \\ &= |\tilde{\psi}\rangle + \sum_R (|\psi_R^1\rangle - |\tilde{\psi}_R^1\rangle), \end{aligned} \quad (2.37)$$

where we can define, $|\psi_R^1\rangle = \sum_{i \in R} |\phi_i\rangle \langle \tilde{p}_i | \tilde{\psi} \rangle$ and $|\tilde{\psi}_R^1\rangle = \sum_{i \in R} |\tilde{\phi}_i\rangle \langle \tilde{p}_i | \tilde{\psi} \rangle$. As a result of this transformation, the wave function is partitioned into the different part of space. Inside the core region, we see partial waves that holds the nodal structure, i.e., $|\tilde{\psi}_R\rangle = |\tilde{\psi}_R^1\rangle$, which describes the true function $|\psi_R\rangle$ merging in to $|\tilde{\psi}_R^1\rangle$. Away from the augmented space, the auxiliary and true wavefunctions are the same, i.e., $|\psi_R\rangle = |\tilde{\psi}_R\rangle$. Although the PAW method consists of some approximations like *frozen core approximation*, the expansion of auxiliary wave function with finite number of plane waves and so on. Despite of these facts, PAW methods gives access to full electron wave function, charge and spin densities with adequate basis sets.

2.6.3 LCAO basis set

In the plane wave basis, the number of plane waves needed for calculation is generally much higher than the number of electrons. Therefore, it demands

high computational resources for the matrix operations. The plane waves are not only extended over all the space, but also over the space where there is no charge density. Thus, the plane wave methods are not suitable for grid based electronic structure calculations for large systems. The alternative route to this is provided by real space basis sets that usually have some natural physical appearance which resembles to the nature of the problem. The linear combination of atomic orbital (LCAO) is one of those. LCAO basis sets were first introduced in quantum chemistry to describe the molecular orbitals, but, they can also be used in the solid state calculations in the Order N-methods. SIESTA uses the LCAO as the basis sets for the solution of Kohn-Sham equation [125]. LCAO basis sets are the superposition of atomic orbitals (AO) and can be written as

$$\phi_{nlm} = \sum_i c_{i,nlm} \chi_{i,nlm}. \quad (2.38)$$

Here, ϕ_{nlm} is the basis orbital and $c_{i,nlm}$ are the AO coefficients and the summation is over the number of AOs, $\chi_{i,nlm}$. Further, the AOs are mostly described as Slater type orbitals (STO) and the Gaussian type of orbitals (GTO). They have the same form as the product of a radial function and spherical harmonics

$$\chi_{i,nlm}(\mathbf{r}, \Theta, \Phi) = R_{nl}(\mathbf{r}) Y_{lm}(\Theta, \Phi). \quad (2.39)$$

The radial part can further be defined differently for STO [126] and GTO [127]. The radial part defines the orbital n and spherical harmonic stands for angular momentum l and magnetic quantum number m , respectively. One has to remember that the radial function becomes zero beyond certain radius.

The accuracy of the calculations in LCAO basis sets can be increased by changing the size and shape of the basis. The basis function can be expanded using multiple zeta basis sets [128, 129]. The term zeta (ζ) describes the exponent of the STO basis function. The minimal basis set is single zeta, which describes just one electron in Hydrogen and Helium case. Further down in the periodic table, different shells in the atoms from the same row, are considered unitedly, e.g., $2sp$ ($2s$ and $2p$), $3sp, 3d$ shells. This minimal basis set is very small and cannot produce correct results, but quantitatively it is possible to get observables. Further the increase in basis set, double zeta (DZ) defines the splitting of the basis function and further triple zeta (TZ) increases the basis function by one. The increase in the basis set, in turn, increases the accuracy of the calculations. LCAO basis set can further be improved by including the polarization function that means the function with higher angular momentum. This polarization function is attributed to include the deformation induced by bond formations in molecules and solids. The polarization function has angular momentum one unit higher than the maximum occupied orbitals, e.g., p -orbital can be used for polarizing s -orbitals and d -orbital can be used for p -orbital. This polarization function denoted by P, e.g., DZ basis set becomes double zeta polarized (DZP) after addition of polarization function.

The choice of basis set can be obtained by comparing energies and geometries at different levels, but DZP provides relatively high accuracy results with a reasonable computational cost for most of the systems. We used DZP basis set for producing the results in this thesis.

2.7 Force theorem and geometry optimization

In all the reported results in this thesis, geometrical optimizations have been performed, i.e., the search for spatial equilibrium configuration in which atoms are arranged in the ground state before calculation of other properties. According to Hellmann-Feynmann theorem [102], the force due to atomic displacements can be written as

$$\mathbf{F}_I = -\frac{\partial \varepsilon}{\partial \mathbf{R}_I}, \quad (2.40)$$

with ε is the total energy of the system, which can be described as

$$\varepsilon = \frac{\langle \psi | \hat{H} | \psi \rangle}{\langle \psi | \psi \rangle}. \quad (2.41)$$

Here ψ represents the Kohn-Sham wave function, which must be normalized, hence $\langle \psi | \psi \rangle = 1$. Using Eqs. (2.40) and (2.41) we get.

$$\mathbf{F}_I = -\langle \psi | \frac{\partial \hat{H}}{\partial \mathbf{R}_I} | \psi \rangle - \langle \frac{\partial \psi}{\partial \mathbf{R}_I} | \hat{H} | \psi \rangle - \langle \psi | \hat{H} | \frac{\partial \psi}{\partial \mathbf{R}_I} \rangle. \quad (2.42)$$

At the exact ground state solution, the energy is extremal for all the possible variations of the wave functions. The latter results in the vanishing of the last two terms in the right hand side of Eq. (2.42). Therefore, the forces are determined by the terms, which is explicitly dependent upon the atomic positions, and it can be further written as

$$\mathbf{F}_I = -\langle \psi | \frac{\partial \hat{H}}{\partial \mathbf{R}_I} | \psi \rangle. \quad (2.43)$$

Thus, keeping the ψ at their ground state values, the partial derivative of the total energy with respect to the ionic position can be calculated.

Force theorem can be used for the relaxation but the two main factors affect this. First, an error due to non-self consistency and the second, the explicit dependence of the basis function on the atomic positions (in LCAO basis set). These two factors give rise to the Pulay force [130]. Therefore, one should be careful to treat the force theorem. On the other hand, the Pulay force is always zero for plane wave basis sets as they do not depend on the ionic positions. However, one should carefully treat the plane wave basis for completeness for better optimization of volume and shape. It can be done by using the large energy cutoff.

2.8 Quantum transport theory

A major portion of this thesis is devoted towards an understanding of electronic transport across nanoscale devices. Such applications involve molecular systems or nanojunction coupled with 2D electrodes or transport in periodic 2D systems. In this section, the basic equations to describe the stationary electron transport in nano structures are discussed. Here, we first define the different transport regimes based on the two characteristic lengths as momentum relaxation length (L_m) and phase relaxation length (L_ϕ). The first one defines the mean distance electron needs to travel before it original momentum lost, i.e., mean free path and the later one represents the length over which electron wave function retains information about its initial phase. If the length of the conducting object (conducting wire) is much longer than these two distances means $L \gg L_m, L_\phi$ then, one simply describes it as classical ohmic behavior where the conductance depends upon the length of the wire. Further, due to small size of the devices, quantum nature of electron needs to be considered, where the electrons behave like waves, which may result in interference effects. Using these two relevant length scales, electron transport can be divided in three parts:

- **Ballistic transport regime, $L \ll L_m, L_\phi$:**
In this case, there is no scattering in between the leads. The resistance can only arise in the contact regions. Graphene and carbon nanotube (CNT) exhibit the ballistic conductance where conductance is quantized on sub micrometer scale lengths.
- **Elastic and coherent regime, $L < L_m, L_\phi$:**
The transport can be coherent, when the length of the wire is less then the phase relaxations length. Electrons can get elastically scattered resulting the reduction in transmission without involving energy or phase change.
- **Inelastic and incoherent regime, $L > L_m, L_\phi$:**
The sufficiently large length over which incoming electrons get inelastically scattered by phonons, destroying its phase memory.

2.8.1 The Landauer formula

Landauer applied the scattering theory of transport as a conceptual framework to illustrate the electrical conductance and formulated that “*Conductance is transmission*” [131]. In this approach, two ballistic leads are connected to mesoscopic scatter (molecule or nanoscale structure) as described in Fig. 2.3. Left and right leads behave like a reservoirs with electrochemical potential

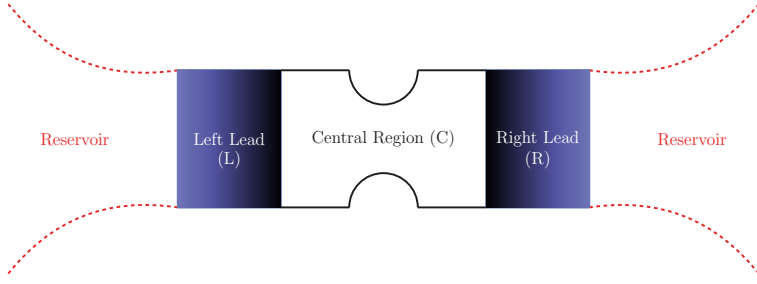


Figure 2.3. Schematic of an mesoscopic system connected with two ballistic leads as described in Landauer approach. These leads are connected with reservoir held at equilibrium at different chemical potentials μ_L and μ_R , respectively. The central region where the scattering process takes place is connected with the leads.

μ_L and μ_R where $\mu_L = \mu_R$ at zero bias voltage. Further, the electrochemical difference causes the flow of electrons from for $L \rightarrow R/R \rightarrow L$.

In his approach Landauer viewed the current flow as the probability of the electron transmitted from one lead to another. Therefore, the current can be written as

$$I = \frac{2e}{h} \int T(\epsilon) (f_L(\epsilon) - f_R(\epsilon)) d\epsilon, \quad (2.44)$$

where e is the electronic charge, h is Plank's constant, f is the Fermi Dirac distribution function and the transmission $T(\epsilon)$ is given as

$$T(\epsilon) = \sum_{i,j} t_{i-j}(\epsilon). \quad (2.45)$$

If V_b is the applied bias on the left (right) electrode symmetrically, then the electrochemical potential at the left and right electrode can be expressed as $\mu_L = E_F + eV_b/2$ and $\mu_R = E_F - eV_b/2$, respectively, where E_F defines the Fermi energy. It is clear from Eq. (2.44), the current would be zero if $f_L(\epsilon) = f_R(\epsilon)$, because only the difference can contribute to the net current. If the temperature is zero but voltage bias is finite then the current can be written as,

$$I = \frac{2e}{h} \int_{E_F - \frac{eV_b}{2}}^{E_F + \frac{eV_b}{2}} T(\epsilon) d\epsilon. \quad (2.46)$$

Consequently, the conductance $G = I/V$ can be obtained by averaging transmission $T(\epsilon)$ over the energy window of the width eV_b centered at the Fermi energy of electrode. On the other hand, if $T(\epsilon)$ does not change significantly over an energy range eV , then the Fermi function can be expanded using Taylor expansion method at $\mu = E_F$ as,

$$I = \frac{2e}{h} \int d\epsilon T(\epsilon) \left(-\frac{\partial f(\epsilon)}{\partial \epsilon} \right) (\mu_L - \mu_R). \quad (2.47)$$

Here, $(\mu_L - \mu_R) = eV$. The electrical conductance $G = I/V$ reads as

$$G = \frac{2e^2}{h} \int d\varepsilon T(\varepsilon) \left(-\frac{\partial f(\varepsilon)}{\partial \varepsilon} \right). \quad (2.48)$$

At $T = 0$ K, $-\frac{\partial f(\varepsilon - \mu)}{\partial \varepsilon} = \delta(\mu)$, where $\delta(\mu)$ is Kronecker delta. Further, for an ideal periodic chain, where $T(\varepsilon) = 1$ at $T = 0$ K, the Landauer conductance becomes

$$G_0 = \frac{2e^2}{h} = 77.5 \mu\text{Siemens} = 12.9 (\text{K}\Omega)^{-1}, \quad (2.49)$$

where G_0 is quantum conductance. Generally, in the nanodevices, its connection to the leads would not be ideal due to scattering. Hence, the formula for the conductance can be rewritten as:

$$G = G_0 T(E_F), \quad (2.50)$$

where E_F is the Fermi energy of the system.

The above description is valid for two-electrode system. However, in the device with e.g. a gate electrode, or a number of electrodes, carrying electrons, the Landauer formula in its general form should be considered

$$G = G_0 \sum_{i,j} T_{ij}(E_F). \quad (2.51)$$

In summary, the conductance calculation from Landauer formula suggests that transmission function has a central significance. In a generalized way, this transmission function can be evaluated as scattering matrix problem defined as matrix S , related to incoming Φ_{in} and outgoing Φ_{out} wave functions on the scattering potential,

$$|\Phi_{out}\rangle = S |\Phi_{in}\rangle, \quad (2.52)$$

with S is the scattering matrix, the elements of this matrix connect the incoming and outgoing states. Absolute values of each squared element of matrix yield the probability of transmission from particular incoming state to the corresponding outgoing state. Further, if these elements are arranged in the blocks representing transmission t and reflection r , then one can write it as

$$S = \begin{pmatrix} r & t \\ r^* & t^* \end{pmatrix}. \quad (2.53)$$

The indices with asterisk sign stand for the coefficient of wave function coming from the right lead. This gives us the transmission function as

$$T(\varepsilon) = \text{Tr}[t^* t], \quad (2.54)$$

where Tr stands for the trace of the matrix. To solve the general scattering problem, one should know the shape of the scattering potential and solve it for the asymptotic wave function in the leads. In this procedure only resulting scattering potential is considered, but the electronic structure in the scattering region is excluded. However, in general, the scattering potential depends on the applied bias voltage and in this way it alters the electronic structure in the scattering region.

2.9 Non-equilibrium Green's function

In this section, Generalized approach to calculate the transmission coefficient T of the electron with energy E traveling from one electrode to another using non equilibrium Green's function (NEGF) method will be discussed. A typical transport setup is divided into three parts as described in Fig. 2.3: central region (C), semi infinite left (L) and right leads (R), then, the Hamiltonian of the system is determined as

$$H = \begin{pmatrix} H_L & \tau_L & 0 \\ \tau_L^\dagger & H_C & \tau_R^\dagger \\ 0 & \tau_R & H_R \end{pmatrix}. \quad (2.55)$$

In the above mentioned equation, H_L , H_C , and H_R denote the Hamiltonian matrices of the left, center, and right components, respectively. $\tau_{L(R)}$ stands for the interaction between the left (right) electrode and the scattering region (central region). Interactions between the electrodes (left \leftrightarrow right) is assumed to be zero, means there is no direct tunneling between the leads. After describing the Hamiltonian, in the next step, we will see the NEGF approach to solve the Schrödinger equation, where the retarded Green's function G corresponding to the Hamiltonian matrix H can be written as:

$$[ES - H]G = I, \quad (2.56)$$

where S is the overlap matrix, I stands for an identity matrix and G described as

$$G = \begin{pmatrix} G_L & G_{CL} & G_{RL} \\ G_{LC} & G_C & G_{RC} \\ G_{LR} & G_{CR} & G_R \end{pmatrix}. \quad (2.57)$$

It is easier to partition the whole system into different regions and calculate the Green's function as we are not interested in the process inside the electrode. Further, the central region is only connected to the surface of the electrode.

Hence, one can expect that the interaction term $\tau_{L(R)}$ would be much smaller in size than H . Thus, after solving the Eqs. (2.56) and (2.57) we get,

$$\begin{pmatrix} ES - H_L & -\tau_L & 0 \\ -\tau_L^\dagger & ES - H_C & -\tau_R^\dagger \\ 0 & -\tau_R & ES - H_R \end{pmatrix} \begin{pmatrix} G_L & G_{CL} & G_{RL} \\ G_{LC} & G_C & G_{RC} \\ G_{LR} & G_{CR} & G_R \end{pmatrix} = I. \quad (2.58)$$

Further, after solving the Eq. (2.58), the full Green's function described earlier in Eq. (2.57), becomes

$$G = \begin{pmatrix} g_L(1 + \tau_L G_{LC}) & g_L \tau_L G_C & g_L \tau_L G_{RC} \\ G_{LC} & G_C & G_{RC} \\ g_R \tau_R G_{LC} & g_R \tau_R G_C & g_R(1 + \tau_R G_{RC}) \end{pmatrix}, \quad (2.59)$$

where $g_{L/R} = (ES - H_{L/R})^{-1}$ is the surface Green's function of the left and right lead uncoupled to the central region.

The solution of above mentioned equations gives the final expression for retarded Green's function of the central region, which can be described as

$$G_C = [ES - H_C - \Sigma_L(E) - \Sigma_R(E)]^{-1}, \quad (2.60)$$

with $\Sigma_L(E) = \tau_L^\dagger g_L \tau_L$ and $\Sigma_R(E) = \tau_R^\dagger g_R \tau_R$ are the self energies. The self energy is associated to the energy level shift and the energy level broadening. The energy level shift and the energy level broadening can be defined from the real and imaginary part as

$$\Delta_{L/R}(E) = \text{Re} [\Sigma_{L/R}(E)], \quad (2.61)$$

$$\begin{aligned} \Gamma_{L/R}(E) &= i[\Sigma_{L/R}(E) - \Sigma_{L/R}^\dagger(E)] \\ &= -2\text{Im}[\Sigma_{L/R}(E)]. \end{aligned} \quad (2.62)$$

The broadening of the molecular orbital is associated with the life time of the electronic state on the molecule. An electron can escape from the lead when it is coupled with the molecule and can spend some time on the molecular state at the central region. This life time (\mathcal{J}) is inversely proportional to the broadening of the states such that $\mathcal{J}\Gamma = \hbar$.

Further, from Eq. (2.60), the infinite dimensional Hamiltonian is reduced to the dimension of the central region, which has much smaller dimension. The self energies $\Sigma_{L/R}$ includes all the information of the semi-infinite properties of the lead. The central part only interacts with the surface region of the electrode [132]. Thus, one can only focus on the Green's function matrix of the central region and effective Hamiltonian would be

$$H_{\text{eff}} = H_C + \Sigma_L(E) + \Sigma_R(E). \quad (2.63)$$

2.9.1 The Schrödinger equation

According to the definition (2.56) and because of self adjoint Hamiltonian, we can write retarded and advanced wave function for the inhomogeneous Schrödinger equation as,

$$|\psi\rangle^R = -G|\nu\rangle, \quad (2.64)$$

$$|\psi\rangle^A = -G^\dagger|\nu\rangle. \quad (2.65)$$

Further, we can write the Schrödinger equation as

$$(E - H)|\psi\rangle = -|\nu\rangle. \quad (2.66)$$

Here, the difference $|\psi\rangle^R - |\psi\rangle^A$ is the solution to the homogeneous Schrödinger equation. Thus, for any vector $|\nu\rangle$, the vector representing wave function can be obtained as

$$|\psi\rangle = A|\nu\rangle, \quad (2.67)$$

where A has the form

$$A = i(G - G^\dagger) = -2\text{Im}(G). \quad (2.68)$$

A is known as the spectral function, which solves the homogeneous Schrödinger equation and the Green's function can be expanded in the eigen basis as

$$G = \sum_k \frac{|\psi_k\rangle\langle\psi_k|}{E + i\eta - E_k}. \quad (2.69)$$

Now, substituting Eq. (2.69) back in Eq. (2.68)

$$\begin{aligned} A(E) &= i \sum_k |\psi_k\rangle\langle\psi_k| \left(\frac{1}{E + i\eta - E_k} - \frac{1}{E - i\eta - E_k} \right) \\ &= \sum_k |\psi_k\rangle\langle\psi_k| \frac{2\eta}{(E - E_k)^2 + \eta^2}. \end{aligned} \quad (2.70)$$

Let η be zero then it becomes ²

$$A(E) = 2\pi \sum_k \delta(E - E_k) |\psi_k\rangle\langle\psi_k|, \quad (2.71)$$

where $\delta(E - E_k)$ is a delta function. Further, using the spectral function from Eq. (2.68), we can write

$$A_C(E) = i(G_C - G_C^\dagger) = iG_C(G_C^{\dagger-1} - G_C^{-1})G_C^\dagger. \quad (2.72)$$

² Plemelj formula: $\lim_{\eta \rightarrow 0} \frac{1}{x \pm i\eta} = \mp i\pi\delta(x) + \text{Pr}\left(\frac{1}{x}\right)$, where Pr defines the Cauchy principal value.

Using Eq. (2.62), we can define identity as

$$\begin{aligned} A_C(E) &= iG_C(E - H_C - \Sigma_L^\dagger(E) - \Sigma_R^\dagger(E) - E + H_C + \Sigma_L^\dagger(E) + \Sigma_R^\dagger(E))G_C^\dagger \\ &= iG_C(\Gamma_L(E) + \Gamma_R(E))G_C^\dagger. \end{aligned} \quad (2.73)$$

It shows that the spectral function at central region is defined by the spectral functions of the left and right electrodes, which means that it is induced by the states at these electrodes through the coupling.

2.9.2 Transport problem and charge density

In this section, we will discuss the transport problem by taking the case of left to right transport problem. Using the standard screening problem, we can write

$$\begin{pmatrix} H_L & \tau_L & 0 \\ \tau_L^\dagger & H_C & \tau_R^\dagger \\ 0 & \tau_R & H_R \end{pmatrix} \begin{pmatrix} \psi_L \\ \psi_C \\ \psi_R \end{pmatrix} = E \begin{pmatrix} \psi_L \\ \psi_C \\ \psi_R \end{pmatrix} = E|\psi\rangle. \quad (2.74)$$

Now, we first consider an isolated left electrode, where an incoming wave gets totally reflected at the end of the contact. This will lead us to the interaction term at the left electrode, $\tau_L = 0$. If $|\nu\rangle$ is the solution wave function then,

$$\begin{pmatrix} H_L & 0 & 0 \\ 0 & H_C & \tau_R^\dagger \\ 0 & \tau_R & H_R \end{pmatrix} \begin{pmatrix} \nu \\ 0 \\ 0 \end{pmatrix} = E' \begin{pmatrix} \nu \\ 0 \\ 0 \end{pmatrix} = E'|\nu\rangle. \quad (2.75)$$

For the connected left electrode to the central region, one can get the wave-function of the whole system. We can start from the simple ansatz $|\psi\rangle + |\nu\rangle$

$$\begin{pmatrix} H_L & \tau_L & 0 \\ \tau_L^\dagger & H_C & \tau_R^\dagger \\ 0 & \tau_R & H_R \end{pmatrix} \begin{pmatrix} \psi_L + \nu \\ \psi_C \\ \psi_R \end{pmatrix} = E \begin{pmatrix} \psi_L + \nu \\ \psi_C \\ \psi_R \end{pmatrix}. \quad (2.76)$$

From Eqs. (2.74) and (2.75), we get

$$\begin{pmatrix} H_L & \tau_L & 0 \\ \tau_L^\dagger & H_C & \tau_R^\dagger \\ 0 & \tau_R & H_R \end{pmatrix} |\psi\rangle + \begin{pmatrix} 0 & \tau_L & 0 \\ \tau_L^\dagger & 0 & 0 \\ 0 & 0 & 0 \end{pmatrix} |\nu\rangle = E|\psi\rangle + (E - E')|\nu\rangle. \quad (2.77)$$

This yields Schrödinger equation as following

$$\begin{pmatrix} H_L & \tau_L & 0 \\ \tau_L^\dagger & H_C & \tau_R^\dagger \\ 0 & \tau_R & H_R \end{pmatrix} |\psi\rangle = E |\psi\rangle - \begin{pmatrix} E' - E & \tau_L & 0 \\ \tau_L^\dagger & 0 & 0 \\ 0 & 0 & 0 \end{pmatrix} |v\rangle. \quad (2.78)$$

Using Eqs. (2.59) and (2.78) and applying some algebra, we can write the wave function for left and right leads and center due to incoming wave as,

$$\begin{aligned} |\psi_L\rangle &= (g_L \tau_L G_C \tau_L^\dagger + 1) |v\rangle, \\ |\psi_C\rangle &= G_C \tau_L^\dagger |v\rangle, \\ |\psi_R\rangle &= g_R \tau_R G_C \tau_L^\dagger |v\rangle. \end{aligned} \quad (2.79)$$

Now, these equations have physical significance. Once we know the incoming solution for the electrode, we can get the total solution. After knowing the electron population in the contact regions, we can fill the different transport states of the system.

Further, we can calculate the charge density

$$\rho = e \sum_k f(E_k, \mu) |\psi_k\rangle \langle \psi_k|, \quad (2.80)$$

where f stands for occupation of the states at energy E and with chemical potential μ of the electrode. Now the charge density induced from left electrode would be,

$$\rho_L = e \sum_k f(E_k, \mu_L) G_C \tau_L^\dagger |v_k\rangle \langle v_k| \tau_L G_C^\dagger. \quad (2.81)$$

Using the definition of delta function, we get

$$\rho_L = e \int dE \sum_k f(E, \mu_L) G_C \tau_L^\dagger |v_k\rangle \delta(E - E_k) \langle v_k| \tau_L G_C^\dagger. \quad (2.82)$$

In Eq. (2.82), we can identify spectral functional from Eq. (2.71) for the left contact as

$$a_L = 2\pi \sum_k |v_k\rangle \delta(E - E_k) \langle v_k|. \quad (2.83)$$

Further, using identity from Eq. (2.73), we can write

$$\tau_L^\dagger a_L \tau_L = i \tau_L^\dagger (g_L - g_L^\dagger) \tau_L = i (\Sigma_L - \Sigma_L^\dagger) = \Gamma_L. \quad (2.84)$$

Using Eqs. (2.83) and (2.84) in Eq. (2.82), one can write the charge density as

$$\rho_L = \frac{e}{2\pi} \int dE f(E, \mu_L) G_C \Gamma_L G_C^\dagger. \quad (2.85)$$

Finally, the full charge density would be sum over the contacts

$$\rho_L = \frac{e}{2\pi} \int dE \sum_{i=L,R} f(E, \mu_i) G_C \Gamma_i G_C^\dagger. \quad (2.86)$$

2.9.3 Calculation of current

The flow of current in the system occurs because of the imbalance of the electron population in the leads, e.g., because of different chemical potentials. Let us assume from left to right in Fig. 2.3, electrons are getting transferred from left to right reservoir. To deal with computational issues, we assume that the process of refilling the reservoir is taking place continuously and it is far away from the central region which makes the system stationary. Thus, all the transitional oscillations must have died out because of weak inelastic processes. Hence, we assume that the probability of current in system does not change overtime (steady state), hence the probability of finding an electron on the device is conserved as

$$\frac{\partial \langle \psi_C | \psi_C \rangle}{\partial t} = \frac{\partial \langle \psi_C |}{\partial t} \langle \psi_C | + | \psi_C \rangle \frac{\partial \langle \psi_C |}{\partial t} = 0. \quad (2.87)$$

Physically, it is equivalent to the case when the electrodes are not getting refilled with the electrons. Instead these electrodes are assumed to be enormously big, enough to ensure the continuous flow of electrons from one electrode to another. Actually, this happens during the experiments. Now the time dependent Schrödinger equation is defined as,

$$\frac{\partial |\psi\rangle}{\partial t} = -\frac{i}{\hbar} H |\psi\rangle. \quad (2.88)$$

By combining Eqs. (2.74) and (2.88), we get

$$\frac{\partial |\psi_C\rangle}{\partial t} = \frac{i}{\hbar} (\tau_L^\dagger |\psi_L\rangle + H_C |\psi_C\rangle + \tau_R^\dagger |\psi_R\rangle). \quad (2.89)$$

Inserting Eq. (2.89) into (2.87), it becomes

$$-\frac{i}{\hbar} \left[\left(-\langle \psi_L | \tau_L | \psi_C \rangle + \langle \psi_C | \tau_L^\dagger | \psi_L \rangle \right) + \left(\langle \psi_C | \tau_L^\dagger | \psi_R \rangle - \langle \psi_R | \tau_L | \psi_C \rangle \right) \right] = 0. \quad (2.90)$$

In the equation above, the first and second term represent the incoming probability of current from left contact L and from right contact R , respectively. Now, we can interpret the electric current from an arbitrary contact j into the central part as the charge times the probability current

$$I_j = \frac{ie}{\hbar} [\langle \psi_C | \tau_j | \psi_j \rangle - \langle \psi_j | \tau_j^\dagger | \psi_C \rangle], \quad (2.91)$$

where j stands for L or R , I_j as a electric current from the j^{th} contact to the central region.

Further, to calculate the current one needs to insert the wave function of the contacts ψ_j and the central part ψ_C from Eq. (2.79) in the Eq. (2.91). Thus we

get the current through the central region due to the incoming wave as,

$$\begin{aligned}
I_{V \rightarrow R} &= \frac{ie}{\hbar} [\langle v | \tau_L G_C^\dagger \tau_R^\dagger g_R \tau_R G_C \tau_L^\dagger | v \rangle - \langle v | \tau_L G_C^\dagger \tau_R^\dagger g_R^\dagger \tau_R G_C \tau_L^\dagger | v \rangle] \\
&= \frac{ie}{\hbar} [\langle v | \tau_L G_C^\dagger \tau_R^\dagger (g_R - g_R^\dagger) \tau_R G_C \tau_L^\dagger | v \rangle] \\
&= \frac{e}{\hbar} [\langle v | \tau_L G_C^\dagger \Gamma_R G_C \tau_L^\dagger | v \rangle].
\end{aligned} \tag{2.92}$$

We can obtain the total current through the device by summing over the incoming states $|v\rangle$ (at the energy E) and integrating over the energy. Hence the total current in the device would be:

$$\begin{aligned}
I_{L \rightarrow R} &= \frac{2e}{\hbar} \int_{-\infty}^{\infty} dE \sum_v \text{DOS}(E) \langle v | \tau_L G_C^\dagger \Gamma_R G_C \tau_L^\dagger | v \rangle \\
&= \frac{2e}{\hbar} \int_{-\infty}^{\infty} dE \sum_{m,v} \text{DOS}(E) \langle v | \tau_L | m \rangle \langle m | G_C^\dagger \Gamma_R G_C \tau_L^\dagger | v \rangle \\
&= \frac{2e}{\hbar} \int_{-\infty}^{\infty} dE \sum_m \langle m | G_C^\dagger \Gamma_R G_C \tau_L^\dagger \sum_v \text{DOS}(E) | v \rangle \langle v | \tau_L | m \rangle \\
&= \frac{2e}{\hbar} \int_{-\infty}^{\infty} dE \sum_m \langle m | G_C^\dagger \Gamma_R G_C \tau_L^\dagger \frac{A_L}{2\pi} \tau_L | m \rangle \\
&= \frac{2e}{\hbar} \int_{-\infty}^{\infty} dE \text{Tr}(G_C^\dagger \Gamma_R G_C \Gamma_L).
\end{aligned} \tag{2.93}$$

Here, the factor 2 is included for spin. If the electrodes are connected to the reservoirs with the electron gas at the chemical potential μ_L , then the states in the electrodes are filled according to the Fermi distribution function $f(\mu, E)$. Thus the total current between the two electrodes would be

$$I_{L \rightarrow R} = \frac{e}{\hbar} \int_{-\infty}^{\infty} dE \text{Tr}(G_C^\dagger \Gamma_R G_C \Gamma_L) [f(E - \mu_L) - f(E - \mu_R)]. \tag{2.94}$$

Eq. (2.94) is the famous Landauer formula for transport with the transmission function as,

$$T(E) = \text{Tr}(G_C^\dagger \Gamma_R G_C \Gamma_L). \tag{2.95}$$

At the equilibrium condition, when both the electrodes have same chemical potential and temperature, there will be no current because the current from left to right would be exactly equal to the current from right to left.

Part II:
Summary of the Results

3. Nanoscale device applications of 2D materials

In the modern world, electronic devices are associated with many aspects of our day to day lives, and these devices are getting smaller and smaller with time. Silicon has been the primary material for electronic device applications for decades. However, silicon-based devices are reaching to their lowest scaling limit and probably may not be longer sustain with the famous Moore's law, which suggests that the number of transistors on a chip will double every two years [38]. The successful isolation of graphene in 2004 [8] paved the way to go beyond the silicon-based technology, and one can look in the quantum device regime. The astonishing progress in nanotechnology has rendered the experimental realization of graphene electrodes using electro burnt method and mechanical break junction has been employed in several state of the art molecular and nanoelectronic applications [56–58]. In similar fashion, graphene nanopores and nanogaps are compelling examples of application in DNA (deoxyribonucleic acids) sequencing and salt water filtering, etc. [59–62]. Graphene has its advantages and limitations as a material for nanoscale electronic applications [133, 134], which pushed the scientific community to look beyond, and a big family of 2D materials emerged with time with a variety of electronic, optical and transport properties. Monolayer of black phosphorus (BP) also known as phosphorene is relatively new but very exciting material for the semiconductor industry for its application in FET, photodetector and several other applications owing to its high mobility and on-off ratios [13, 20]. In this chapter, we will discuss two different application of these materials in lateral and vertical heterostructure form with theoretical approach. In the first part, graphene-hexagonal boron nitride (G/hBN) lateral heterostructure nanogap is discussed with the potential application in identification of the DNA building blocks, nucleobases. In the second section, we have discussed electronic and structural properties of BP in symmetric and twisted bilayer form and further the transport behavior in the nanojunction device architecture is discussed. It is proposed for the current rectifying application.

3.1 DNA sequencing in Graphene/h-BN nanogap

DNA carries the full genetic information of all the living organisms. DNA sequencing is a process of determining the order of nucleotides in DNA. It is

like reading the genetic code, which can be called as “*alphabet of life*”, A, T, G, and C (adenine, thymine, guanine, and cytosine) nucleobase sequence. Single-stranded DNA, have its bases ~ 0.34 nm apart. These strands can be dragged through the graphene nanogap/nanopores and they can be matched with a width of graphene electrode, which makes graphene based pore efficient in comparison with traditional gold nanopore or nanogap. Graphene nanogap has been reported computationally, where the nanogap formed with an armchair edge of graphene could serve as a functioning device to sequence DNA [59–61]. However, the practical implementation of graphene nanochannels meets the challenges because of high reactivity at the edges [63–65]. In this work, the idea of having atomic layer 2D material nanochannel is mixed with recent advancement, where 2D heterostructures are the new trend to modify the materials property [78]. The graphene edges are terminated with hBN strips to lower down the reactivity at the edges. The comparison of edge reactivity with nucleobases suggests that the hBN edge is less reactive with respect to the graphene edge. This gives rise to the idea that such a heterostructure may be a suitable nanochannel device for DNA sequencing. In which dAMP, dTMP, dGMP, and dCMP (deoxy adenosine monophosphate, deoxy thymidine monophosphate, deoxy guanine monophosphate, and deoxy cytosine monophosphate, respectively) are the target nucleotides.

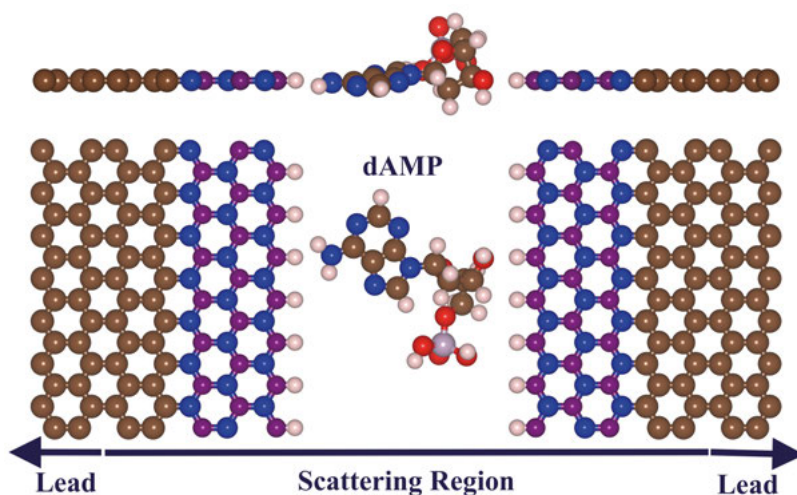


Figure 3.1. Schematic of the nanogap setup for the nucleotides (shown for dAMP case), illustrating the semi infinite leads and scattering regions. [Atom color code: C (green), N (blue), B (purple), O (red), P (light purple), H (white)]. Reproduced with permission from Paper I. Copyright ©2016 American Chemical Society.

The target nucleotides are placed in the nanogap, which is maintained at 12.6 Å. Fig. 3.1 shows the schematic illustration of the nanogap having a nucleotide in between. In the setup, graphene serves as the electrodes and hBN

terminated with H forms the nanogap by directly interacting with the incoming nucleobases. When nucleobases pass through the nanogap setup, it bridges

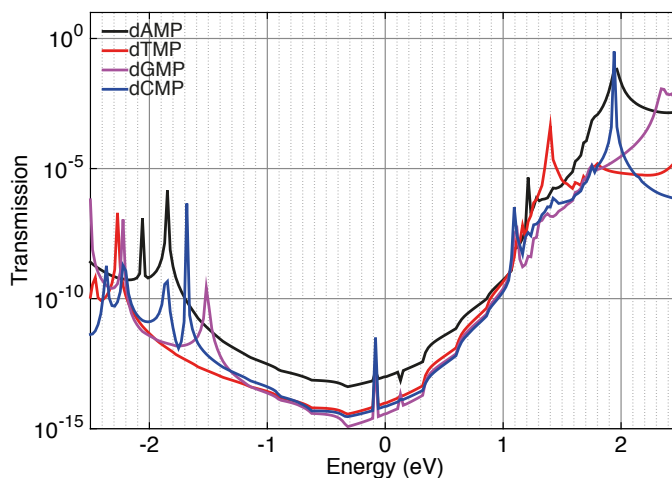


Figure 3.2. Zero-bias transmission function of the four target nucleotides (dAMP, dTMP, dGMP, dCMP). Reproduced with permission from Paper I. Copyright ©2016 American Chemical Society.

the nanogap, and the characteristics tunneling current can be measured which forms the basis of recognition of the bases. In Fig. 3.2, zero bias transmission shows a clear distinction among the nucleotides. Highest occupied molecular orbital (HOMO) associated peaks appear between the energies of -1 and -2.2 eV, whereas lowest unoccupied molecular orbital (LUMO) ones are mainly situated in between the range of 1 to 2 eV as can be seen in Fig. 3.2. The projected density of states has confirmed these HOMO and LUMO position of nucleotides in the gap [135]. Further, these HOMO and LUMO positions vary upon shifting and rotating of the target nucleotides in between the gap and this variation in HOMO and LUMO positions happen due to the change in chemical interactions between the nucleotides and hydrogenated hBN edge [135]. The calculated current-voltage (I-V) characteristics is shown in Fig. 3.3(a), which suggests that these nucleotides can be distinguished at the two different voltage ranges in lower and higher bias regimes. For instance, one can see almost two orders of magnitude higher current for dTMP than dCMP at 3.2 V, which divulged the better sensitivity towards them. On the other hand, the current trace for dAMP is smaller than that for dTMP, and at ~ 2.9 V, one can observe a notable difference between these two bases. Therefore, at this voltage, a clear classification of these two bases seems reasonable. Additionally, scanning at the higher bias region, we find that current curves for dGMP and dCMP, although they mostly run parallel to each other, tend to split at ~ 2.9 V, which makes it feasible to identify these bases distinctly. We, accordingly, put forward that the voltage window of 2.7-3 V will be optimal for

a clearer distinction of all four nucleotides. In an attempt to demonstrate the sensitivity of detection of the four target nucleotides at the higher bias regime, the current responses of individual bases for a bias voltage between 2.8 and 2.9 V are presented in Fig. 3.3(b). This figure basically compiles the read-outs of current traces of all four bases within a given bias window (2.8-2.9 V). It is very clear from this figure that all four bases impart unique current signatures at the given bias window. More accurately, dTMP yields highest current while dCMP evinces lowest current, whereas dAMP and dGMP can be distinguished between the former two nucleobases. However, the low bias regime

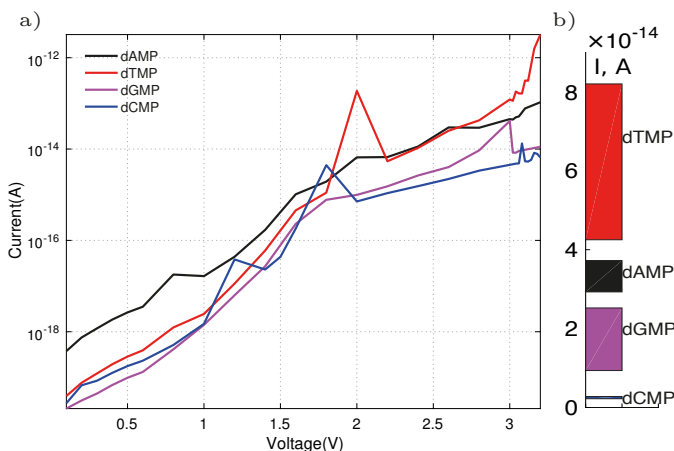


Figure 3.3. (a) Current-voltage characteristics of the four target nucleotides (dAMP, dTMP, dGMP, dCMP). The current axis is shown on a logarithmic scale. (b) The current responses (read-outs of current traces) for four target nucleotides within the bias range 2.8-2.9 V. Reproduced with permission from Paper I. Copyright ©2016 American Chemical Society.

of the I-V plot shows that the distinction between all four bases is also possible. From Fig. 3.3(a), it is conspicuous that dAMP delivers higher current as compared to the remaining bases up to 1 V, and it can be distinguished from dTMP. Moreover, for the characterization of other bases, we need to extend the voltage range up to 1.2 V, and all of the four target bases record different current traces at this voltage window. Consequently, keeping both lower and higher bias regimes in perspective, it is possible to detect all four bases uniquely at two voltage regimes but we observe better sensitivity at a higher bias window. Although, the I-V characteristics in this device exhibit relatively low current and the small tunneling current remains a problem indeed for any devices which measure the transverse current in DNA sequencing. Nevertheless, it must be possible to address this issue in well-tuned experiments. In brief, this study establishes the utilization of nanogap setup in the form of a lateral heterostructure of graphene with passivated hBN for DNA sequencing.

See Paper I for a detailed discussion about the translocation and rotation of nucleotides between the nanogap.

3.2 Twisted bilayer black phosphorus nanojunction

Synthesis of new materials by stacking monolayers of same or two different materials, i.e., the epitaxial growth of superlattices has been a subject of intense research for decades [136]. The idea of van der Waals (vdW) heterostructures was conceptualized by A. Geim and I. Grigorieva a few years back [69]. These vdW heterostructures are materialized by stacking of two 2D crystalline atomic layers, with no chemical bond between them [70, 71]. These stacking patterns unfold the world of the possibility of many desired heterostructure with the specified chemical/physical and electronic properties. These heterostructures have been studied widely both theoretically and experimentally, like G/hBN, MoS₂/G, MoS₂/WSe₂ for band alignment and charge transfer, which make them suitable for optoelectronic applications [72–74]. WSe₂/hBN/G heterostructure was reported for programmable p-n junction diodes [137], and the same property has also been recited for transition metal dichalcogenides (TMD)/G, h-BN/TMD, and TMD/TMD, and several others [75–77]. In this section, the possibility of using vdW heterostructures

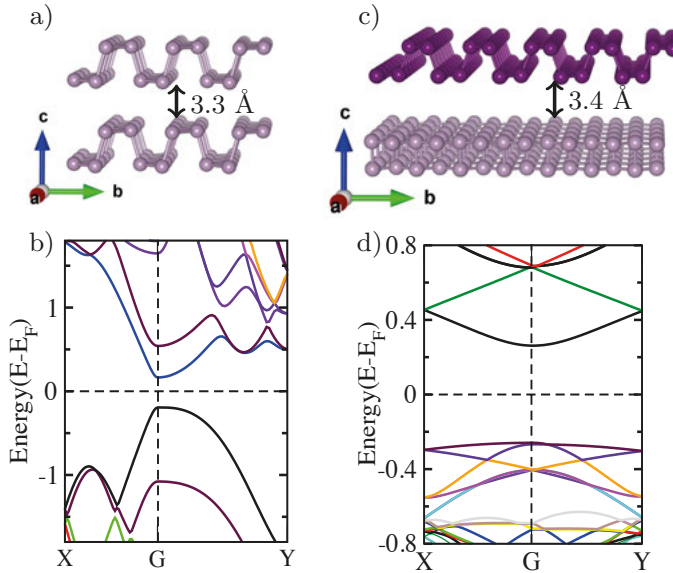


Figure 3.4. (a) Illustration of AA-stacked bilayer black phosphorus (BP) (c) 90° twisted stacked bilayer structure (Upper layer is twisted by 90° with respect to the lower layer), band structures of (b) bilayer (d) twisted bilayer (Brillouin zone for the twisted bilayer is a square).

of stacked 2D bilayer black phosphorus (BP) for nanoscale device applica-

tion is explored. The symmetric and twisted bilayer structures are shown in Fig. 3.4(a,c). The symmetric bilayer is considered in AA stacked form and the second one is in 90° twisted form, where the top layer is rotated by 90° with respect to the bottom layer. The band structure in Fig. 3.4(b) shows the anisotropic properties of the bilayer form in zigzag and armchair direction and the bandgap is reduced to 0.39 eV as compared to 0.9 eV of the monolayer BP [21]. Strong interlayer interaction due to two extra lone pair electrons of the P atom is responsible for this reduction in the bandgap. Let us shift our attention towards twisted bilayer, in Fig. 3.4(c), which is laterally symmetric in structure. Supercell approach is used to reduce the lattice mismatch to 1% in 5×7 times that of the unit cell. Twisted bilayer has square reciprocal lattice geometry in the Brillouin zone, and the symmetric band structure is shown in Fig. 3.4(d). Twisted bilayer yields a band gap of 0.48 eV, which is bigger than that of the AA-stacked bilayer. This increment in band gap happens due to the lower interlayer interaction in between the layers. The conduction band minimum (CBM) is singly degenerate, while the valence band maximum (VBM) is doubly degenerate with the value of 0.01 eV. This degeneracy advocates the lack of significant hybridization near the VBM, whereas the CBM are strongly coupled. The degenerate states in VBM are localized either in the top layer or the bottom layer. This degeneracy paves the way for symmetric electronic structure, where X-G is defined by the top layer and G-Y is described by the bottom layer. This degeneracy and symmetric nature are highly dependent on vertical electric field and strain [138, 139].

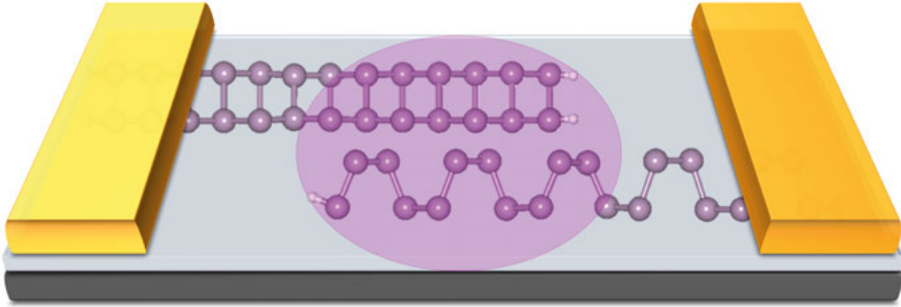


Figure 3.5. Schematics of twisted bilayer nanojunction device. The device region is composed of bilayer in the armchair, and zigzag direction and the left and right electrodes are consisting of the monolayer of zigzag and armchair direction of BP.

Further, the twisted bilayer nanojunction is described in Fig. 3.5. The ML-BL-ML (monolayer-bilayer-monolayer) architecture has one of the monolayers in the armchair direction and the other one in zigzag direction. The central region shows a structure of a vertically stacked 90° twisted bilayer, which is isotropic unless now the twisted nanojunction setup is attached with the semi-infinite electrodes in either direction. The upper layer defines the zigzag trans-

port direction, and the lower layer exhibits armchair transport direction, and both layers have one edge terminated with hydrogen, which makes the system asymmetric in either directions. In this case, the junction length is 12 Å in the transport direction, and the width is periodic. The current rectifying property in I-V curve can be seen in Fig. 3.6. In the negative bias regime, when the

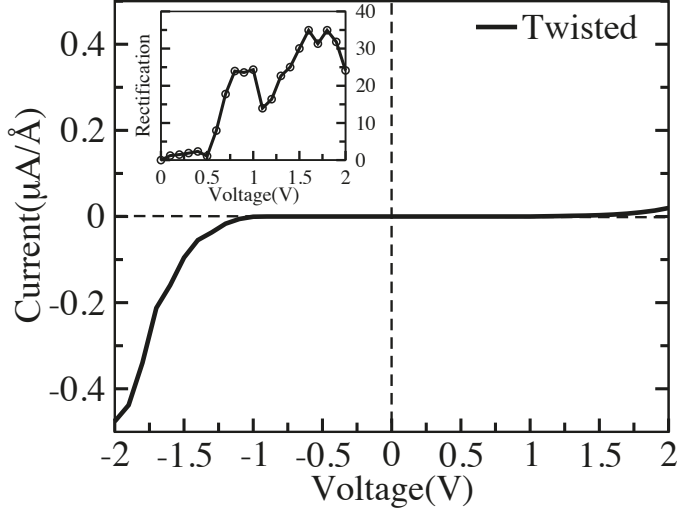


Figure 3.6. Current-Voltage (I-V) characteristics for twisted nanojunction device (the rectification ratio (I_-/I_+) of the respective device is shown in the inset).

electrons are injected from armchair to zigzag direction, yields higher current. On the other hand, in positive bias, the current flows from zigzag direction to armchair direction yielding lower current. The inset of Fig. 3.6, describes the rectification ratio (I_-/I_+) with maximum of 35 achieved at ± 1.8 V bias.

The rectifying behavior in the described nanojunction is further explained with the help of transmission function plot at ± 1.8 V bias, as shown in Fig. 3.7(a). In the negative bias regime, relatively higher transmission probability is noticed at 0 eV, but the dominant peak comes at 0.35 eV, whereas a much lesser transmission for positive bias (+1.8 V) can be seen in the bias window. For more detailed understanding of these difference in transmission function, corresponding eigenchannels are plotted for both the biases at ± 1.8 V at 0 eV energy, which can be seen in Fig. 3.7(b,c). In the negative bias as shown in Fig. 3.7(c), there is a tunneling probability from armchair to zigzag layer as the channel is spread all over the device region. This advocates the higher current in negative bias as shown in Fig. 3.6. Furthermore, lower conductance in positive bias (+1.8 V) can be explained from Fig. 3.7(b), where more localized eigenchannels towards the left side of the nanojunction are seen, which remains only in the zigzag layer. This describes the lower tunneling from the zigzag to armchair layer. As already discussed in Fig. 3.7(a) that in the negative bias, higher transmission peak comes at +0.35 eV, henceforth

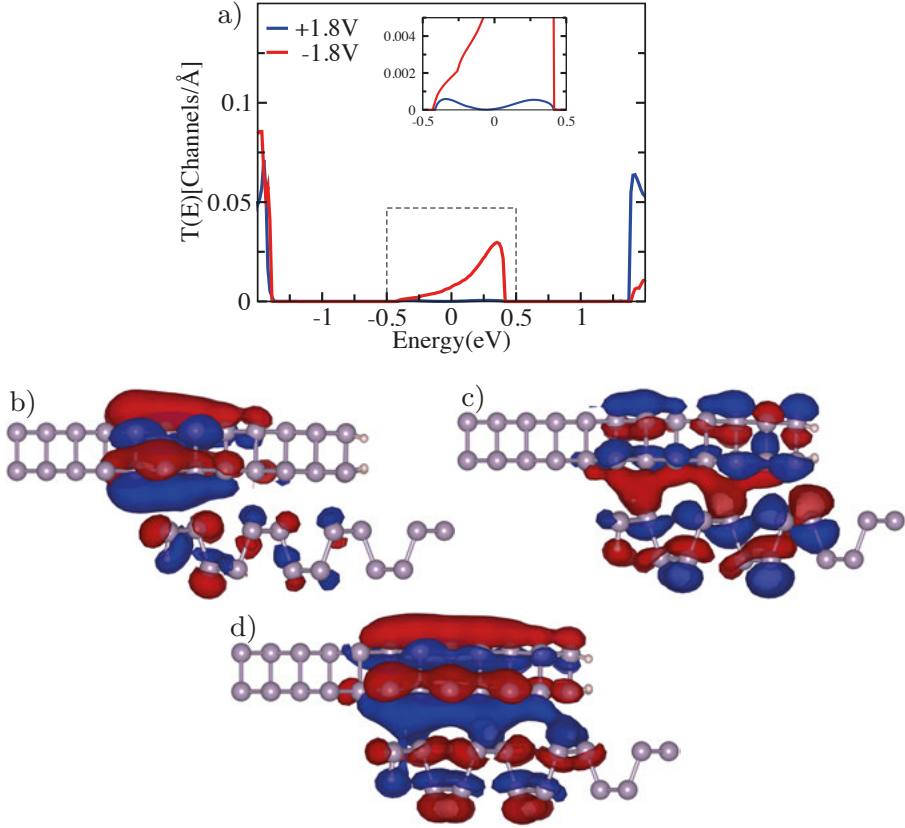


Figure 3.7. (a) Transmission function at ± 1.8 V biases for nanojunction (inset zooms the picture of transmission around 0 eV) and eigenchannels for twisted bilayer nanojunction at 0 eV (b) positive bias of 1.8 V (c) negative bias of 1.8 V and (d) eigenchannel at 0.35 eV for negative 1.8 V bias.

the eigenchannels at this energy are shown in Fig. 3.7(d). This evidences a strong tunneling channel, delocalized all over the nanojunction area, which is responsible for much higher current in the negative bias regime.

Rectifying behavior in a device with no electron transfer between the layers and no band bending is very interesting. In the positive bias when the current flow is from the zigzag to armchair direction, the current limiting regime is zigzag directional current. Whereas in the opposite direction, when the current flow is from the armchair to zigzag direction, it follows the armchair direction for limiting current. The detailed description of the current-voltage characteristics in the symmetric armchair and zigzag nanojunction can be found in paper II. We found the symmetric current in positive and negative bias regime for both the symmetric nanojunctions, which strongly suggests that the rectification that occurs in the twisted nanojunction device is only due to the intrinsic anisotropic behavior of the BP. Furthermore, the gate tunable elec-

tronic structure of the twisted bilayer presents the possibility to regulate the electron transport in the real-time device, where the transport behavior can be controlled by the applied gate voltage. This can even yield much higher rectification, which makes the setup useful in nano-electronic applications. Further details can be found in paper II.

4. Electronic and transport properties of 2D materials

During the last decade, the research on 2D material beyond graphene with varying electronic characteristics such as metal, insulator, and semiconductor has been actively pursued to make the dream of the atomically thin device a reality. There are some established 2D materials like transition metal dichalcogenides (TMDs) and hexagonal boron nitride (hBN), and these have already been favorably explored in the nanoscale device applications [140, 141]. Usually, 2D materials exhibit the outstanding commitment for the futuristic electronic device applications due to their exceptional carrier mobility in a single layer, strong mechanical nature, abundant active sites and a large surface to volume ratios. This crusade has triggered new areas of research with rapid growth from both experimental and theoretical aspects aimed at technological advancements. With the progress in this area, many synthetic 2D materials have been realized such as germanene, stanene, bismuthene, and tellurene, etc. [23–26]. Although the study of these materials is yet at an early stage, the computational predictions and commencing measurements of their properties underpin that they are reciprocal to the conventional 2D materials (layered, derived from bulk).

In the quest of new materials in 2D family, boron, the fifth element in the periodic table has recently been realized experimentally in the different form of structures [27, 28]. Earlier, It was theoretically reported that the single layer of boron exhibits rich polymorphism with multiple low energy structures because it has one less valence electron than the available valence orbital [142–144]. The multicenter bonds and electron deficient features of boron make the synthesis of 2D boron a challenging problem [145, 146]. Experimental evidence for the first synthesis of 2D boron known as borophene was reported by Mannix *et al.* [27] in 2015 and nearly at the same time Feng *et al.* [28] reported two different polymorphs of 2D boron known as β_{12} and χ borophene. In both the cases, synthesis was performed under ultra-high vacuum conditions, and clean Ag(111) surface was used as the substrate. Theoretical prediction suggested that boron 2D sheets are metallic while the bulk boron polymorph are semiconducting in nature [147, 148]. Apart from the synthetic 2D boron, 2D black phosphorus (BP), a material which belongs to the class of traditional 2D material attracted significant attention because of its high mobility, anisotropic electronic and transport properties and perfect semiconducting nature [13]. BP has already been explored for several applications [149–151]. Rectifying

behavior of twisted bilayer nanojunction has been already discussed in the previous chapter.

In this chapter, structural, electronic and transport properties of the newly synthesized 2D boron polymorph known as β_{12} borophene, χ borophene, and corrugated borophene will be discussed. We will further discuss the gas sensing possibilities in corrugated borophene. In the later section, the case of silicon and sulfur substituted BP monolayer and its application in gas sensing with the use of density functional theory and NEGF is briefly discussed.

4.1 β_{12} and χ -borophene

The experimentally observed 2D boron was found to consist of triangular boron grid and hexagonal holes, corresponding to a β_{12} -borophene sheet and a χ -borophene sheet as described earlier by theoretical calculations [28]. β_{12} -borophene has 5 atoms in the unit cell with $p2mm$ symmetry and relaxed lattice parameters are $a = 2.92 \text{ \AA}$, $b = 5.09 \text{ \AA}$ which can be seen in Fig. 4.1(a).

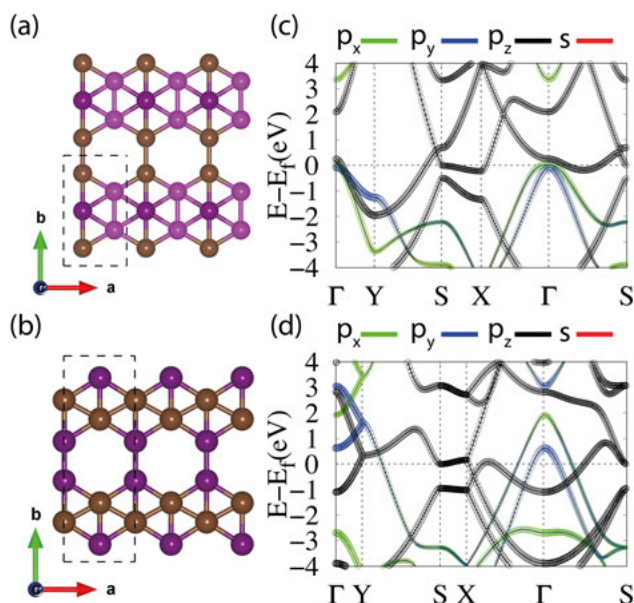


Figure 4.1. Structures of (a) β_{12} -borophene and (b) χ -borophene (dashed lines stand for the unit cells) and the respective band structures of (c) β_{12} -borophene (d) χ -borophene (orbital projection of bands are defined with colors above the graph). This figure is reproduced with permission from paper III. Copyright ©2018 Royal Society of Chemistry.

The band structure of β_{12} -borophene is shown in Fig. 4.1(c), where the metallic nature is visible. The bands near the Fermi level are mostly derived from the p_z orbital of boron atoms with some contribution from boron p_y orbitals. The structure of β_{12} has inhomogeneity as there are four-coordinated (brown), five-coordinated (magenta) and six-coordinated (purple) atoms in the unit cell. The structure has a linear, alternate atomic chain of the boron atom in y -direction which gives rise the metallic band along Γ -Y, S-X and Γ -S, whereas the x -direction is composed of the alternate filled hexagonal pattern. One can see the metallic band along Γ -X and Y-S, which are mainly composed of p orbitals of boron. This structure has inversion symmetry, where the massless Dirac fermions are expected. These Dirac cones are seen above the Fermi level at the energies 2 eV and 0.5 eV.

Further, the structure of χ -borophene can be seen in the Fig. 4.1(b), where the unit cell is composed of 8 atoms and two kinds of coordination of boron atom as 5-coordinated (purple) and 4-coordinated (brown) are shown. The unit cell has lattice parameter $a = 2.94 \text{ \AA}$, $b = 8.50 \text{ \AA}$, and shows higher inhomogeneity than β_{12} -borophene. It is characterized by alternate chains of hollow sites shifted by half of the lattice in the y -direction and chains of hollow sites separated by zigzag boron rows in the x -direction, resulting in planar $c2mm$ symmetry. The band structure in Fig. 4.1(d) depicts the metallic nature of χ -borophene and further shows anisotropic nature because of the gap in X-S direction. Same as the previous one, this structure also possesses the inversion symmetry and results a Dirac cone which is located below the Fermi level at 0.4 eV. These Dirac cones can be shifted at the Fermi level through strain or interaction with the substrate, which can compensate the electron deficiency. These polymorph are not stable in isolated form and one would need a substrate other than silver (metallic) to use these outstanding materials for futuristic device applications. This motivates us further to understand the effect of strain in these two polymorph. The detailed analysis of unidirectional strain on the electronic structure can be found in paper III.

4.1.1 Electron transport properties

A closer inspection of the intrinsic electron transport properties helps to understand the suitability of the material for electronic device applications. Therefore, to further explore anisotropy in the transport behavior, the direction-dependent zero bias transmission function for these borophenes are presented in Fig. 4.2. β_{12} -borophene does not exhibit anisotropy in transmission because x -direction has higher transmission above the Fermi level, and y -direction has higher transmission below the Fermi level in Fig. 4.2(a). At the Fermi level, both of them present a nearly equivalent transmission which lasts for isotropic nature of electron transport. This can be demonstrated from the band structure in Fig. 4.1(c), where Γ -Y has a gap, and X- Γ has bands above the Fermi level

that leads to higher transmission in $T_x(E)$. Below the Fermi level, Γ -Y has the higher number of bands than X - Γ , therefore, the $T_y(E)$ shows higher transmission. Overall transmission function does not show any anisotropy from -1 eV to 1 eV. Following the case of χ -borophene, the anisotropic behavior is seen in Fig. 4.2(b). The anisotropy is higher when there are alternate hollow sites in the y -direction. Transmission in x -direction $T_x(E)$ has the value of 1.2 Channels/ \AA and the y -direction $T_y(E)$ is 0.8 Channels/ \AA at the Fermi level. It can also be seen that $T_x(E)$ has higher value beyond the Fermi level. This can be justified from the band structure in Fig. 4.1(d). We can see that Γ -Y and X -S have only p_z contribution around the Fermi level, whereas X - Γ and Y -S have contributions from all the p orbitals. In the inset of the Fig. 4.2(a),

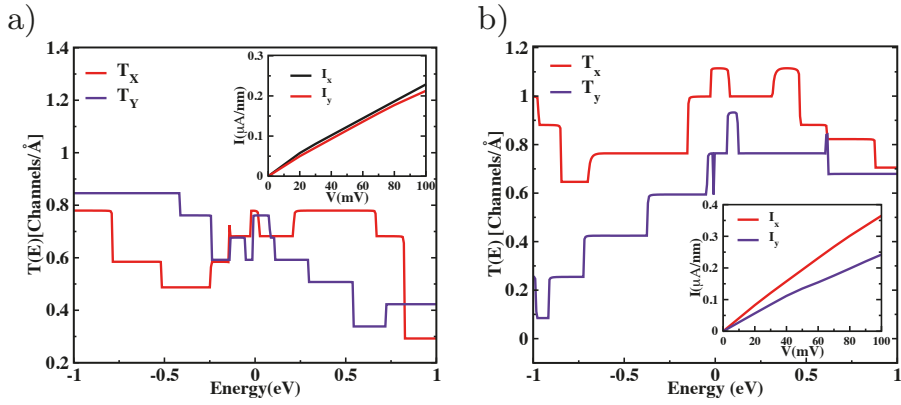


Figure 4.2. Zero bias transmission function along the x and y -direction as $T_x(E)$ and $T_y(E)$ in (a) β_{12} -borophene (b) χ -borophene, insets stand for the current-voltage characteristics in x -direction as I_x and y -direction as I_y . This figure is reproduced with permission from paper III. Copyright ©2018 Royal Society of Chemistry.

the current-voltage (I - V) characteristic is presented for β_{12} -borophene, which shows the same current in x and y -directions. On the other hand, in the case of χ -borophene, the anisotropic current can be seen in x and y -direction in the inset of Fig. 4.2(b). Further, this anisotropy (I_x/I_y) is calculated as 1.5 at 100 mV. It is clear from this discussion that the structures belonging to the same family show the different anisotropy in the current despite the fact that both of the structures have hollow sites in the form of hexagons. It is particularly the structural synergy which furnishes the anisotropy. Additionally, the anisotropy in these two systems can be tuned with the unidirectional strain in the system. β_{12} -borophene shows the strain tunable anisotropy, and it happens because of linear atomic chains in this structure, whereas χ -borophene rests nearly unchanged against the 6% of unidirectional strain. The detailed analysis of the strain tunable anisotropy can be found in paper III.

4.2 Corrugated borophene

The first experimentally realized member of the 2D boron family is corrugated borophene (we will call it borophene). This was synthesized on the silver substrate under high vacuum condition by Mannix *et al.* [27]. Soon after realization, it dragged attention and has been investigated for possible applications like Li and Na ion battery anode, hydrogen storage, and photo catalysis [152–156]. Additionally, a theoretical investigation has been performed to hydrogenate this borophene, which resulted in the graphene-like Dirac cone [157, 158]. Fig. 4.3(a) depicts the structure of the borophene, where it clearly shows the corrugation in y -direction and linear atomic chains of boron in x -direction. The band structure in Fig. 4.3(b) shows the highly anisotropic behavior of this borophene in two directions. It is clear from the band structure that there is no metallic band in Y-G and S-X direction, which is perpendicular to linear atomic chain of boron. One can see the metallic band in X-G direction, which presents linear chains ruled by the formation of σ B- p_x bonds. The elaborated discussion about the strain tunable anisotropy has been given by the Padhila *et al.* [158], where applied unidirectional strain tuned the anisotropy of borophene along with the hydrogenated borophene (borophane). There are

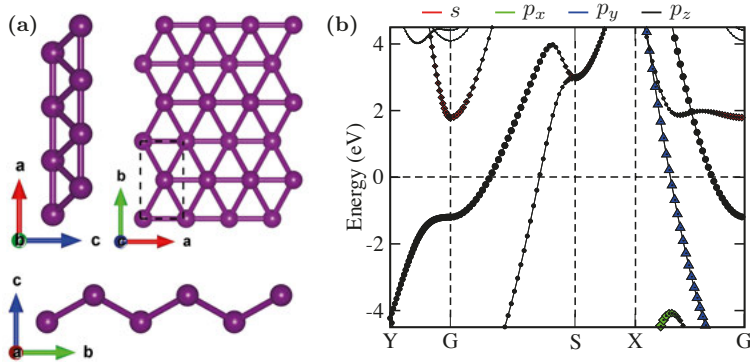


Figure 4.3. (a) Top and side views of optimized structures of the borophene (dashed lines stand for the unit cell) (b) orbital projected band structure of borophene.

several promising frontiers where borophene can find application, one such area is gas adsorption and detection. In an attempt to understand the feasibilities of gas sensing, it is essential to understand the interaction between the gas molecules and the borophene surface. Table 4.1 presents the adsorption energies of the gas molecules on the top of the surface along with distance and charge transfers.

The values represented in Table 4.1 stand for the most suitable (highest adsorption energies) cases. Borophene confers high adsorption strength towards the nitrogen-containing gases, whereas for carbon-based gases the adsorption energies are also moderate in comparison with most of the already explored 2D materials [159–162]. Particularly, in CO_2 case, the low adsorption energy

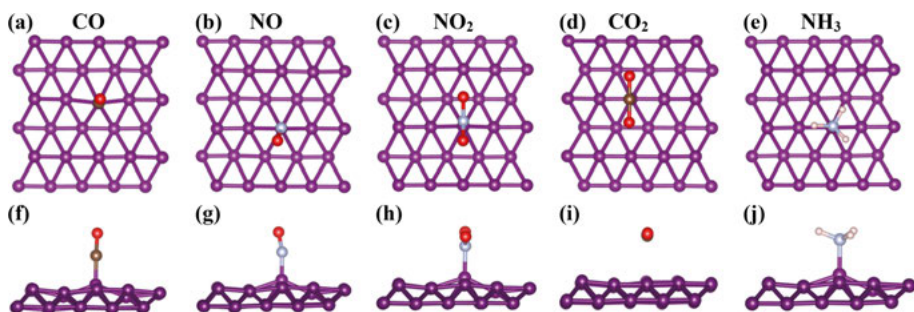


Figure 4.4. Top (a-e) and side (f-j) views of optimized structures of the borophene sheet with adsorbed gases CO, NO, NO₂, CO₂, and NH₃, respectively. Color code as B-purple, gray-N, red-O, cyan-H and brown-C. Reproduced with permission from Paper IV. Copyright ©2017 American Chemical Society.

Table 4.1. Calculated binding energies (E_b), net (Bader) charges on the gas molecules for different Gas+Borophene systems (ΔQ), and bonding distance (d_a). Reproduced with permission from Paper IV. Copyright ©2017 American Chemical Society.

Device	Gas	E_b (eV)	ΔQ (ρ)	d_a (Å)
Borophene	CO	-1.38	-0.39	1.49
	CO ₂	-0.36	-0.09	1.82
	NH ₃	-1.75	+0.18	1.63
	NO	-1.79	-0.62	1.44
	NO ₂	-2.32	-0.72	1.51

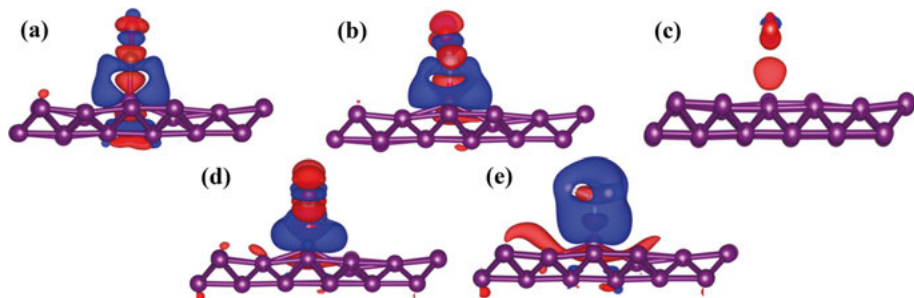


Figure 4.5. (a-e) Charge density difference for gas adsorptions (CO, NO, CO₂, NO₂, and NH₃, respectively) on borophene sheet. Isovalues cutoff is taken as 0.003 e/Å³. Red and blue color indicates the electron gain and electron loss respectively. Reproduced with permission from Paper IV. Copyright ©2017 American Chemical Society.

advocates the physisorption. For a better conclusion of the adsorption process, the charge transfer (Bader charges) associated with the binding of the gases on

the borophene surface is tabulated in the Table 4.1. These charge transfers are validated from the spatial charge distribution in Fig. 4.5, which has been calculated by using the expression $\Delta\rho(\mathbf{r}) = \rho_{B+gas}(\mathbf{r}) - \rho_B(\mathbf{r}) - \rho_{gas}(\mathbf{r})$, where $\rho_{B+gas}(\mathbf{r})$ is the charge distribution on borophene with adsorbed gases, $\rho_B(\mathbf{r})$ is the charge distribution on borophene and $\rho_{gas}(\mathbf{r})$ is the charge distribution on isolated gas molecules. Charge density difference picture confirms the stronger binding for all the gases except CO₂. These charge transfer tabulated in the Table 4.1 matches well with the Fig. 4.5. Detailed explanations have been provided in paper IV. Furthermore, the influence of gas adsorption on the electronic structure of borophene is depicted in Fig. 4.6, where it presents the density of states (DOS) of gas adsorbed sheet with projected density on the gas molecule for all the gases. As described earlier, CO₂ gas shows the lowest adsorption energy in Table 4.1 and from Fig. 4.6(b), it can be confirmed because there is a negligible influence of the CO₂ adsorption on borophene electronic structure. However, remaining gases induce some changes in the

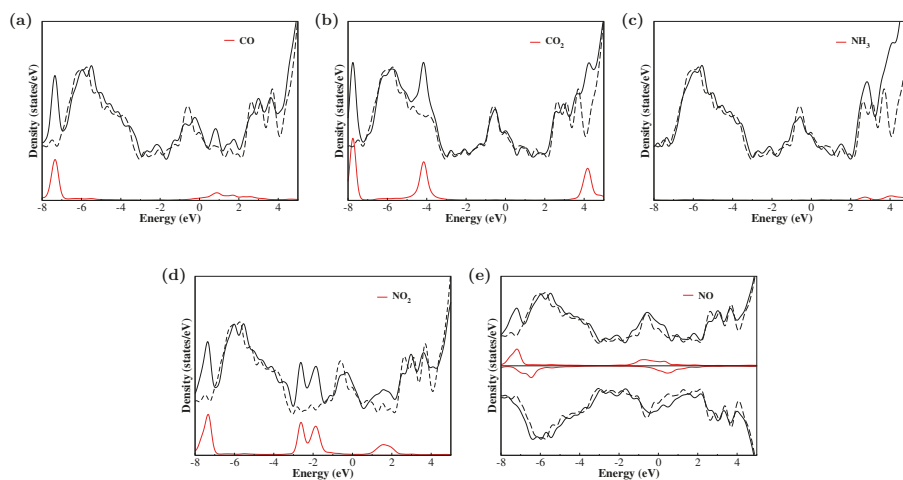


Figure 4.6. Total density of states (black) and projected density of states for different gases in red color (a-e). Density of states for pristine borophene is represented with dash lines. Fermi level is shifted to zero in each case. Reproduced with permission from Paper IV. Copyright ©2017 American Chemical Society.

DOS (broaden the peak) particularly around the Fermi level, which can be confirmed by comparing the total DOS with the pristine borophenes DOS (dashed lines in Fig. 4.6). In the case of CO molecule, the broadening of peak happens around 1 eV due to hybridization of LUMO level of the gas molecule with the states of borophene. For the tetra atomic gas NH₃, one can see hybridization around the Fermi level results in broadening of the of DOS. Further, paramagnetic gases NO and NO₂ withdraw charge from the borophene surface which can be seen in the Table 4.1. In the case of NO gas, the broadening of the peak around the Fermi level advocates the strong binding and charge trans-

fers. Spin-up and spin-down cases of DOS in Fig. 4.6(e), suggest the magnetic behavior of the adsorbed system [163]. This magnetization occurs because of the unpaired electron in NO gas. The NO₂ adsorbed system deserves special attention because it does not show magnetic behaviors in DOS. The states below the Fermi level are hybridized with boron *p* orbital, which makes it non-magnetic [163]. The clear picture of non-magnetic DOS of NO₂ can be found in supporting information of paper IV, where the *p*DOS of the molecule is presented with variable distance from the surface, which describes relaxed configuration (bonding) as nonmagnetic and the nonbonding configuration as magnetic one. From strong binding energy, charge transfer, and DOS analysis,

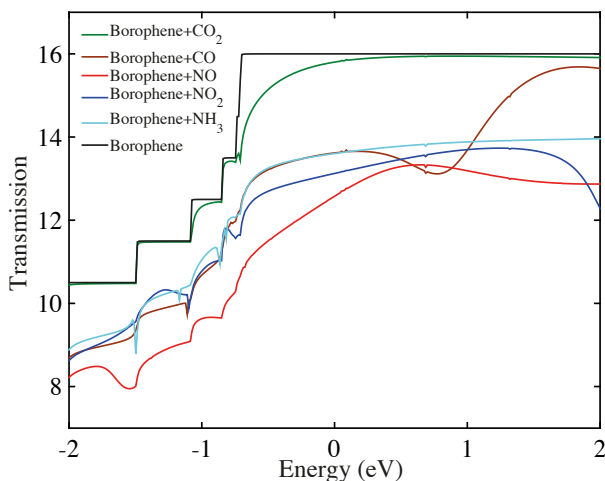


Figure 4.7. Zero bias transmission for pristine borophene and borophene with gas systems. Reproduced with permission from Paper IV. Copyright ©2017 American Chemical Society.

it is pertinent that the influence of gas molecule on the borophene surface will produce different sensitivity in the resistivity measurements. To understand this, the zero bias transmission functions are represented in Fig. 4.7 for all the systems. These transmission functions are plotted for the transport setup in *x*-direction of borophene sheet, which stands for high conducting direction. A noticeable difference can be seen due to the effect of gas adsorption in transmission spectra. Reduced transmission advocates the back scattering which inhibits the conduction channels in borophene sheet. CO gas induces small change in transmission whereas CO₂ has a negligible effect. As discussed before from DOS pictures, the paramagnetic gases show clear variation, which is relevant to their adsorption energies and charge transfers. The same trend can be seen for NH₃ gas adsorption also. Furthermore, these changes in transmission are also explained with the current-voltage characteristics and this can be found in Paper IV. In summary, the high adsorption energies for most of the

gases, charge transfer and quenched transmissions demonstrate the possibility of designing a borophene based gas sensor nanodevice.

4.3 S/Si substituted black phosphorus

Among several applications, black phosphorus (BP) has also been reported for selective gas sensing in both experiment and theory [164–167]. BP monolayer shows good sensitivity and selectivity towards the gas molecules. In the theoretical report, Kou *et al.* [164] showed that the changes in the I-V characteristics emerge at relatively higher bias in transport calculations due to its band gap of 0.9 eV in GGA calculation. In this work, the structural, electronic and transport properties of the silicon and sulfur doped BP sheet have been investigated. Further, the properties of gas molecule adsorption on these doped BP sheets are demonstrated. Fig. 4.8 (top panel) presents the top and side

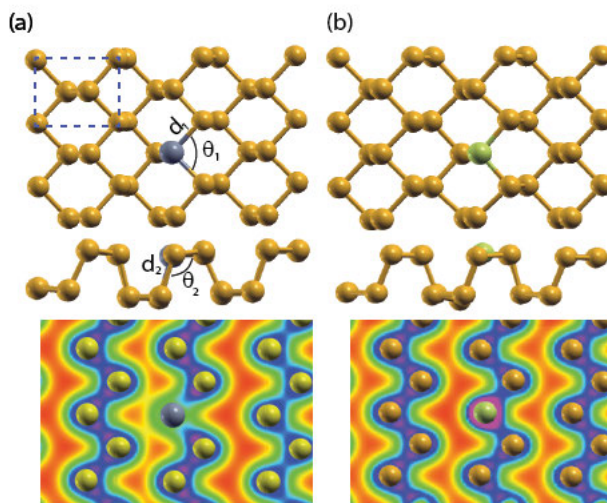


Figure 4.8. (a) The optimized structures of Si- and S-doped BP with bond length defined by d_1 and d_2 . The dashed line shows one unit cell of BP (b) The electron densities plotted for isovalues of $0.08 e \times \text{bohr}^{-3}$.

view of the relaxed structures of Si-BP and S-BP supercells, respectively. The intraplanar and interplanar bond lengths (d_1 and d_2) along with the intraplanar and interplanar bond angle (θ_1 and θ_2) are illustrated in Table 4.2.

For Si-BP, the geometrical configurations (d_1 , d_2 , θ_1 and θ_2) are slightly different from those of pristine BP because the radius of silicon is comparable with phosphorus. Still, the substitution of Si atom (four valence electrons) with a phosphorus atom (five valence electrons) modifies the electronic structures and chemical properties of BP. Only three of four valence electrons of Si are utilized for bonding with neighboring P atoms, leaving one electron

Table 4.2. Intraplanar (d_1) and interplanar (d_2) bond lengths and bond angles (θ_1 and θ_2) in pristine BP, Si-doped BP and S-doped BP.

Device	$d_1(\text{\AA})$	$d_2(\text{\AA})$	$\theta_1(^{\circ})$	$\theta_2(^{\circ})$
BP	2.24	2.26	96.6	101.6
Si-BP	2.29	2.30	93.2	106.8
S-BP	2.20	2.92	101.1	102.6

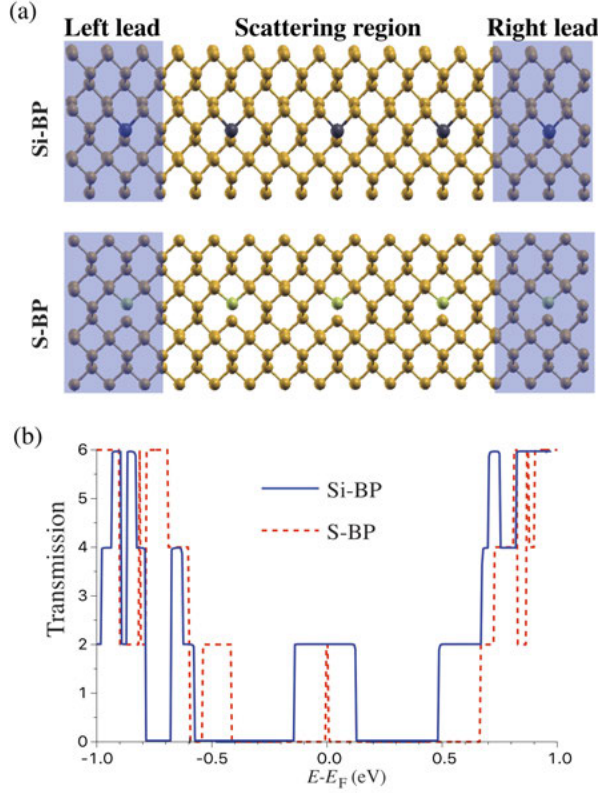


Figure 4.9. (a) Device setup used for Si-BP (upper) and S-BP (lower). The first-principles quantum transport simulation consists of a scattering region and two semi-infinite leads. One unit cell of lead is shown in blue (b) zero-bias transmission coefficients as a function of energy for Si-BP (solid line) and S-BP (dotted line) devices.

relatively free to move. Whereas, in the case of S-BP, sulfur has six valence electrons and requires two electrons to get stabilized. As a result, the sulfur atom forms chemical bonds with only two P atoms. This is consistent with d_1 and d_2 bond lengths between phosphorous and sulfur atoms in Table 4.2, since the interplanar P-S bond length ($d_2 = 2.92 \text{ \AA}$) is too large to form a co-

valent bond. Additionally, Fig. 4.8 (bottom panel) stands for the total charge density redistribution map due to the dopant atoms in BP by comparing the charge density of Si-BP and S-BP with the pristine BP, using the expression: $\Delta\rho(\mathbf{r}) = \rho_{\text{Si/S-BP}}(\mathbf{r}) - \rho_{\text{BP}}(\mathbf{r})$. It explains the fluctuation of charge density mostly around the dopant atoms. For Si-BP, one can see the less charge density (green) on Si atom, and the charge is accumulated around the P atom. This is due to different electronegativity values ($\text{Si} \ll \text{P} < \text{S}$). Conversely, the electronic charge is concentrated (pink) to S atom, which reinforces the assumption that the charge is localized on the dopant for S-BP following from the presence of two electron lone pairs.

Further, concentrating on electronic transport, the zero-bias transmission coefficients, $T(E)$ for Si- and S-BP devices are displayed in Fig. 4.9(b). By looking at the transmission coefficients of the Si-BP device (solid line), one can perceive that there are two conducting channels which are associated with the Si dopant in the energy window range of approximately from -0.15 to 0.15 eV around the Fermi level. In the case of S-BP device (dash line), there is a narrow resonant peak in the transmission at the Fermi energy. At lower energies, however, S-BP exhibits a transmission enhancement due to a more conducting path, mimicking its p DOS for those corresponding energy ranges ($-0.5 \text{ eV} > E > 0.5 \text{ eV}$) (see in paper V). Therefore, it is reasonable to conclude that the nonbonding $3p$ electrons of neighboring P atom around S atom are more localized, whereas in Si case, the unpaired valence electron of Si atom is free to move and contributed to the metallic property and conductance.

Table 4.3. *Calculated binding energies (E_b) and shortest distance between the molecule and surface (d_a).*

Gas	Si-BP		S-BP	
	E_b (eV)	d_a (Å)	E_b (eV)	d_a (Å)
CO	-0.02	2.53	-0.04	3.02
NH₃	-0.18	2.40	-0.06	2.97
NO	-1.48	2.07	-1.50	1.78
NO₂	-2.09	1.98	-1.18	2.10

After deliberation of electronic structure and transport properties of periodically doped BP, the gas sensing capabilities of these nanodevices are explored with four different gases (CO, NO, NO₂ and NH₃). Fully relaxed and the most stable configuration of adsorbed gas systems are shown in Fig. 4.10. Binding energies for these configurations are tabulated in Table 4.3 along with

the smallest binding distances from the surfaces. All these four gases prefer binding with Si impurity for Si-BP case, as shown Fig. 4.10(a). The binding energies for NO and NO₂ show higher values than those for the NH₃ and CO. This shows Si-BP device is more sensitive towards former two gases. The reason behind this is an extra electron in the Si atom, which can be shared by the paramagnetic gases during binding. The case of S-BP shows that NO and NO₂ prefer to be chemisorbed on the P atom close to the doping site, whereas CO and NH₃ adsorbed weakly on the top of S atom due to very weak interaction. NO and NO₂ are electron withdrawing gases, but S site in the surface is more electronegative than rest of the surface, therefore these radicals move on the top of the P atom. To further indulge into adsorption process and understand

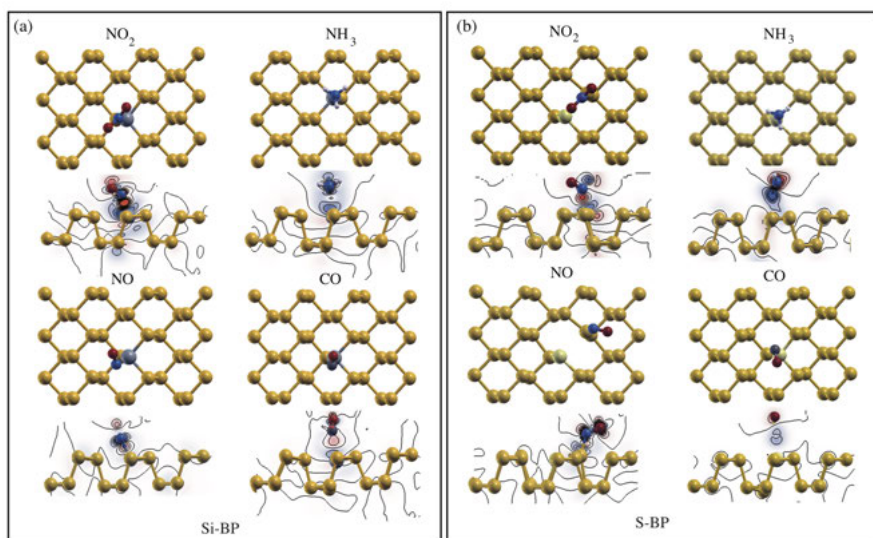


Figure 4.10. The most stable adsorption configurations of the NO₂, NH₃, NO, and CO molecules (upper) and charge density differences of (a) Si-BP and (b) S-BP, blue and red color represent charge depletion and accumulation, respectively.

the charge reorganizations, the spatial charge distribution is plotted for these two set of devices with different gases adsorbed, are shown in Fig. 4.10 in the form of the two-dimensional contour plot. Strong charge accumulations can be seen for Si-BP and S-BP in the case of NO and NO₂ between the layer and gas. This charge accumulation is associated with the hybridization of orbitals. In the case of Si-BP device, gases sit on the top of Si atom and bind with N atom, sharing charge to the unpaired electron induced by Si dopant. For S-BP, the charge is concentrated on the S dopant since its electronegativity is higher than that of P atoms. As discussed in the previous section, the S atom forms two chemical bonds with P atoms. As a result, there is nonbonding 3p electron of neighboring P atom which adsorbs the NO and NO₂ gases. Orbital hybridization is absent for CO molecule on the sensor surface implies no

charge sharing, whereas for NH_3 there is less charge accumulation in between surface and gas in both the devices. Therefore, it is correct to argue that Si- and S-BP are sensitive towards the nitrogen-based gases, especially for NO and NO_2 .

The most important feature of an experimental device for sensing is resistivity/conductivity measurements. The variation in conductance proffers the signature of the adsorbate. This property is referred as sensitivity and defined as $S(\%) = \frac{|G - G_r|}{G_r}$, where G and G_r are the zero bias conductance for the nanosensor with and without the gas molecule, respectively. Transmission

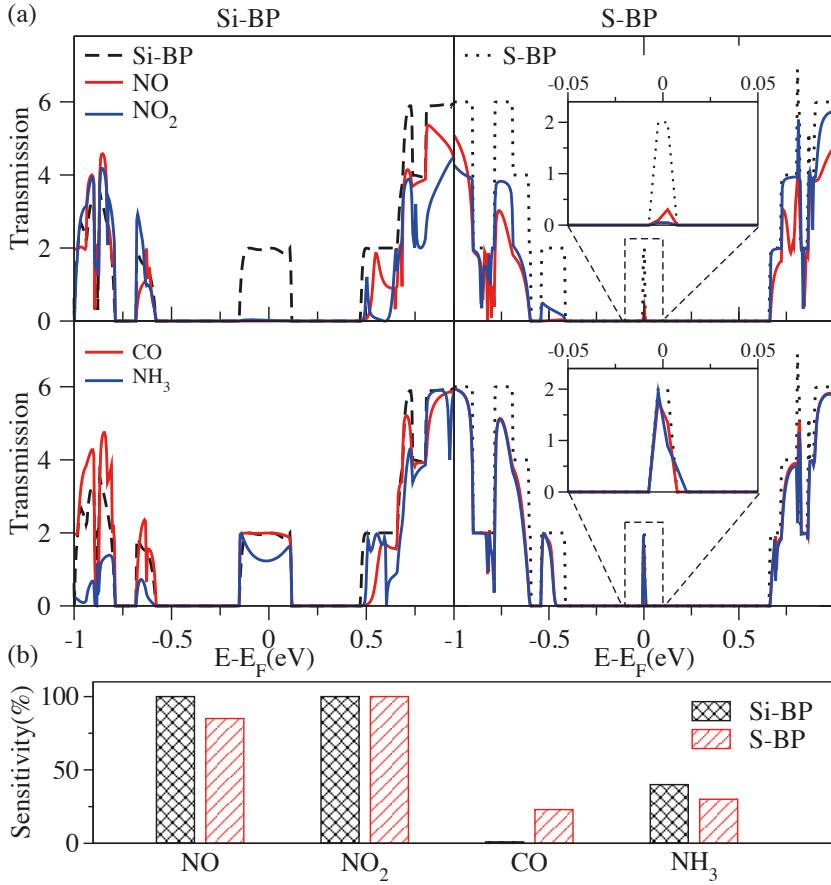


Figure 4.11. (a) Zero-bias transmission coefficients as a function of energy for NO, NO_2 , CO and NH_3 adsorbed on Si-BP (left panel) and S-BP (right panel), respectively, as compared to that in the absence of gas (b) sensitivity for different gases on two respective devices.

for paramagnetic gases NO and NO_2 are shown in the upper panel, whereas lower panel stands for CO and NH_3 in Fig. 4.11(a). Si-BP device exhibits the complete suppression of transmission peak around Fermi level for NO and

NO₂ adsorption. Moreover, NH₃ adsorption shows damped transmission at the Fermi level, and upon the CO gas adsorption, it remains nearly the same due to the lowest adsorption energy and no charge transfer (see Table 4.3). Additionally, S-BP device shows nearly the same trend for NO₂, but the NO gas adsorption does not suppress the transmission peak entirely. For the adsorption of CO and NH₃, the T(E) peaks at the Fermi energy are slightly shifted to the lower energy, as compared to that of the S-BP without gas. As we have discussed above regarding the unpaired valence electron of the Si-doped devices and the nonbonding electron of neighboring P atom around S, it is reasonable to assume that the charge sharing between the adsorbate and surface gives rise to valence saturated device and attributes to the decrease in conductance. These changes in the transmissions for different gases in both the devices are in agreement with the binding energies presented in Table 4.3.

Fig. 4.11(b) displays the sensitivity in the two nanodevices for different gases. It is evident that both the nanodevices have high sensitivity towards the paramagnetic gases. NH₃ adsorption reveals the relatively lower sensitivity for S-BP device than the Si-BP devices. In the case for CO, we have negligible sensitivity in S-BP and no sensitivity in Si-BP device. It is visible that these two nanodevices are sensitive towards most of the gases, but selectivity can be the issue in resistivity measurements for the paramagnetic gases. However, It is possible that these two paramagnetic gases may differ in transmission at increased bias. From this study, one can understand that the periodically doped BP has higher sensitivity than the pristine BP at zero bias transmission around the Fermi level. For both devices, the sensitivity is seen to be ordered in the following hierarchy: $S_{\text{NO}_2} \geq S_{\text{NO}} \gg S_{\text{NH}_3} > S_{\text{CO}}$. These sensitivities are significantly correlated with the amount of binding energy; more is the binding energy of the absorbed gas, greater is the sensitivity it has. For further detailed analysis, see Paper V.

5. 2D materials for anode application in rechargeable batteries

Materials have played important roles in energy production, conversion, and storage. However, nowadays there are even more significant challenges to conquer, i.e., whether the materials can meet their high-performance demands. Li-ion batteries have been widely embraced in modern-day technologies working as a vital power source for portable electronic devices. The traditional Li-ion battery anodes based on graphite and commonly used cathodes are undergoing constant developments due to the vast emphasis on high energy density, efficiency and as well as low cost. Therefore, the need for next-generation energy storage devices which can produce high capacity and capability inspires the community to search for new electrode materials. Taking these issues into account and considering high surface to volume ratio, abundant active sites, while maintaining the low dimensions which help them to outperform concerning their bulk counterpart, makes 2D materials a promising choice for an electrode in Li/Na-based batteries.

Taking earlier mentioned advantages as an inspiration, in this chapter, results produced using first principles methods to model the various newly predicted and synthesized 2D materials for battery anode applications are discussed. In the first three sections, some background information about the modeling are introduced; further, the different cases of 2D materials are discussed briefly with essential results.

5.1 Intercalation profile

In the intercalation process (reaction), lithium atoms are incorporated into the crystalline structure of the host material, and electrons are added to its band structure. The first establishment of lithium insertion voltage by the use of first principles calculations was proposed in 1992 for Li_xAl system [168, 169]. Further, in 1997 Ceder with his co-workers explained, how the lithium insertion voltage of transition metal oxides can be surmised from the calculated total energies of the host compound and that of the lithium metal [170–172]. Although their method was reported for cathode electrode, where they considered the pure Li metal as an anode but this same method can be applied to investigate the intercalation profile in the anode materials. The intercalation reaction that occurs in the process of adsorption of Li in the host compound

for two different phases can be expressed as

$$(x_2 - x_1)Li + (Li_{x_1}h) = (Li_{x_2}h), \quad (5.1)$$

where x_1 and x_2 stand for two different concentration of adsorbed Li-ions. Li stands for the metallic lithium in body centered cubic (*bcc*) structure with a constant chemical potential μ_{Li} , and h describes the host material as an anode. The cell voltage of the intercalation reaction described in Eq. (5.1) depends upon the partial molar free energy, G or chemical potential, μ . As the amount of host moles N_h are constant and $N_{Li} = x_{Li}N_h$, one can write chemical potential as a variation of Gibbs free energy for Li concentration x_{Li} as

$$\mu = \left(\frac{\partial G_r}{\partial N_{Li}} \right)_{T,P,N_h} \approx \left(\frac{\partial G_r}{\partial x_{Li}} \right)_{T,P,N_h}. \quad (5.2)$$

Here G_r defines the Gibbs free energy of the intercalation process of the reaction defined in Eq. (5.1). Further, using Nernst equation the average voltage (\bar{V}) of reaction (5.1) can be written as

$$\bar{V}(x_2, x_1) = - \frac{\Delta G_r}{(x_2 - x_1)zF}, \quad (5.3)$$

here F stands for the Faraday constant, z is the charge of the intercalating ion ($z = 1$ in the case of lithium). Further, the Gibbs free energy can be written approximately in terms of energies as

$$\Delta G_r = \Delta E_r + P\Delta V_r - T\Delta S_r. \quad (5.4)$$

The above equation can be approximated by considering that only the solid phases are involved at equilibrium. The term $P\Delta V_r$ is of the order 10^{-5} eV and ΔE_r is normally in the order of 3 to 4 eV. Therefore, $P\Delta V_r$ term can be ignored. All the stability assessments in this process are carried out at zero temperature. Hence, the entropy term will not be taken into account [173]. Finally, the Eq. (5.4) becomes $\Delta G_r = \Delta E_r$, and ΔE_r can be determined directly from the electronic structure calculations for the reaction (5.1). Further, by using Eq. (5.4) into Eq. (5.3), the average voltage of the reaction, $\bar{V}(x_2, x_1)$ can be calculated as

$$\bar{V}(x_2, x_1) = - \frac{E(Li_{x_2}h) - (x_2 - x_1)E(Li) - E(Li_{x_1}h)}{(x_2 - x_1)}. \quad (5.5)$$

Here, E refers to the total energies per formula unit of the respective compounds. Thus, the calculation of ΔE_r yields the predicted cell voltage that is averaged over the value of the concentration limit x_1 and x_2 , where $x_2 > x_1$.

At equilibrium condition, the free energy function of the system, ΔG_r , must be a convex function of the reaction extent because the electrode should achieve the thermodynamic stability at each given concentration. However,

Eq. (5.3) can be used to calculate the stepwise approximation to the voltage curve. Here comes the real challenge in determining the thermodynamically stable phases and their respective structures. The stability of the different phases can be compared by the quantity ΔE_r , which is also referred as the formation energy with respect to the stable reference materials. For example, we consider two end structure as the full coverage of host material (1 Li per formula unit of the host) Li_h and the host materials as h . Further, the formation energy for any concentration (x) of Li is described as

$$\Delta E_r(Li_xh) = E(Li_xh) - (x)E(Lih) - (1-x)E(h). \quad (5.6)$$

If the different phases of Li_xh are thermodynamically stable, then the formation energies of these phases of Li_xh with its reference phase must lie on the convex hull of ΔE_r versus Li concentration x .

Once the convex hull construction is defined, one can calculate the piecewise voltage profile by using Eq. (5.3). The composition of x_{max} for which the electrochemical potential (voltage) vanishes and sets the end of the electrochemical reaction, defines the theoretical specific capacity of the electrode material. This theoretical specific capacity can be calculated using the formula

$$C_m = \frac{x \cdot z \cdot F}{3.6 \cdot MW(h)}, \quad (5.7)$$

where x stands for the total number of Li intercalated in the systems and z describes the number of electrons involved in the process. $MW(h)$ is the molecular weight of the host material.

5.2 Basin-hopping

It has been discussed in the previous section that one can figure out the stable phases with different concentration of Li in the host material by using Eq. (5.6), which further participates in calculating the average voltage. Therefore, it is important to define the accurate description of the equilibrium structure of modified compound during the lithiation of the surface at each given concentration of Li given by x . It can be probed by exploring the material's potential energy surface (PES) and searching for its energy minimum (most thermodynamically stable structure). These procedures are known as Steepest Descent and Conjugate gradient, are implemented in most of the DFT codes which use the Hellmann-Feynman scheme [123, 125]. However, these methods are not good when the structure is far away from the equilibrium or different polymorph exist at a given chemical composition. Therefore, more sophisticated methods are required to ensure that the materials PES are accurately sampled. We start with an arbitrary structure and generate new structures by randomly displacing the Li atoms on the top of the surface.

Basin-Hopping (BA) scheme, firstly proposed by David J Wales *et al.* [174], has been used in the work in this thesis. It is based on the idea of transforming the PES into interpenetrating local minima forming basin, see Fig. (5.1). In this scheme, a local structural relaxation is performed for each newly generated structure by randomly displacing Li. The total energy related to any configuration is mapped to that of local minima computed with the local optimization method. After this, the PES is transformed into a set of staircase with plateaus correlated to a given minima after local optimization. Predicted structures are accepted or discarded on the basis of change in the total energy (ΔE) via Metropolis algorithm. If $\Delta E \leq 0$, the composite structure is used as the new guess structure and if $\Delta E > 0$, the new structure is assigned to a probability $P(E) = e^{-\frac{\Delta E}{k_B T}}$, which leads to a canonical ensemble of atomic configurations at T .

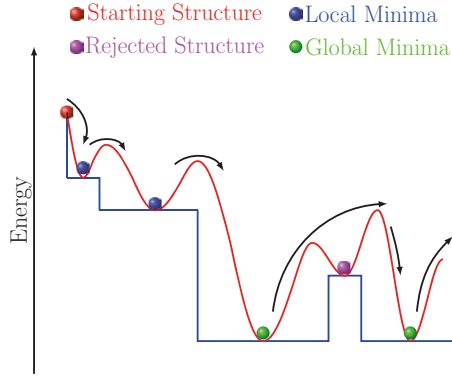


Figure 5.1. Schematic representation of the Basin-hopping procedure. Arrows show stochastic transformations and the solid blue line stands for transformed PES.

5.3 Nudged elastic band method

Diffusion mechanisms reported in this part of the thesis are computed using Nudged Elastic Band (NEB) method implemented in VASP [123]. This method was developed by H. Jónsson *et al.* [175] as an enhancement of the chain states method, where the main objective is to determine the minimum energy pathway (MEP) connecting two local minima on a potential energy surface. The activation barrier and the transition state associated with the reaction can be obtained from the minimum energy pathway. First, the set of images $([r_0, r_1, r_2 \dots r_n], n - 1 \text{ replicas})$ in the linear interpolation between the two ends are initiated. This is the most important part of the NEB method to get the optimum initial guess of the images to converge the MEP. The force, minimizing the energy of each image is defined as $\mathbf{F} = \nabla E(r_i)$, where $E(r_i)$ can be obtained from a ground state DFT calculation. Further, to prevent the

movement of the images from their minimum energy path configurations, a spring constant is added. Hence, the total force on an atom will be the sum of the true force perpendicular to the local tangent and the spring term along the local tangent. The projection of the parallel component of the true force acting on the images and the perpendicular component of the spring force is canceled. Hence, one can write as

$$F_i = F_i^s|_{\parallel} - \nabla E(r_i)|_{\perp}, \quad (5.8)$$

further, these projections in Eq. (5.8) are described as

$$\nabla E(r_i)|_{\perp} = \nabla E(r_i) - \nabla E(r_i)\hat{\tau}_i, \quad (5.9)$$

and

$$F_i^s = k(|r_{i+i} - r_i| - |r_i - r_{i-1}|)\hat{\tau}_i. \quad (5.10)$$

Here, E is the energy of the system, which is a functional of all the atomic coordinates, $\hat{\tau}_i$ is the normalized local tangent at any described image i , and k is the spring constant. The program runs each image simultaneously and describes the forces at the end of the each ionic cycle to compute the forces acting on each replica. Spring force defined in Eq. (5.10) assures the same spacing in the images. The minimization of the forces acting on the images tries to bring the NEB to MEP. However, due to a small number of images for the length of the path, typically none of the images lands over at the saddle point at the end of the minimization process, hence, the saddle point energy needs to be estimated by interpolation [176]. The climbing image NEB (CI-NEB) method was developed to solve this problem with a small modification to the NEB method. A precise convergence to a saddle point is achieved while maintaining the information about the shape of MEP. This does not cost extra computational effort since all the images are being relaxed synchronously. During the iteration of regular NEB, the image with the highest energy is determined. The force on this identified image is not described by Eq. (5.8), but calculated by,

$$F_{i_{max}} = -\nabla E(r_{i_{max}}) + 2\nabla E(r_{i_{max}})|_{\parallel}, \quad (5.11)$$

with $2\nabla E(r_{i_{max}})|_{\parallel}$ is doubled opposite of the true force parallel to the local tangent. This reverse force can adjust the climbing image to an energy minimum in all the directions perpendicular to the path and an energy maximum along the path. Thus, the image converges under this condition would be the exact saddle point. The highest energy image is no longer influenced by the spring constant. Therefore, the image spacing is no longer equal in CI-NEB method.

5.4 2D Si₂BN anode for rechargeable battery

Recently, Andriotis *et al.* [29] proposed a monolayer of 2D Si₂BN using first-principle calculations. Si₂BN monolayer was shown to be stable using phonon dispersion calculations and high-temperature molecular dynamics

simulations. The structure is composed of Si-Si-B-N arrangement in a single layer with each Si atom having Si, B, and N atoms as nearest neighbors, whereas, B (N) atom has two Si atoms and one N (B) atom as nearest neighbor. The structural arrangement can be seen in Fig. 5.2, where it is clear that this configuration avoids the formation of energetically unfavorable B-B and N-N bonds. Si_2BN shows metallic property, and Si centers are in electron deficient condition, which works as an electron reservoir. Metallic behavior and active

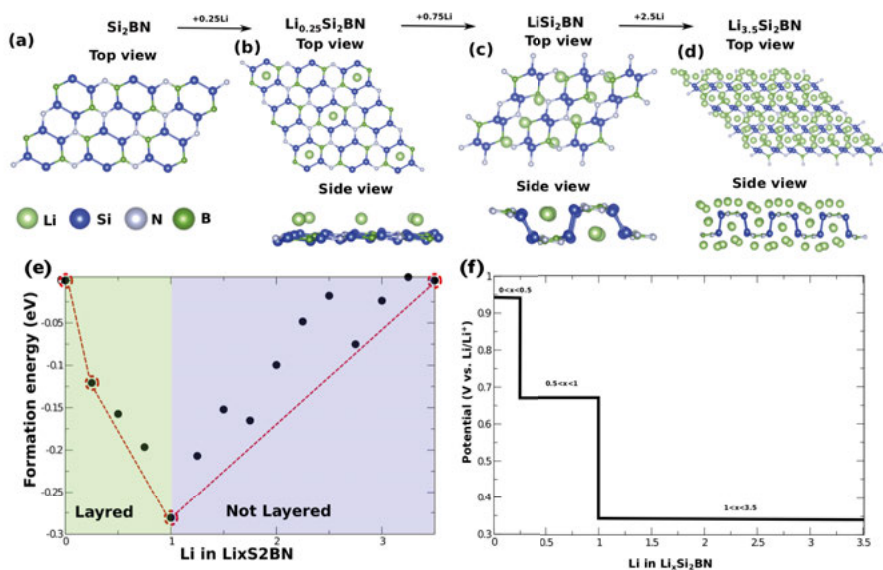


Figure 5.2. Global minimum structures of $\text{Li}_x\text{Si}_2\text{BN}$ appearing in the tie line of the convex hull are shown in (a-d), where x assumes the values of (a) 0, (b) 0.25, (c) 1 and (d) 3.5. Buckling of the original planar structure happens after $x = 1$ is noteworthy. (e) Convex hull and (f) potential with respect to the concentration of Li are shown in the bottom panel. Reproduced with permission from Paper VI. Copyright ©2017 ELSEVIER.

sites in this material prove advantageous for an advance battery anode application. Relatively high adsorption energy for Li/Na atoms and good charge transfer from Li/Na atom to the surface established it for further investigations. To further investigate the ionic insertion potential, different concentrations of Li/Na atoms in host compound are calculated to find out the global minimum structure and further, these structures were converged with high convergence criteria to calculate the ground state energy. The concentrations (x) are varied from 0 to 3.50 for Li case and from 0 to 3.25 for the Na case in the form of $\text{Li/Na}_x\text{Si}_2\text{BN}$. The computed internal energies of these structures are analyzed for the relative thermodynamic stabilities through the convex hull plot, that can be seen in Fig. 5.2(e) for Li case. Phases existing on the tie lines of the convex hull are only the stable structures and rest of them may be disproportionate and form the two-phase electrode. Hence, the computation of adsorption potential

is done by considering only the stable phases lying on the tie line of convex hull, shown in Fig. 5.2(f). It can also be seen that this material undergoes a phase transformation from planar to puckered after the insertion of 1 Li/Na per formula unit and at a potential of 0.67 V for Li/Li⁺ adsorption, and 0.60 V for Na/Na⁺ adsorption. It is concluded that the filling of antibonding states creates some level of stress in the structure leading to the puckered phase formation [177]. Further, insertion of Li/Na gives us the ultimate potential which comes out to be 0.34 V vs. Li/Li⁺ at the concentration of 3.50 Li and 0.09 V vs. Na/Na⁺ for the concentration of 3.0 Na per Si₂BN, respectively. This leads to a very high theoretical specific capacity of 1158 mAh/g for Li and 1076 mAh/g for Na based systems.

Another parameter, which decisively governs the performance of the battery is the kinetics of the electrochemical reaction. Therefore, it is essential to quantify the diffusion barrier for Li and Na on the Si₂BN surface. In most of the cases, ionic mobility influences the power delivered by the battery. However, unlike graphene, there can be different pathways possible for Si₂BN because of its tri-elemental surface [177]. Only the diffusion between two similar configurations specific to the case of the most favorable binding site (at the center of Si₄B₂ ring) is considered. The first case shows that the ions move from the center of the hexagonal ring (Si₄B₂) to the center of the next Si₄B₂ ring through a Si₄N₂ ring. In the second investigated path, ions hop from the center of the Si₄B₂ hexagonal ring to another Si₄B₂ ring through Si₂BN ring. The diffusion barriers are calculated using CI-NEB methods. In Li-ion case the barrier comes out to be 0.48 eV for both the defined pathways, whereas for Na-ion case these barriers are 0.32 eV and 0.4 eV for the two respective pathways. The detailed explanations, schematic illustrations, and MEP plots are given in Paper VI in this thesis.

5.5 Hydrogenated 2D boron anode for rechargeable battery

The two-dimensional polymorph of boron (borophenes) have been discussed in the previous chapter. However, its synthesis involved stringent condition such as the use of ultra-high vacuum and Ag substrate [27, 28]. Few practical challenges such as high energy and chemically reactive surface of the sheet, make it difficult to have it in the free-standing form. However, it is essential to have a stable sheet for further application of 2D boron. In this quest, several experimental and theoretical efforts have been made to realize the stabilized boron in 2D forms [178–180]. Boron atoms are electron-deficient as their three valence electrons occupy four available *s* and *p* orbitals, which encourages various bonding characters. In the attempt to compensate the electron deficiency of boron, its hydrogenation is a practical approach to stabilize the sheet [178, 179]. Keeping the context of limited stability in free-standing

form, the first-principles study by Xu *et al.* [157] proposed that borophene can be stabilized by complete surface hydrogenation. The resulting materials called as borophane, possess directional dependent Dirac cone and linear dispersion relation, which is reminiscent of graphene. Further, borophane structure is explored for various properties using DFT, like ferroelastic and auxetic properties of borophane explored by Kou *et al.* [181] with asserting its application in microelectromechanical and nanoelectronic devices. Similarly, the directional dependence of the electronic transport properties of pristine borophene and borophane were explored in recent *ab initio* calculations [158]. These theoretical reports drive the inquisitiveness for the experimental realization of 2D sheet of hydrogen boride (alternatively, hydrogenate borophene, borophane or boron hydride). Nishino *et al.* [179] used robust cation exchange method to experimentally realize the boron hydride sheet, which differs from the theoretically predicted borophane. Soon after the realization, this got a significant attention and was investigated for thermal conductivity, electronic and optical properties [182]. Inspired by the previous investigation of pristine borophene polymorphs for possible battery anode application and their exciting results, it is interesting to investigate hydrogen boride for its possible role as an anode electrode in rechargeable batteries. In the next section, both the polymorph, referred as B_2H_2 and BH, will be discussed for Li/Na ion battery application.

5.5.1 2D B_2H_2 case

Surface of 2D B_2H_2 possesses a buckled structure with corrugations that are anisotropic (uncorrugated along x and corrugated along y) in nature as can be seen in Fig. 5.3. Hydrogenation alters the lattice parameter in direction x , whereas lattice parameter in y direction remains unchanged. Further, the buckling height comes out to be 0.84 Å, and B-H bond length is 1.18 Å. Metallic nature of the electronic structure is same as pristine, and the lower molecular weight suggests it to be a promising material for battery anode. Before exploring the potential of borophane as Li/Na battery anode, the structure has been proved to be dynamically stable by phonon dispersion curve. Furthermore, *ab initio* molecular dynamics (AIMD) simulation has also been conducted to check the stability. Partial hydrogenation has also been tried, which resulted in dynamically unstable structures. After defining the stability, adsorption energies are calculated for Li/Na atoms at different adsorption sites, which convey that the top of B-atom is the most favorable site with effective adsorption energies of -2.58 eV and -1.08 eV for Li and Na ions, respectively. To model the effect of operational battery, the concentration (number of atoms = 4, 8, 12, and 16) of Li/Na is varied systematically on the surface. For this purpose, swapping basin hopping method is employed, and after getting the lowest energy structures, ground state calculation is performed with a high

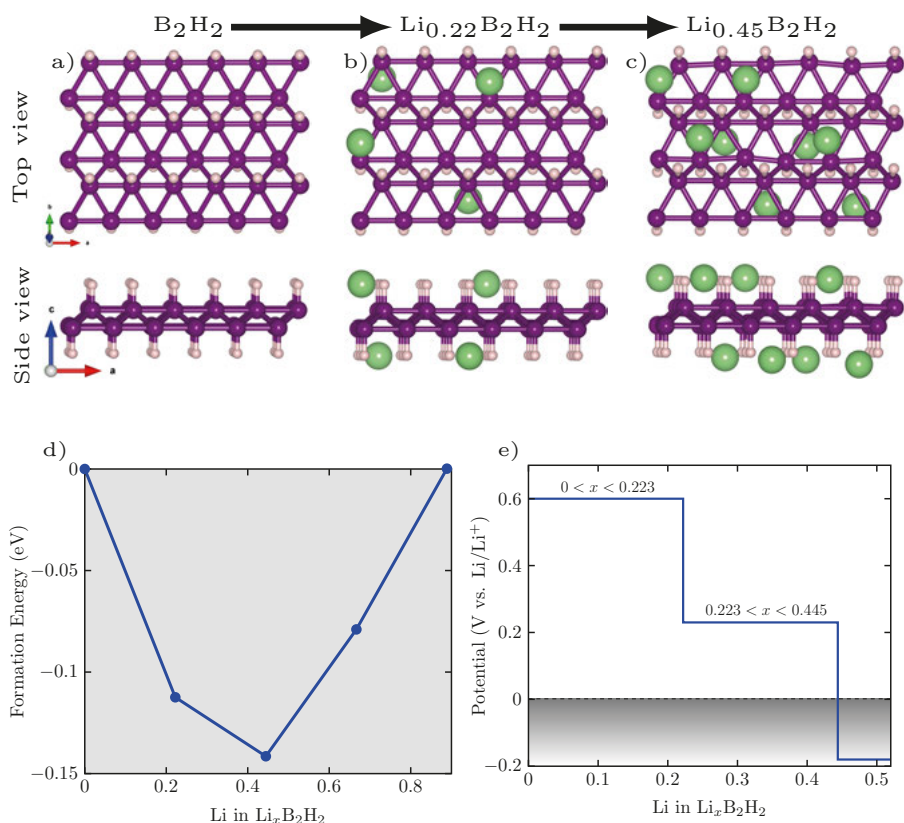


Figure 5.3. (a-c) Stable phase structure of $Li_xB_2H_2$ existing on the tie line of the convex hull along the intercalation process. In the lower panel (d) shows the formation energies of the compound $Li_xB_2H_2$ as a function of concentration (x) in eV per f.u. and (e) Li intercalation potential profile deals with only the phases appearing on the tie line of the convex hull for B_2H_2 substrate shown vs. Li/Li^+ . Reproduced with permission from Paper VII. Copyright ©2017 American Chemical Society.

level of accuracy. Fig. 5.3(d) shows that the phases with concentration x as 0.22, 0.45, 0.67, and 0.89 are stable between the two end structures, B_2H_2 and $Li_{0.89}B_2H_2$. These stable phases are further considered for calculation of insertion potential. Fig. 5.3(e) depicts the voltage profile with varying a concentration of Li in B_2H_2 and manifests two main plateaus. The first plateau shows a voltage of 0.61 V vs. Li/Li^+ , corresponding to the lithium concentration varying from $x = 0$ to 0.22. The second plateau lowers down to 0.23 V vs. Li/Li^+ with x value changing from 0.22 to 0.45. The next transformation, $Li_{0.45}B_2H_2 \rightarrow Li_{0.67}B_2H_2$, yields a negative value suggesting that the maximum concentration this sheet can be loaded with is $x = 0.45$. Hence, only the phases stable from the convex hull and possible from the intercalation potential are shown in Fig. 5.3(a-c). On the other hand, in Na case only one stable phase

described as $\text{Na}_{0.45}\text{B}_2\text{H}_2$ exists between the two end structure of the same concentration as Li case [183]. The average voltage for Na is computed as 0.03 V with the plateau from $\text{B}_2\text{H}_2 \rightarrow \text{Na}_{0.45}\text{B}_2\text{H}_2$. Further insertion results in the negative voltage. The details of sodium intercalation can be found in Paper VII in this thesis.

The maximum Li/Na concentration realized, i.e., $\text{Li}/\text{Na}_{0.45}\text{B}_2\text{H}_2$, brings out to an electrode with maximum theoretical specific capacity of the order of 504 mAh/g for both the Li and Na-ions, together with an average open circuit voltage of 0.43 V vs. Li/Li^+ for the Li insertion and 0.03 V vs. Na/Na^+ for the Na intercalation. Borophane offers higher capacity than the graphite (371 mAh/g), well established as the anode material for Li rechargeable battery. In case of Na, the theoretical capacity of borophane (504 mAh/g) is greater than that of reported for MoS_2 [184] with a theoretical capacity of 146 mAh/g or the case of Ti_3C_2 [185] with a capacity of 351.8 mAh/g. The diffusion barrier of Li and Na on the B_2H_2 surface has two different minimum energy paths as defined along the linear atomic boron (in x -direction) and along the corrugation (in y -direction) [183]. The estimated barrier for Li case comes out to be 0.21 and 0.68 eV for the two pathways, respectively, whereas for Na, it comes out to be 0.09 and 0.37 eV in the respective directions. The detail description for diffusion pathways and barrier is given in paper VII.

5.5.2 2D BH case

After the brief description of the results from borophane (B_2H_2), we further take the case of experimentally realized 2D boron hydride (BH) sheet to explore its potential application in Li/Na ion battery. BH sheet possesses planer structure different than the previously discussed corrugated structure, predicted with first-principles calculations. This structure has hexagonal symmetry and metallic nature in electronic structure, which opens up a practical avenue to test this experimental structure for battery applications. Keeping this in hindsight, this 2D sheet is investigated to estimate the possibility as an anode for Li/Na battery. Adsorption energies calculation and charge transfer process supports the potential strength of BH to be tested as an electrode. The intercalation profile of Li and Na atoms in the BH sheet has been investigated.

Li concentration is systematically varied on both sides of the BH sheet. Swapping basin hopping scheme has been performed to check the minimum energy structure and further the stringent DFT calculation is performed to check the ground state energy. Li atom is varied from 0 to 18 (concentration $x = 0$ to 0.5) in 3×3 supercell. It gives the stable intermediate phases with 4, 10, and 14 Li atoms ($x = 0.11, 0.27, 0.38$ in Li_xBH), which can be seen in Fig. 5.4(b-d). From the idea of the convex hull, stable phases along the intercalation process can be identified in Fig. 5.4(e). These stable phases are responsible for the charging/discharging voltage profiles accompanying the ion intercalation. Fig. 5.4(f) depicts the different plateaus of potential (volt-

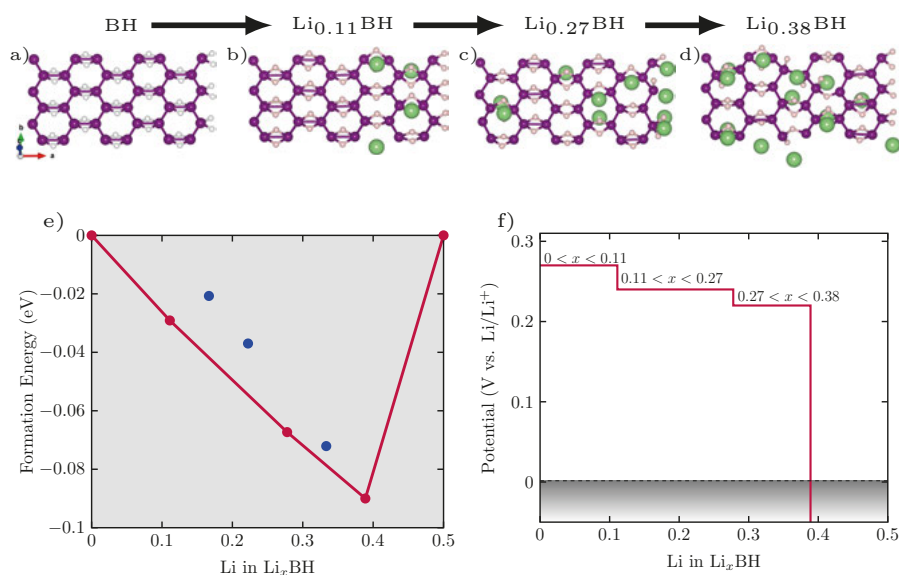


Figure 5.4. (a-d) Ground state structure of Li_xBH existing on the tie line of the convex hull along the intercalation process. Lower panel represents (e) the formation energies of the compound Li_xBH as a function of concentration (x) in eV per f.u. (these formation energies were calculated using the ground state structure resulted from basin hopping algorithm) and (f) Li intercalation potential profile deals with only the phases appearing on the tie line of the convex hull for BH substrate shown vs. Li/Li^+ . Reproduced with permission from Paper VIII. Copyright ©2018 Royal Society of Chemistry.

Table 5.1. Comparison of specific capacity, diffusion barrier and open circuit voltage (OCV) of two hydrogenated boron sheets (B_2H_2 and BH) materials for Li/Na-battery anode. Reproduced with permission from Paper VII and VIII. Copyright ©2017 American Chemical Society and ©2018 Royal Society of Chemistry.

Host	Li			Na		
	OCV (V)	Barrier (eV)	Capacity (mAh/g)	OCV (V)	Barrier (eV)	Capacity (mAh/g)
B_2H_2	0.43	0.21/0.68	504	0.03	0.09/0.37	504
BH	0.24	0.8	861.8	—	—	—

age) profiles with respect to Li concentration. The first plateau is related to

a step where the ionic concentration changes as $x = 0 \rightarrow 0.11$ and the delivered the potential as 0.27 V. In the similar fashion, the second and third plateaus correspond to the change in Li concentration as $x = 0.11 \rightarrow 0.27$ and $x = 0.27 \rightarrow 0.38$ with potentials of 0.24 V and 0.22 V, respectively. Further increment in concentration leads to the negative potential, which indicates that more lithiation would lead to dendrite formation. The computed average potential comes out to be 0.24 V, which is rather lower than most of the 2D materials. A noteworthy point about the potential profile is that the potential drop is rather constant along the lithiation process, which can be advantageous for the performance of the battery. On the contrary, in the case of the Na ion, we observe that the potential takes negative values right from the beginning of the intercalation process. Such estimations (potential profiles) are beneficial for checking the stability of the material from a thermodynamics point of view, and results indicate the unsuitability of BH for Na-ion battery. BH yields a high specific capacity of 861.78 mAh/g, which is considerably larger than that obtained by considering the computational structure of B_2H_2 (504 mAh/g). Table 5.1 stands for comparison of the potential of B_2H_2 and BH sheets for rechargeable battery applications. To understand the ionic mobility on the surface, diffusion barrier is estimated for Li-ion case. Only one path is possible for diffusion in this surface, and can be defined as ion moving from one hexagonal ring to another through the B-B bridge [186]. The diffusion barrier calculated using CI-NEB method is described in Table 5.1, and this comes out to be 0.8 eV, which is relatively high in comparison to the other 2D materials. See Paper VIII for the details.

5.6 S-Mxene and application in battery anode

Mxenes (transition metal carbides/nitrides/carbonitrides) are the emerging class of layered 2D materials [19]. These are found to be electrically conductive and stable in aqueous environments, a rare combination indeed, with huge potential in many applications [18]. Several reports delved the role of Mxenes for electrode materials in Li/Na-ion batteries, both experimentally and theoretically [95–97]. Mxene exhibits excellent capability to handle high cycling rates with good gravimetric capacities [187]. In this section, the investigation of the sulfur functionalized nitride Mxenes (V_2NS_2 and Ti_2NS_2) for Li/Na-ion battery anode application are discussed. These functionalized Mxenes are also metallic same as their pristine counterparts. The metallic behavior comes mainly because of d -orbital in the metal atom and some states also come from p orbital of the S atom. The adsorption strength for both the Li and Na atoms comes out to be better than several existing 2D material electrodes.

Further, same as the previous cases, the swapping basis hopping algorithm is performed to check the global minimum structures for the different Li/Na concentrations on the surfaces. Interestingly, for the Li case, both the surfaces can adsorb up to tri-layer of Li but the interplay between the formation

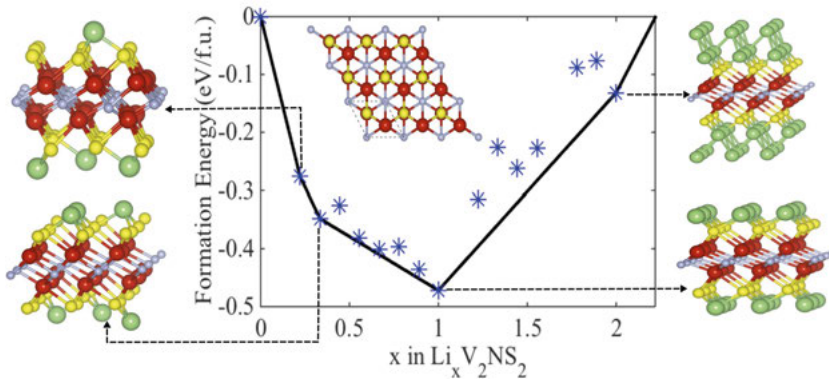


Figure 5.5. Formation energies vs. concentration of Li (x) in eV/f.u. for V_2NS_2 host. Fully relaxed structure with the concentration of stable phases ($x = 0.11, 0.22, 1$, and 2) are presented. (color code: V(red), N(gray), S(yellow) and Li(green)).

Table 5.2. Comparison of specific capacity, diffusion barrier and OCV of two host (Ti_2NS_2 and V_2NS_2) materials for Li/Na-battery anode.

Host	Li			Na		
	OCV (V)	Barrier (eV)	Capacity (mAh/g)	OCV (V)	Barrier (eV)	Capacity (mAh/g)
Ti_2NS_2	0.642	0.19	308.28	0.83	0.09	84.77
V_2NS_2	0.82	0.17	299.52	0.53	0.09	99.8

energy and OCV only allows up to bi-layer of Li coverage. To understand the intercalation of Li in bi-layer form the fully covered (full lithiation) surface, $Li_2V_2NS_2$ and $Li_2Ti_2NS_2$ are considered as the host material for further search of global minimum structure in the bilayer. This same process is repeated for tri-layer, where the host materials were considered as $Li_4V_2NS_2$ and $Li_4Ti_2NS_2$.

Furthermore, the higher level of accuracy is used to get the energies of ground state structure of lithiated systems. Convex hull plotted with two end structure as V_2NS_2 and $Li_2V_2NS_2$ ($x = 0$ to 2.2) is shown in Fig. 5.5. It can be seen that concentrations with $x = 0.22, 0.33, 1.0$ and 2.0 are the stable phases. In the case of Ti_2NS_2 , all the phases below the full coverage ($Li_2Ti_2NS_2$) are the stable phases and above the monolayer coverage only fully covered bilayer is a stable phase that can be seen in Fig. 5.6. In addition to this, the stepwise intercalation potential with respect to concentration of Li is shown in Fig. 5.7 for both the host materials. Intercalation potential in V_2NS_2 has four plateaus and

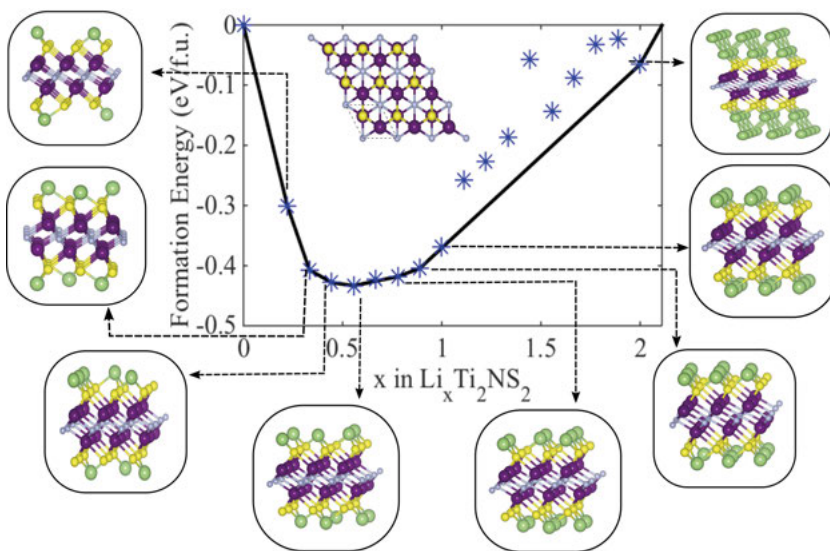


Figure 5.6. Formation energies as a function of Li concentration x in eV/f.u., global minimum structures of $\text{Li}_x\text{Ti}_2\text{NS}_2$ appearing in the tie line of the convex hull. (color code: Ti(purple), N(gray), S(yellow) and Li(green)).

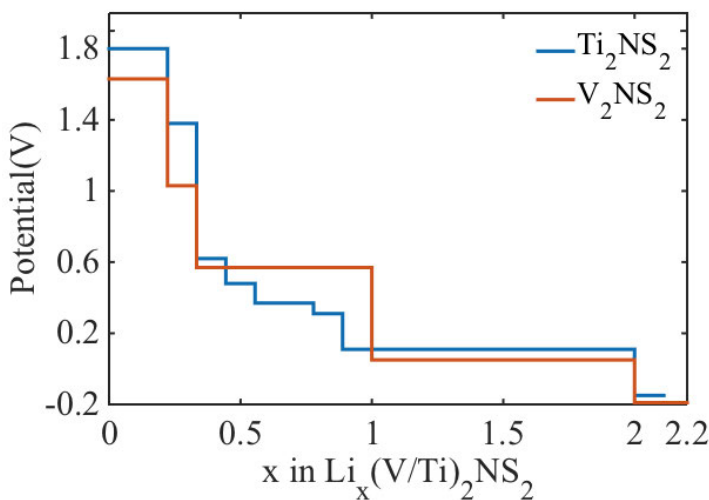


Figure 5.7. Li intercalation potential profiles for V_2NS_2 and Ti_2NS_2 . The results presented here are shown vs. Li/Li^+ .

the average OCV is calculated as 0.82 V vs. Li/Li^+ , whereas Ti_2NS_2 shows several steps in intercalation potential and the average OCV comes out to be 0.64 V vs. Li/Li^+ . In the Na-ion case, the two end structures are described as $\text{V}_2\text{NS}_2 \leftrightarrow \text{Na}_{0.78}\text{V}_2\text{NS}_2$, and $\text{Ti}_2\text{NS}_2 \leftrightarrow \text{Na}_{0.67}\text{Ti}_2\text{NS}_2$, respectively. All

the phases between the two end compounds are stable and average OCVs are computed as 0.53 V for Na/Na⁺ in V₂NS₂ and 0.83 V for Na/Na⁺ in Ti₂NS₂ host. For better understanding, the comparison of results in both surfaces for Li and Na case are summarized in Table 5.2. OCVs for these two hosts are higher than most of the 2D materials, but higher concentration of ion intercalation yields the good theoretical specific capacities. V₂NS₂ surface shows the specific capacity of 300 mAh/g for Li-ion and 99.8 mAh/g for Na-ion. Additionally, Ti₂NS₂ yields the specific capacity as 308 mAh/g for Li-ion and 85 mAh/g for Na-ion. Further, diffusion barriers on these two surfaces are described in Table 5.2 for both the Li and Na in case, which yields a fast kinetic process. Detailed discussions of minimum energy pathways are given in Paper IX in this thesis.

Part III:
Final Remarks

6. Summary and Outlook

Design and development of new materials are the intrinsic part of the technological advancements. Understanding and improving material properties for electronic and energy applications is a cornerstone of human civilization in digital era. Along with the advancement in technology, the critical requirement of the present and the future civilization is the new sources and storage methods for energy. As of now, the silicon-based technology is reaching its miniaturization limit, while the materials are required to fill this gap. The nanoscale-structured materials are one of the base points in this research. In particular, the central topic of this thesis is 2D materials studied from theoretical perspective. Electronic structure along with the potential applications are discussed for newly synthesized and predicated 2D materials, varying from nanoscale electronic devices to rechargeable batteries.

In recent years, there has been a continuous progress in constructing the heterostructures of 2D materials either in vertical or in lateral dimension and tune the electronic properties suitable to the desired applications. An example of vertical heterostructure is van der Waals (vdW) bonded heterostructure that have been used for the experimental realization of field effect transistor, rectifier and photodiode during last decade. Lateral heterostructures perform as electrodes when arranged as nanogap or nanopore. With a suitable choice of materials, we have studied all these setups in this thesis.

It is essential to put forward the experimental efforts with these materials for different applications, but to perform the experiments, one needs enough resources and workforce. In many occasions, the density functional theory (DFT) supported the experimental finding very well, as well as in some cases the theoretical prediction was made much before the experimental realization happened. Modern-day DFT has proven to be an essential tool in describing and understanding the materials properties and also their applications. This thesis discussed the DFT and Non-equilibrium Green's function (NEGF) formalism and computational methods, which have been used to perform all the theoretical work presented in this thesis.

The prototype 2D material is graphene, which has been extensively discussed and much more explored as compared to the other 2D materials. It has been utilized as an ultrathin electrode for nanoelectronics and single molecular devices. Graphene nanogap and nanopore have been proved to be an attractive setup for DNA sequencing, but the fundamental problem of the reactivity of the graphene edge is unsolved. In particular, graphene edge can be decorated with hexagonal boron nitride. In the first work of this thesis,

graphene-hBN lateral heterostructure forming nanogap has been used into sequencing the single-stranded DNA. The sensitivity in the setup demonstrated to be lower than the pristine graphene, however, the lower edge reactivity suggests that this can be a potential setup for future DNA sequencing. The success of graphene has been followed by other contemporary 2D materials exfoliated from the bulk counterpart in the form of layered structures. These 2D materials exhibit remarkable electronic and physical properties and have been investigated for the range of applications in electronics and energy storage. In this quest, several other synthetic layered materials are also synthesized from precursor unlike the layer-derived 2D materials: silicene, stanene, tellurene, etc. Recently, the lightest 2D material, 2D boron monolayer has been synthesized in different polymorphic forms. In this thesis, we have explored structural, electronic and transport properties of the different polymorph of 2D borons known as borophenes. We have also reported the tunable strain anisotropy in the two different polymorphs, β_{12} -borophene and χ -borophene. Additionally, the electronic structure and transport properties of corrugated borophene are also addressed, and its applicability as potential gas sensing application is explored. Besides applying strain, doping is a conventional method of tuning material's properties. We explore silicon and sulphur doped black phosphorus (BP), that shows metallic characteristics in electronic structure and transport properties. Considering the metallic nature, the gas sensing application has been investigated in these doped-BP sheets.

In the 90° twisted bilayer form, the intrinsic anisotropy of the BP disappears because of the degeneracy in the valence band maximum. However, when it has been used in the nanojunction setup made of the twisted bilayer, it shows the current rectifying properties, which is originated from the intrinsic anisotropy of the BP layer. Furthermore, this rectifying behavior can be tuned with the associated gate voltage.

The last part of the thesis is dedicated to the energy storage applications of different 2D materials. Presently nearly one-third of the energy storage market is occupied by the Li-ion batteries, ranging from a cell phone in our pocket to household electronic devices. To deliver higher power with enhanced stability and safety, new materials are required to replace the traditional electrode in Li-ion batteries, and 2D materials show the great promise to deal with these high demands. DFT framework has been applied to investigate the ionic insertion reaction and ionic diffusion mechanism in the 2D host compounds. Specific capacity, stability and ion intercalation kinetics of selected 2D materials are explored from the application perspective for battery operation.

A recently predicted material is Si_2BN , where Si atom is in electron deficient state. In contrast to pristine silicene, which is naturally buckled, Si_2BN is planar. Si_2BN delivered relatively high specific capacity in comparison to most of the 2D anode materials. Nevertheless, an exciting transition from planar to a buckled structure occurs upon insertion of more than one Li and Na ions per formula unit. Subsequently, this transition in the structure is corre-

lated with a higher specific capacity, which is significantly superior to several other 2D analogs. Moreover, the substrate Si_2BN retrieves the planar structure on succeeding desorption of ions and stability of the material remains intact.

Two different hydrogenated 2D boron polymorphs have been explored for the potential application in rechargeable battery. From all the obtained results, it is argued that borophane (B_2H_2) could be a potentially useful anode material both for Li and Na-ion batteries with a relatively high specific capacity. On the other hand, BH (boron hydride) has delivered remarkably higher specific capacity than the B_2H_2 for Li-ion case.

Two different sulfur functionalized Mxenes, V_2NS_2 and Ti_2NS_2 have been studied with the focus to envisage these 2D materials to be optimally functioning battery electrodes. It is found that the multilayer ion intercalation is viable, which exhibits high capacity, especially for Li-ion case. Further, the faster kinetics for battery operation has been shown with lower barrier heights of the ionic diffusion. In contradiction to various other recent 2D materials, especially the elemental ones such as silicene, phosphorene, borophene, or even graphene, that have been extensively explored for electrode applications, Mxenes can be a new paradigm, where the ion intercalation in a multilayer fashion and ultrafast diffusion suggests exciting possibilities. All these unique characteristics enable these Mxenes to be potential anode materials and likely to attract immediate attention.

6.1 Future prospects

The techniques which have been used to produce the results in this thesis will prove to be useful to investigate different kind of nanoscale device applications and electronic properties of the materials. The world of 2D materials is full of opportunities, and only graphene has shown the tremendous possibilities for application in different fields. Apart from graphene, there are almost 40 different possible transition metal dichalcogenides (TMDCs) and more than 100 possible structure of Mxene. There is extensive research also going on to synthesize the several 2D materials using synthetic methods like stanene, silicene, germanene, borophene, bismuthene, Si_2BN and so on. Using lateral and vertical heterostructure of same or different 2D materials opens the new door of possibilities for exploring new 2D materials with a range of physical and chemical properties. To design a successful 2D material heterostructures, understanding the structural and electronic properties of interfaces between those 2D materials plays a significant role. The electronic properties of heterostructure can be further tuned by the relative rotation of the layer on the surface, external strain and vertical electric field. Looking at electronic transport and optical properties of these heterostructures would be quite interesting from future aspects.

The field of nanoscale molecular electronics has emerged rapidly, which aims to utilize individual molecules as the building blocks for electronic devices. This may improve the functionality and enable the scientific community to achieve an extreme level of device miniaturization and control. The central hindrance in the progress of this field is the inadequacy in stable contacts between the molecules and metal electrodes used that can both function at room temperature and provide reproducible results. Gold has been the preferred material for making nanoscale spaced electrode for the model experiments, but these electrodes are unstable at the room temperature, which results in poor reproducibility and does not allow the spin injection. Graphene, on the other hand, possesses not only outstanding mechanical stability but also exceptionally high thermal and electronic conductive properties. These properties make graphene very attractive for a range of possible applications in molecular electronics. Furthermore, one can functionalize the chemical contact of the molecule to graphene-based materials, which can be further useful in switching the rectifying behavior of a single molecular device by changing the chemical contact of the molecule. Theoretical tools such as DFT and NEGF can be helpful to understand the properties the electrode after functionalization and it is possible to perform the electron transport calculation, which can give a direct insight of the behavior of the electrical current in the molecular scale device. It will be interesting to see, how does the rectifying property of a standard rectifying molecule with graphene electrodes and different coupling moieties behave. Additionally, edge reactivity issues of the graphene have been already discussed for the nanogap and nanopore cases in DNA sequencing devices. Nowadays, it is possible to fold graphene controllably. One can use these two ideas and use bilayer folded graphene nanogap to detect the DNA molecule and for other applications. This will be interesting to see how the folded edge of graphene reacts with the DNA molecule and up to which extent it can identify the different DNA molecules.

7. Svensk sammanfattning

Utformning och utveckling av nya material är den grundläggande delen av teknologiska framsteg. Att förstå och förbättra materialens egenskaper för användning inom elektronik och energi är en hörnsten för den mänskliga civilisationen i den digitala eran. Vid sidan av framsteg inom teknologin, är nya energikällor och metoder för att lagra energi en nödvändighet för nuvarande och kommande generationer.

Den kiselbaserade teknologin har redan nått sin nedre storleksgräns, så det krävs nya material för att fylla gapet. Materialstrukturer på nanonivå är i fokus i den här forskningen. Speciellt är dem 2D-material studerade från ett teoretiskt perspektiv som tar den centrala delen i den här avhandlingen. Elektronisk struktur tillsammans med möjliga användningsområdena diskuteras för nyligen syntetiserade eller förutsagda 2D-material, vilka användningsområdena varierar från elektroniska komponenter på nanonivå till uppladdningsbara batterier.

På senare år har det blivit möjligt att framställa heterostrukturer ifrån 2D-material både i lodrät samt sidoställda och manipulera deras egenskaper, för att anpassa till valfritt användningsområde. T.ex. har vi lodrätta strukturer som under det senaste årtiondet har använts i field effect transistor (FET), likriktare och fotodioder. Sidoställda strukturer används som elektroder utformade som nanogap eller nanopor. Materialer anpassade för alla dessa system studeras i den här avhandlingen.

Det är nödvändigt att framhålla den experimentella insatsen med de här 2D-materialen, men för att bedriva experiment behöver man tillräckligt med resurser och arbetskraft. I många tillfällen överensstämde densitetsfunktionalteorin (DFT) väl med experimentella resultat, i andra gjordes den teoretiska förutsägelsen innan det experimentella förverkligandet gjordes. Det har visat sig att dagens DFT är ett viktigt verktyg för att beskriva och förstå materialens egenskaper och i vissa fall även deras användningsområden. I det andra kapitlet i den här avhandlingen diskuteras DFT och Non-equilibrium Green's function (NEGF)-metoden, vilka har använts för att göra allt teoretiskt arbete i den här avhandlingen.

Grafen är prototypen för 2D-material. Den hade omfattande diskuterats och undersökts mer än alla andra 2D-material. Den har använts som en ultratunn elektrod i nanoelektronik och för en-molekylskonstruktioner. Grafen-nanogap och -nanopor har visat sig vara lysande system för DNA-sekvensering, men det grundläggande problemet med de reaktiva grafenkanterna är olöst. Grafenkanterna kan i det här fallet kläs i hexagonalt bornitrat (hBN). I den första artikeln i den här avhandlingen har grafen-hBN, som bildar ett nanogap, använts

för att sekvensera en-strängs-DNA. Känsligheten hos systemet visar sig vara lägre än hos rent grafen, dock gör den lägre kantreaktiviteten systemet till en lovande kandidat för framtida DNA-sekvenseringar.

Succén hos grafen uppföljdes av andra moderna 2D-material, som framställdes från lager av motsvarande bulkmaterial. De här 2D-materialen visar enastående elektroniska och fysikaliska egenskaper och har undersökts för många olika användningsområden inom elektronik och energilagring. I sökandet har även andra, syntetiska material syntetiserats från sina föregångsmaterial, de olika lagerframställda 2D-materialen: silicen, stanen, telluren, etc. Nyligen syntetiserades det lättaste 2D-materialet - 2D-bor i olika polymorfiska former. In den här avhandlingen utforskade vi strukturer, elektroniska- och transportegenskaper hos olika polymorfiska former av 2D-bor s.k. borofen. Vi visar också justerbar anisotropi i två polymorfiska former, β_{12} -borofen och χ -borofen med hjälp av sträckning. Dessutom har elektronisk struktur och transportegenskaper hos vågig borofen tagits upp och dess lämplighet som en möjlig gassensor har undersökts. Förutom sträckning är dopning en av etablerade metoder för att ändra på ett materials egenskaper. Vi undersöker Si-dopad svart forsfor (SF), som har endimensionell, metallisk, trådliknande karakteristik i elektronstruktur och transportegenskaper. S-dopad SF beter sig också som en metall i elektronisk struktur och transportegenskaper, det visar en skarp topp i övergångsdiagrammet. P.g.a. sin metalliska karaktär undersöktes det dopade SF-monolagret med avseende på gassensorstillämpningar.

I den 90°vridna formen försvinner den inre anisotropin i SF p.g.a. degenera-tion i valensbandsmaximumet. När den användes i en nanoelektronikkoppling, kunde man se korregerande strömmar som kommer från den inre anisotropin i den vridna formen av SF. Vidare kan detta beteende hos kopplingen justeras med spänning från grindelektroden.

Den sista delen i den här avhandlingen är avsatt för energilagringstillämpningar av olika 2D-material. Nu för tiden är nära en tredjedel energilagring-smarknaden mättad av Li-jonbatterier, där användning sträcker sig från mobiltelefoner i våra fickor till elektroniska hushållsapparater. För att kunna leverera högeffektiv elkraftförsörjning med ökad stabilitet och säkerhet, måste nya material användas för att ersätta den traditionella elektroden i Li-jonbatterier och 2D-material visar sig lovande för de här höga kraven. DFT-ramverket har använts för att undersöka joninsättningsreaktionen och jondiffusionsmekanis-men i 2D-värdöreningarna. Specifik kapacitet, stabilitet och joninskjutsning-skinetik hos utvalda 2D-material har undersökts med fokus på batterifunktionstillämpningar. Ett nyligen beräknat material är Si_2BN , där Si-atomen saknar några elektroner. Si_2BN levererade relativt hög specifik kapacitet jämfört med de flesta 2D-anodmaterialen. Dessutom sker en spännande övergång från plan till vågig struktur med mer än en Li- och Na-jon per formelenhet. Den här ändringen i strukturen hänger samman med en högre specifik kapacitet, vilken är märkbart överlägsen flertal andra 2D-analogier. Dessutom återfår substratet Si_2BN plan struktur vid lyckad borttagning av joner och stabiliteten av mate-

rialet förblir intakt.

Två olika vätegenererade 2D-borpolymorfer har undersökts för en möjlig tillämpning inom uppladdningsbara batterier. Från alla uppmätta resultat talade det för, att B_2H_2 skulle kunna vara ett användbart anodmaterial både för Li- och Na-jonbatterier med relativt hög specifik kapacitet. Å andra sidan levererade BH (borhydrid) anmärkningsvärt högre specifik kapacitet än B_2H_2 i Li-jon fallet.

Två olika svavelfunktionaliserade mxener, V_2NS_2 och Ti_2NS_2 , har studerats med fokus på att simulera meningsfulla markörer för att bedöma om dessa 2D-material kan vara optimalt fungerande batterielektroder. Det upptäcktes att multilagersjoninskjutning är möjlig, vilket visar en hög kapacitet, särskilt i Li-jon fallet. Vidare har snabbare batterifunktionskinetik visats med lägre barriärer för jondiffusionen. I skillnad till många andra nya 2D-material, speciellt elementära så som silicen, forforen, borofen eller även grafen som har studerats omfattande, kan mxener vara ett nytt paradigm, där joninskjutningen på ett multilagerssätt och ultrasnabb diffusion medför spännande möjligheter. Alla de här unika dragen meriterar dessa mxener till att vara möjliga anodmaterial och troliga att få omedelbart uppmärksamhet.

8. Acknowledgments

I am immensely obliged to a large number of people for making journey as a Doctoral student at Uppsala University exhilarating one. All of them deserve my devoted acknowledgment, and I proved my best to list all of them here. However, It may be possible that I might have dropped some of them, unwittingly, I beg for their forgiveness. It is because of the colleagues in Materials theory division and the group members, I have been able to do research and complete my thesis in a relaxed environment. I would also like to give a special thanks to the funding agency *Erasmus Mundus* for providing me *NAMASTE* scholarship to come here in Sweden for Doctoral studies.

Prof. Rajeev Ahuja, who provided me opportunity to work here as a Doctoral student in materials theory division, and helped me throughout my stay both educationally and mentally. I am most obliged to him for his supervision, encouragement, constructive discussions, suggestions, patience, and invaluable support, which made this work possible. I am indebted to Dr. Anton Grigoriev (Co-supervisor) for teaching me density function theory and electron transport calculation, helping me throughout my doctoral work, listening ideas (sometimes nonsense) and patiently making me correct. I also owe a significant portion of my acknowledgment to co-supervisor Dr. Sudip Chakarborty and Dr. Naresh Jena for helping me and giving me new ideas to work. I would convey my overwhelming thanks to the administration of our department, they always manage an excellent working environment and ready to support. Thanks to Ritwik, Rafael, Pablo, Vancho, Iulia, Marco, Soumyajyoti, Swarup, Ehsan, Rudra, Ashish, Sangeeta, Pralay and Ishtiaq, who were always open for discussions during this work. It is worth mentioning the name of Ritwik, Soumyajyoti for their help in correcting this thesis and cover page, John for Swedish summary and Devendra, Deobrat, Non, Rafael, Rubab, Priyam, Arnab, Rahul, Nishant and Naresh for the proofreading and making this thesis readable.

Special thanks to my friends here from India, who always made me comfortable and made an environment like a home away from home. Manvi and Ankit, Naresh and Bani made me feel like family here in Uppsala. I want to convey my special thanks to Ritwik for being such a nice friend and running partner during most the running sessions and Soumyajyoti for being a captain of the running team, which also includes Somnath, Pralay and Devendra, with whom I ran three half marathons. You guys were amazing throughout and I think we did well in the last three years. My heartiest gratitude to Devendra, Sangeeta (Annapurna Devi), Soham, Nishant, Rudra, Ritwik, Amitava,

Soumyajyoti, Somnath, Sudip, Ravi, Deep, Rahul, Deobrat and Swarup for being such a fantastic family, organizing nice trips, nightouts and immediate dinner plans and awesome parties.

It is also an excellent opportunity to acknowledge my friends staying in India, Pankaj and Shailendra, the friends with whom I shared childhood dreams and struggles. Shikha and Ravi for being such great support and Ritu for being the closest friend for six-years and helping through the even and odds of life and PhD studies.

The family comes in the last, but they have been in my life since the beginning. I do not have words to express my gratitude towards my grandparents, parents, and siblings for their unconditional love, support, encouragement, and blessings. Whoever I am and I will be, is only because of the sacrifices they have made, their blessings and motivation.

References

- [1] R. Peierls, *Annales de l'institut Henri Poincaré* **5**, 177 (1935).
- [2] L. Landau, *Phys. Z. Sowjetunion* **11**, 26 (1937).
- [3] L. D. Landau, E. M. Lifshitz, L. P. Pitaevskii, J. B. Sykes, and M. J. Kearsley, *Statistical physics. Volume 5 of Course of theoretical physics. Part 1*, third edition, revised and enlarged / by e.m. lifshitz and l.p. pitaevskii ed. (Oxford, England Pergamon Press, 1980).
- [4] R. Peierls, *Helv. Phys. Acta* **7**, 158 (1934).
- [5] N. D. Mermin, *Phys. Rev.* **176**, 250 (1968).
- [6] J. Evans, P. Thiel, and M. Bartelt, *Surface Science Reports* **61**, 1 (2006).
- [7] J. A. Venables, G. D. T. Spiller, and M. Hanbucken, *Reports on Progress in Physics* **47**, 399 (1984).
- [8] K. S. Novoselov, A. K. Geim, S. V. Morozov, D. Jiang, Y. Zhang, S. V. Dubonos, I. V. Grigorieva, and A. A. Firsov, *Science* **306**, 666 (2004).
- [9] C. Oshima, A. Itoh, E. Rokuta, T. Tanaka, K. Yamashita, and T. Sakurai, *Solid State Communications* **116**, 37 (2000).
- [10] I. Forbeaux, J.-M. Themlin, and J.-M. Debever, *Phys. Rev. B* **58**, 16396 (1998).
- [11] A. V. Bommel, J. Crombeen, and A. V. Tooren, *Surface Science* **48**, 463 (1975).
- [12] H. P. Boehm, A. Clauss, G. O. Fischer, and U. Hofmann, *Zeitschrift für anorganische und allgemeine Chemie* **316**, 119 (1962).
- [13] A. Carvalho, M. Wang, X. Zhu, A. S. Rodin, H. Su, and A. H. Castro Neto, *Nature Reviews Materials* **1** (2016).
- [14] Y.-C. Lin, H.-P. Komsa, C.-H. Yeh, T. Björkman, Z.-Y. Liang, C.-H. Ho, Y.-S. Huang, P.-W. Chiu, A. V. Krasheninnikov, and K. Suenaga, *ACS Nano* **9**, 11249 (2015).
- [15] K. F. Mak, C. Lee, J. Hone, J. Shan, and T. F. Heinz, *Phys. Rev. Lett.* **105**, 136805 (2010).
- [16] C. Tan and H. Zhang, *Chem. Soc. Rev.* **44**, 2713 (2015).
- [17] C. R. Dean, A. F. Young, I. Meric, C. Lee, L. Wang, S. Sorgenfrei, K. Watanabe, T. Taniguchi, P. Kim, K. L. Shepard, and J. Hone, *Nature Nanotechnology* **5**, 722 (2010).
- [18] B. Anasori, M. R. Lukatskaya, and Y. Gogotsi, *Nature Reviews Materials* **2**, 16098 (2017).
- [19] M. Naguib, V. N. Mochalin, M. W. Barsoum, and Y. Gogotsi, *Advanced Materials* **26**, 992 (2014).
- [20] L. Kou, C. Chen, and S. C. Smith, *The Journal of Physical Chemistry Letters* **6**, 2794 (2015).
- [21] D. Çakır, C. Sevik, and F. M. Peeters, *Phys. Rev. B* **92**, 165406 (2015).
- [22] P. Vogt, P. De Padova, C. Quaresima, J. Avila, E. Frantzeskakis, M. C. Asensio, A. Resta, B. Ealet, and G. Le Lay, *Phys. Rev. Lett.* **108**, 155501 (2012).

- [23] M. E. Dávila, L. Xian, S. Cahangirov, A. Rubio, and G. L. Lay, *New Journal of Physics* **16**, 095002 (2014).
- [24] F. Reis, G. Li, L. Dudy, M. Bauernfeind, S. Glass, W. Hanke, R. Thomale, J. Schäfer, and R. Claessen, *Science* **357**, 287 (2017).
- [25] F.-f. Zhu, W.-j. Chen, Y. Xu, C.-l. Gao, D.-d. Guan, C.-h. Liu, D. Qian, S.-C. Zhang, and J.-f. Jia, *Nature Materials* **14**, 1020 (2015).
- [26] Z. Zhu, X. Cai, S. Yi, J. Chen, Y. Dai, C. Niu, Z. Guo, M. Xie, F. Liu, J.-H. Cho, Y. Jia, and Z. Zhang, *Phys. Rev. Lett.* **119**, 106101 (2017).
- [27] A. J. Mannix, X.-F. Zhou, B. Kiraly, J. D. Wood, D. Alducin, B. D. Myers, X. Liu, B. L. Fisher, U. Santiago, J. R. Guest, M. J. Yacaman, A. Ponce, A. R. Oganov, M. C. Hersam, and N. P. Guisinger, *Science* **350**, 1513 (2015).
- [28] B. Feng, J. Zhang, Q. Zhong, W. Li, S. Li, H. Li, P. Cheng, S. Meng, L. Chen, and K. Wu, *Nature Chemistry* **8**, 563 (2016).
- [29] A. N. Andriotis, E. Richter, and M. Menon, *Phys. Rev. B* **93**, 081413 (2016).
- [30] C. Zhang and Q. Sun, *The Journal of Physical Chemistry Letters* **7**, 2664 (2016).
- [31] G. R. Bhimanapati, Z. Lin, V. Meunier, Y. Jung, J. Cha, S. Das, D. Xiao, Y. Son, M. S. Strano, V. R. Cooper, L. Liang, S. G. Louie, E. Ringe, W. Zhou, S. S. Kim, R. R. Naik, B. G. Sumpter, H. Terrones, F. Xia, Y. Wang, J. Zhu, D. Akinwande, N. Alem, J. A. Schuller, R. E. Schaak, M. Terrones, and J. A. Robinson, *ACS Nano* **9**, 11509 (2015).
- [32] J. Hassoun, F. Bonaccorso, M. Agostini, M. Angelucci, M. G. Betti, R. Cingolani, M. Gemmi, C. Mariani, S. Panero, V. Pellegrini, and B. Scrosati, *Nano Letters* **14**, 4901 (2014).
- [33] D. Akinwande, C. J. Brennan, J. S. Bunch, P. Egberts, J. R. Felts, H. Gao, R. Huang, J.-S. Kim, T. Li, Y. Li, K. M. Liechti, N. Lu, H. S. Park, E. J. Reed, P. Wang, B. I. Yakobson, T. Zhang, Y.-W. Zhang, Y. Zhou, and Y. Zhu, *Extreme Mechanics Letters* **13**, 42 (2017).
- [34] Z. Yang, J. Dou, and M. Wang, in *Two-dimensional Materials for Photodetector* (InTech, 2018).
- [35] S. Gupta, S. N. Shirodkar, A. Kutana, and B. I. Yakobson, *ACS Nano* **12**, 10880 (2018).
- [36] K. Bernstein, D. J. Frank, A. E. Gattiker, W. Haensch, B. L. Ji, S. R. Nassif, E. J. Nowak, D. J. Pearson, and N. J. Rohrer, *IBM Journal of Research and Development* **50**, 433 (2006).
- [37] S. Saxena, C. Hess, H. Karbasi, A. Rossoni, S. Tonello, P. McNamara, S. Lucherini, S. Minehane, C. Dolainsky, and M. Quarantelli, *IEEE Transactions on Electron Devices* **55**, 131 (2008).
- [38] G. E. Moore, *IEEE Solid-State Circuits Society Newsletter* **11**, 33 (2006).
- [39] L. Liu, S. B. Kumar, Y. Ouyang, and J. Guo, *IEEE Transactions on Electron Devices* **58**, 3042 (2011).
- [40] Y. Yoon, K. Ganapathi, and S. Salahuddin, *Nano Letters* **11**, 3768 (2011).
- [41] R. A. Street, *Advanced Materials* **21**, 2007 (2009).
- [42] I. Meric, M. Y. Han, A. F. Young, B. Ozyilmaz, P. Kim, and K. L. Shepard, *Nature Nanotechnology* **3**, 654 (2008).
- [43] K. Bolotin, K. Sikes, Z. Jiang, M. Klima, G. Fudenberg, J. Hone, P. Kim, and H. Stormer, *Solid State Communications* **146**, 351 (2008).

- [44] K. S. Novoselov, A. K. Geim, S. V. Morozov, D. Jiang, M. I. Katsnelson, I. V. Grigorieva, S. V. Dubonos, and A. A. Firsov, *Nature* **438**, 197 (2005).
- [45] E. H. Hwang, S. Adam, and S. D. Sarma, *Phys. Rev. Lett.* **98**, 186806 (2007).
- [46] Y.-W. Tan, Y. Zhang, K. Bolotin, Y. Zhao, S. Adam, E. H. Hwang, S. Das Sarma, H. L. Stormer, and P. Kim, *Phys. Rev. Lett.* **99**, 246803 (2007).
- [47] Q. H. Wang, K. Kalantar-Zadeh, A. Kis, J. N. Coleman, and M. S. Strano, *Nature Nanotechnology* **7**, 699 (2012).
- [48] W. Choi, N. Choudhary, G. H. Han, J. Park, D. Akinwande, and Y. H. Lee, *Materials Today* **20**, 116 (2017).
- [49] B. Radisavljevic, A. Radenovic, J. Brivio, V. Giacometti, and A. Kis, *Nature Nanotechnology* **6**, 147 (2011).
- [50] B. Radisavljevic and A. Kis, *Nature Materials* **12**, 815 (2013).
- [51] A. Splendiani, L. Sun, Y. Zhang, T. Li, J. Kim, C.-Y. Chim, G. Galli, and F. Wang, *Nano Letters* **10**, 1271 (2010).
- [52] O. Lopez-Sanchez, D. Lembke, M. Kayci, A. Radenovic, and A. Kis, *Nature Nanotechnology* **8**, 497 (2013).
- [53] M. W. Iqbal, M. Z. Iqbal, M. F. Khan, M. A. Shehzad, Y. Seo, J. H. Park, C. Hwang, and J. Eom, *Scientific Reports* **5**, 10699 (2015).
- [54] S. R. Das, J. Kwon, A. Prakash, C. J. Delker, S. Das, and D. B. Janes, *Applied Physics Letters* **106**, 083507 (2015).
- [55] L. Li, Y. Yu, G. J. Ye, Q. Ge, X. Ou, H. Wu, D. Feng, X. H. Chen, and Y. Zhang, *Nature Nanotechnology* **9**, 372 (2014).
- [56] F. Prins, A. Barreiro, J. W. Ruitenbergh, J. S. Seldenthuis, N. Aliaga-Alcalde, L. M. K. Vandersypen, and H. S. J. van der Zant, *Nano Letters* **11**, 4607 (2011).
- [57] C. Nef, L. Pósa, P. Makk, W. Fu, A. Halbritter, C. Schönenberger, and M. Calame, *Nanoscale* **6**, 7249 (2014).
- [58] H. M. Wang, Z. Zheng, Y. Y. Wang, J. J. Qiu, Z. B. Guo, Z. X. Shen, and T. Yu, *Applied Physics Letters* **96**, 023106 (2010).
- [59] J. Prasongkit, A. Grigoriev, B. Pathak, R. Ahuja, and R. H. Scheicher, *Nano Letters* **11**, 1941 (2011).
- [60] J. Prasongkit, A. Grigoriev, B. Pathak, R. Ahuja, and R. H. Scheicher, *The Journal of Physical Chemistry C* **117**, 15421 (2013).
- [61] H. W. C. Postma, *Nano Letters* **10**, 420 (2010).
- [62] D. Cohen-Tanugi and J. C. Grossman, *Nano Letters* **12**, 3602 (2012).
- [63] C. A. Merchant, K. Healy, M. Wanunu, V. Ray, N. Peterman, J. Bartel, M. D. Fischbein, K. Venta, Z. Luo, A. T. C. Johnson, and M. Drndic, *Nano Letters* **10**, 2915 (2010).
- [64] S. Garaj, W. Hubbard, A. Reina, J. Kong, D. Branton, and J. A. Golovchenko, *Nature* **467**, 190 (2010).
- [65] G. F. Schneider, S. W. Kowalczyk, V. E. Calado, G. Pandraud, H. W. Zandbergen, L. M. K. Vandersypen, and C. Dekker, *Nano Letters* **10**, 3163 (2010).
- [66] A. B. Farimani, K. Min, and N. R. Aluru, *ACS Nano* **8**, 7914 (2014).
- [67] M. Heiranian, A. B. Farimani, and N. R. Aluru, *Nature Communications* **6**, 8616 (2015).

- [68] R. L. Kumawat, P. Garg, S. Kumar, and B. Pathak, *ACS Applied Materials & Interfaces* (2018).
- [69] A. K. Geim and I. V. Grigorieva, *Nature* **499**, 419 (2013).
- [70] J. E. Padilha, A. Fazzio, and A. J. R. da Silva, *Phys. Rev. Lett.* **114**, 066803 (2015).
- [71] R. B. Pontes, R. H. Miwa, A. J. R. da Silva, A. Fazzio, and J. E. Padilha, *Phys. Rev. B* **97**, 235419 (2018).
- [72] M. Z. Iqbal, S. Siddique, M. F. Khan, A. u. Rehman, A. Rehman, and J. Eom, *Advanced Engineering Materials* **20**, 1800159 (2018).
- [73] D. Pierucci, H. Henck, J. Avila, A. Balan, C. H. Naylor, G. Patriarche, Y. J. Dappe, M. G. Silly, F. Sirotti, A. T. C. Johnson, M. C. Asensio, and A. Ouerghi, *Nano Letters* **16**, 4054 (2016).
- [74] H.-P. Komsa and A. V. Krashennnikov, *Phys. Rev. B* **88**, 085318 (2013).
- [75] M. A. Khan, S. Rath, C. Lee, Y. Kim, H. Kim, D. Whang, S. J. Yun, D.-H. Youn, K. Watanabe, T. Taniguchi, and G.-H. Kim, *Nanotechnology* **29**, 395201 (2018).
- [76] C. Jin, J. Kim, J. Suh, Z. Shi, B. Chen, X. Fan, M. Kam, K. Watanabe, T. Taniguchi, S. Tongay, A. Zettl, J. Wu, and F. Wang, *Nature Physics* **13**, 127 (2016).
- [77] C.-H. Lee, G.-H. Lee, A. M. van der Zande, W. Chen, Y. Li, M. Han, X. Cui, G. Arefe, C. Nuckolls, T. F. Heinz, J. Guo, J. Hone, and P. Kim, *Nature Nanotechnology* **9**, 676 (2014).
- [78] M. P. Levendorf, C.-J. Kim, L. Brown, P. Y. Huang, R. W. Havener, D. A. Muller, and J. Park, *Nature* **488**, 627 (2012).
- [79] S. Yang, C. Jiang, and S.-h. Wei, *Applied Physics Reviews* **4**, 021304 (2017).
- [80] P. Bonato, *IEEE Engineering in Medicine and Biology Magazine* **29**, 25 (2010).
- [81] C. Narayanaswami, N. Kamijoh, M. Raghunath, T. Inoue, T. Cipolla, J. Sanford, E. Schlig, S. Venkiteswaran, D. Guniguntala, V. Kulkarni, and K. Yamazaki, *Computer* **35**, 33 (2002).
- [82] R. Want, B. N. Schilit, and S. Jenson, *Computer* **48**, 28 (2015).
- [83] V. Etacheri, R. Marom, R. Elazari, G. Salitra, and D. Aurbach, *Energy Environ. Sci.* **4**, 3243 (2011).
- [84] S. Goriparti, E. Miele, F. D. Angelis, E. D. Fabrizio, R. P. Zaccaria, and C. Capiglia, *Journal of Power Sources* **257**, 421 (2014).
- [85] L. Li, Y. Zheng, S. Zhang, J. Yang, Z. Shao, and Z. Guo, *Energy Environ. Sci.* **11**, 2310 (2018).
- [86] G. E. Blomgren, *Journal of The Electrochemical Society* **164**, A5019 (2017).
- [87] P. Ge and M. Foulletier, *Solid State Ionics* **28-30**, 1172 (1988).
- [88] X. Xu, W. Liu, Y. Kim, and J. Cho, *Nano Today* **9**, 604 (2014).
- [89] K.-S. Chen, I. Balla, N. S. Luu, and M. C. Hersam, *ACS Energy Letters* **2**, 2026 (2017).
- [90] L. Shi and T. Zhao, *J. Mater. Chem. A* **5**, 3735 (2017).
- [91] D. Pan, S. Wang, B. Zhao, M. Wu, H. Zhang, Y. Wang, and Z. Jiao, *Chemistry of Materials* **21**, 3136 (2009).
- [92] C.-M. Park and H.-J. Sohn, *Advanced Materials* **19**, 2465 (2007).

- [93] J. Sun, G. Zheng, H.-W. Lee, N. Liu, H. Wang, H. Yao, W. Yang, and Y. Cui, *Nano Letters* **14**, 4573 (2014).
- [94] W. Choi, N. Choudhary, G. H. Han, J. Park, D. Akinwande, and Y. H. Lee, *Materials Today* **20**, 116 (2017).
- [95] Y. Sun, D. Chen, and Z. Liang, *Materials Today Energy* **5**, 22 (2017).
- [96] Y. Liu, K. Horikawa, M. Fujiyosi, N. Imanishi, A. Hirano, and Y. Takeda, *Electrochimica Acta* **49**, 3487 (2004).
- [97] M. Naguib, J. Come, B. Dyatkin, V. Presser, P.-L. Taberna, P. Simon, M. W. Barsoum, and Y. Gogotsi, *Electrochemistry Communications* **16**, 61 (2012).
- [98] M. Born and R. Oppenheimer, *Annalen der Physik* **389**, 457 (1927).
- [99] L. H. Thomas, in *Mathematical Proceedings of the Cambridge Philosophical Society*, Vol. 23 (Cambridge University Press, 1927).
- [100] E. H. Lieb and B. Simon, *Phys. Rev. Lett.* **31**, 681 (1973).
- [101] P. Hohenberg and W. Kohn, *Phys. Rev.* **136**, B864 (1964).
- [102] R. M. Martin, *Electronic structure: basic theory and practical methods* (Cambridge university press, 2004).
- [103] D. Sholl and J. A. Steckel, *Density functional theory: a practical introduction* (John Wiley & Sons, 2011).
- [104] F. Jensen, *Introduction to computational chemistry* (John Wiley & sons, 2017).
- [105] W. Kohn and L. J. Sham, *Phys. Rev.* **140**, A1133 (1965).
- [106] D. M. Ceperley and B. J. Alder, *Phys. Rev. Lett.* **45**, 566 (1980).
- [107] A. Zupan, P. Blaha, K. Schwarz, and J. P. Perdew, *Phys. Rev. B* **58**, 11266 (1998).
- [108] R. O. Jones and O. Gunnarsson, *Rev. Mod. Phys.* **61**, 689 (1989).
- [109] J. C. Grossman, L. Mitas, and K. Raghavachari, *Phys. Rev. Lett.* **75**, 3870 (1995).
- [110] J. P. Perdew, J. A. Chevary, S. H. Vosko, K. A. Jackson, M. R. Pederson, D. J. Singh, and C. Fiolhais, *Phys. Rev. B* **46**, 6671 (1992).
- [111] J. P. Perdew and W. Yue, *Phys. Rev. B* **33**, 8800 (1986).
- [112] J. P. Perdew, K. Burke, and M. Ernzerhof, *Phys. Rev. Lett.* **77**, 3865 (1996).
- [113] A. D. Becke, *Phys. Rev. A* **38**, 3098 (1988).
- [114] A. D. Becke, *The Journal of Chemical Physics* **107**, 8554 (1997).
- [115] B. Hammer, M. Scheffler, K. W. Jacobsen, and J. K. Nørskov, *Phys. Rev. Lett.* **73**, 1400 (1994).
- [116] E. Penev, P. Kratzer, and M. Scheffler, *The Journal of Chemical Physics* **110**, 3986 (1999).
- [117] F. Bloch, *Zeitschrift für physik* **52**, 555 (1929).
- [118] N. W. Ashcroft and N. D. Mermin, *Solid State Physics* (Cengage Learning, 2011).
- [119] A. E. A. Fouda and N. A. Besley, *Theoretical Chemistry Accounts* **137**, 6 (2017).
- [120] J. Ihm, A. Zunger, and M. L. Cohen, *Journal of Physics C: Solid State Physics* **12**, 4409 (1979).
- [121] F. Nogueira, J. Martins, and C. Fiolhais, *The European Physical Journal D - Atomic, Molecular, Optical and Plasma Physics* **9**, 229 (1999).
- [122] W. E. Pickett, *Computer Physics Reports* **9**, 115 (1989).
- [123] G. Kresse and J. Furthmüller, *Phys. Rev. B* **54**, 11169 (1996).

- [124] P. E. Blöchl, Phys. Rev. B **50**, 17953 (1994).
- [125] P. Ordejón, E. Artacho, and J. M. Soler, Phys. Rev. B **53**, R10441 (1996).
- [126] J. C. Slater, Phys. Rev. **36**, 57 (1930).
- [127] J. VandeVondele and J. Hutter, The Journal of Chemical Physics **127**, 114105 (2007).
- [128] G. Maroulis and A. Haskopoulos, Chemical Physics Letters **349**, 335 (2001).
- [129] G. Maroulis, The Journal of Chemical Physics **108**, 5432 (1998).
- [130] Á. Ruiz-Serrano, N. D. M. Hine, and C.-K. Skylaris, The Journal of Chemical Physics **136**, 234101 (2012).
- [131] R. Landauer, Zeitschrift für Physik B Condensed Matter **68**, 217 (1987).
- [132] S. Datta, Superlattices and Microstructures **28**, 253 (2000).
- [133] S. De and J. N. Coleman, ACS Nano **4**, 2713 (2010).
- [134] K. S. Novoselov, V. I. Fal'ko, L. Colombo, P. R. Gellert, M. G. Schwab, and K. Kim, Nature **490**, 192 (2012).
- [135] V. Shukla, N. K. Jena, A. Grigoriev, and R. Ahuja, ACS Applied Materials & Interfaces **9**, 39945 (2017).
- [136] L. Esaki and R. Tsu, IBM Journal of Research and Development **14**, 61 (1970).
- [137] D. Li, M. Chen, Z. Sun, P. Yu, Z. Liu, P. M. Ajayan, and Z. Zhang, Nature Nanotechnology **12**, 901 (2017).
- [138] T. Cao, Z. Li, D. Y. Qiu, and S. G. Louie, Nano Letters **16**, 5542 (2016).
- [139] J. Xie, Q. Luo, L. Jia, Z. Y. Zhang, H. G. Shi, D. Z. Yang, and M. S. Si, EPL (Europhysics Letters) **121**, 27002 (2018).
- [140] C. Gong, Y. Zhang, W. Chen, J. Chu, T. Lei, J. Pu, L. Dai, C. Wu, Y. Cheng, T. Zhai, L. Li, and J. Xiong, Advanced Science **4**, 1700231 (2017).
- [141] J. Yin, J. Li, Y. Hang, J. Yu, G. Tai, X. Li, Z. Zhang, and W. Guo, Small **12**, 2942 (2016).
- [142] H. Tang and S. Ismail-Beigi, Phys. Rev. Lett. **99**, 115501 (2007).
- [143] Z. Zhang, E. S. Penev, and B. I. Yakobson, Nature Chemistry **8**, 525 (2016).
- [144] E. S. Penev, S. Bhowmick, A. Sadrzadeh, and B. I. Yakobson, Nano Letters **12**, 2441 (2012).
- [145] Z. Zhang, Y. Yang, G. Gao, and B. I. Yakobson, Angewandte Chemie International Edition **54**, 13022 (2015).
- [146] Y. Liu, E. S. Penev, and B. I. Yakobson, Angewandte Chemie International Edition **52**, 3156 (2013).
- [147] X.-F. Zhou, X. Dong, A. R. Oganov, Q. Zhu, Y. Tian, and H.-T. Wang, Phys. Rev. Lett. **112**, 085502 (2014).
- [148] Z. Zhang, E. S. Penev, and B. I. Yakobson, Chem. Soc. Rev. **46**, 6746 (2017).
- [149] L. Li, Y. Yu, G. J. Ye, Q. Ge, X. Ou, H. Wu, D. Feng, X. H. Chen, and Y. Zhang, Nature Nanotechnology **9**, 372 (2014).
- [150] C. Guo, L. Wang, H. Xing, and X. Chen, Journal of Applied Physics **120**, 215701 (2016).
- [151] Y. Du, H. Liu, Y. Deng, and P. D. Ye, ACS Nano **8**, 10035 (2014).
- [152] H. Jiang, Z. Lu, M. Wu, F. Ciucci, and T. Zhao, Nano Energy **23**, 97 (2016).
- [153] P. Liang, Y. Cao, B. Tai, L. Zhang, H. Shu, F. Li, D. Chao, and X. Du, Journal of Alloys and Compounds **704**, 152 (2017).
- [154] J. Liu, C. Zhang, L. Xu, and S. Ju, RSC Adv. **8**, 17773 (2018).

- [155] Y. Zhang, Z.-F. Wu, P.-F. Gao, S.-L. Zhang, and Y.-H. Wen, *ACS Applied Materials & Interfaces* **8**, 22175 (2016).
- [156] L. Li, H. Zhang, and X. Cheng, *Computational Materials Science* **137**, 119 (2017).
- [157] L.-C. Xu, A. Du, and L. Kou, *Phys. Chem. Chem. Phys.* **18**, 27284 (2016).
- [158] J. E. Padilha, R. H. Miwa, and A. Fazio, *Phys. Chem. Chem. Phys.* **18**, 25491 (2016).
- [159] O. Leenaerts, B. Partoens, and F. M. Peeters, *Phys. Rev. B* **77**, 125416 (2008).
- [160] A. Shokri and N. Salami, *Sensors and Actuators B: Chemical* **236**, 378 (2016).
- [161] J. wen Feng, Y. jie Liu, H. xia Wang, J. xiang Zhao, Q. hai Cai, and X. zhang Wang, *Computational Materials Science* **87**, 218 (2014).
- [162] W. Xia, W. Hu, Z. Li, and J. Yang, *Phys. Chem. Chem. Phys.* **16**, 22495 (2014).
- [163] V. Shukla, J. Wörnå, N. K. Jena, A. Grigoriev, and R. Ahuja, *The Journal of Physical Chemistry C* **121**, 26869 (2017).
- [164] L. Kou, T. Frauenheim, and C. Chen, *The Journal of Physical Chemistry Letters* **5**, 2675 (2014).
- [165] S. Cui, H. Pu, S. A. Wells, Z. Wen, S. Mao, J. Chang, M. C. Hersam, and J. Chen, *Nature Communications* **6**, 8632 (2015).
- [166] A. N. Abbas, B. Liu, L. Chen, Y. Ma, S. Cong, N. Aroonyadet, M. Köpf, T. Nilges, and C. Zhou, *ACS Nano* **9**, 5618 (2015).
- [167] G. Lee, S. Kim, S. Jung, S. Jang, and J. Kim, *Sensors and Actuators B: Chemical* **250**, 569 (2017).
- [168] J. N. Reimers and J. R. Dahn, *Phys. Rev. B* **47**, 2995 (1993).
- [169] J. N. Reimers, *Journal of Power Sources* **54**, 16 (1995).
- [170] M. K. Aydinol, A. F. Kohan, G. Ceder, K. Cho, and J. Joannopoulos, *Phys. Rev. B* **56**, 1354 (1997).
- [171] M. Aydinol, A. Kohan, and G. Ceder, *Journal of Power Sources* **68**, 664 (1997).
- [172] M. K. Aydinol and G. Ceder, *Journal of The Electrochemical Society* **144**, 3832 (1997).
- [173] Y. S. Meng and M. E. Arroyo-de Dompablo, *Energy Environ. Sci.* **2**, 589 (2009).
- [174] D. J. Wales and J. P. K. Doye, *The Journal of Physical Chemistry A* **101**, 5111 (1997).
- [175] G. Henkelman, G. Jóhannesson, and H. Jónsson, “Methods for finding saddle points and minimum energy paths,” in *Theoretical Methods in Condensed Phase Chemistry*, edited by S. D. Schwartz (Springer Netherlands, Dordrecht, 2002) pp. 269–302.
- [176] G. Henkelman, B. P. Uberuaga, and H. Jónsson, *The Journal of Chemical Physics* **113**, 9901 (2000).
- [177] V. Shukla, R. B. Araujo, N. K. Jena, and R. Ahuja, *Nano Energy* **41**, 251 (2017).
- [178] Y. Jiao, F. Ma, J. Bell, A. Bilic, and A. Du, *Angewandte Chemie* **128**, 10448 (2016).
- [179] H. Nishino, T. Fujita, N. T. Cuong, S. Tominaka, M. Miyauchi, S. Iimura, A. Hirata, N. Umezawa, S. Okada, E. Nishibori, A. Fujino, T. Fujimori, S.-i.

- Ito, J. Nakamura, H. Hosono, and T. Kondo, *Journal of the American Chemical Society* **139**, 13761 (2017).
- [180] R. Peköz, M. Konuk, M. E. Kilic, and E. Durgun, *ACS Omega* **3**, 1815 (2018).
- [181] L. Kou, Y. Ma, C. Tang, Z. Sun, A. Du, and C. Chen, *Nano Letters* **16**, 7910 (2016).
- [182] B. Mortazavi, M. Makaremi, M. Shahrokhi, M. Raeisi, C. V. Singh, T. Rabczuk, and L. F. C. Pereira, *Nanoscale* **10**, 3759 (2018).
- [183] N. K. Jena, R. B. Araujo, V. Shukla, and R. Ahuja, *ACS Applied Materials & Interfaces* **9**, 16148 (2017).
- [184] M. Mortazavi, C. Wang, J. Deng, V. B. Shenoy, and N. V. Medhekar, *Journal of Power Sources* **268**, 279 (2014).
- [185] Q. Tang, Z. Zhou, and P. Shen, *Journal of the American Chemical Society* **134**, 16909 (2012).
- [186] V. Shukla, R. B. Araujo, N. K. Jena, and R. Ahuja, *Phys. Chem. Chem. Phys.* **20**, 22008 (2018).
- [187] M. Naguib, J. Come, B. Dyatkin, V. Presser, P.-L. Taberna, P. Simon, M. W. Barsoum, and Y. Gogotsi, *Electrochemistry Communications* **16**, 61 (2012).

Acta Universitatis Upsaliensis

*Digital Comprehensive Summaries of Uppsala Dissertations
from the Faculty of Science and Technology 1761*

Editor: The Dean of the Faculty of Science and Technology

A doctoral dissertation from the Faculty of Science and Technology, Uppsala University, is usually a summary of a number of papers. A few copies of the complete dissertation are kept at major Swedish research libraries, while the summary alone is distributed internationally through the series Digital Comprehensive Summaries of Uppsala Dissertations from the Faculty of Science and Technology. (Prior to January, 2005, the series was published under the title "Comprehensive Summaries of Uppsala Dissertations from the Faculty of Science and Technology".)



ACTA
UNIVERSITATIS
UPSALIENSIS
UPPSALA
2019

Distribution: publications.uu.se
urn:nbn:se:uu:diva-369471